Courants de spin et l'effet Hall de spin dans des nanostructures latérales

Piotr Laczkowski

UNIVERSITÉ DE GRENOBLE

THÈSE

Pour obtenir le grade de

DOCTEUR DE L'UNIVERSITÉ DE GRENOBLE

Spécialité : **Physique**

Arrêté ministérial :

Présentée par

Piotr Laczkowski

Thèse dirigée par **Dr. Alain Marty**
et codirigée par **Dr. Laurent Vila**

préparée au sein **du Laboratoire Nanostructure et Magnétisme**
et de **l'école doctorale de Physique**

Spin currents and spin Hall effect in lateral nano-structures

Thèse soutenue publiquement le ,
devant le jury composé de :

Prof. Alain Schuhl
Institut Néel, CNRS Grenoble, Président
Prof. Albert Fert
Unité Mixte de Physique CNRS/Thales (UMR137), Examinateur
Prof. Francois Montaigne
Laboratoire de Physique des Matériaux, Institut Jean Lamour, Nancy, Rapporteur
Dr. Michel Viret
Service de Physique de l'Etat Condensé, CEA Orme des Merisiers, Rapporteur
Dr. Alain Marty
INAC/SP2M/NM, CEA Grenoble, Directeur de thèse
Dr. Laurent Vila
INAC/SP2M/NM, CEA Grenobl, Co-Directeur de thèse

"Learn from yesterday, live for today,

hope for tomorrow. The important thing is

to not stop questioning."

Albert Einstein

Acknowledgements

I would like to express my gratitude to all the wonderful people that I had pleasure to meet during this 3-year adventure ! Thank you very much for your help and guidance - I wish you all the best and hope one day our paths will cross again !!

Laurent: *It is your patience, knowledge and trust in me that resulted in this wonderful cooperation and in such an extraordinary adventure. I wanted to thank you for being there for me as my supervisor but mostly as a friend in every aspect of day-to-day life and of course for all the precious knowledge ! You are the best supervisor that one can imagine !*

Jean-Philippe: *Thank you for sharing with me your wonderful academic and scientific point of view based upon simplicity, uniformity (not only colors, types etc..) and clarity ! For keeping an eye on me whenever I was meant to turn in a wrong direction (especially during the ski season ;) and for all the exciting out-off adventures (I will never forget about it) !*

Alain: *Thank you for your guidance and knowledge, for sharing with me whatever is the best in science ! Thanks for early morning discussions and for sharing my passion for programming and the open source software !! I will always admire your knowledge ("you are the man") !*

Cyril and Lucien: *Without you this work would be simply impossible, so let me thank you for all your hard work, perfect organization and precision always coming along with a very good atmosphere, humor and music (keep on rocking) !!!*

Dai: *Thank you for this wonderful time spent together as office-mates and after-all as friends during this PhD journey ! I wish you the very best in every aspect and hope that one day we could work together once again!*

Irina: *Thanks for your help and guidance, for your soft heart and good example ;) . I will always remember the football tournaments, captain !*

Carlos, Williams and Murat: *Thanks for completing this great team, for motivation, humor and all of many adventures ! Have to say it was a great experience to work with you !*

Thilbaut, Jean-Luc, Helge, Christophe, Sebastien, Gile, Tristan, Milène, Perrine and all of the clean room staff members in PTA and CIME: *Thank you very much for making me one of you as a clean room/white-ninja family member - It was a great experience / wonderful memories !!!*

Mathieu, Ariel, Céline, Robert, Patrick, Stéphan, Louis et al. : *Thanks for your humor, optimism, patience and knowledge that always built a very nice and friendly atmosphere in the lab - I will miss it !!!*

Albert, Alain, Henri, Jean-Marie, Cyril: *Thank you for your guidance, patience and for the trust in me - It was a distinct pleasure to work with you during the Spin-Hall project !*

and al. *not mentioned above.*

Using these simple words I would like to acknowledge all you have done for me:
THANK YOU !!!

Table of Contents

Introduction

In conventional electronics, information is stored, manipulated and transported by electron charges. Further progress can no longer be accomplished by merely scaling transistors to smaller geometries, mainly because of the dramatic increase in power consumption in highly scaled Complementary Metal Oxide Semiconductor (CMOS) devices. Advances in new magnetic materials and devices, based on the electronic spin, build an attractive alternative to maintain the progress in computation and data storage [1].

As it becomes clear that breakthroughs are needed, nano-magnetic systems could provide unique opportunities. Indeed, the dissipation energy of magnetic processes can be orders of magnitude smaller than those of CMOS. Furthermore, most magnetic applications are inherently non-volatile and radiation hard, and could lead to increased data processing speeds [2]. Spin-based memories and logic devices could complement or supplant traditional semiconductor microelectronics, especially since spintronics nowadays involves not only metals [3] but semiconductors [4] or even graphene-based structures [5].

In 1988 Albert Fert and Peter Grünberg discovered independently the Giant Magneto-Resistance effect (GMR) [6, 7]. A GMR device consists basically of a trilayer vertical structure, with two ferro-magnetic layers separated by a thin non-magnetic metallic material [8]. The first observation of GMR in a spin-valve [9], in which the magnetization of the free layer can be reversed by small magnetic fields, and the discovery of Tunnel Magnet-Resistance (TMR) [10, 11, 12], led to the miniaturization of the hard drives recording heads, and thus to a strong increase of the storage density [1].

As GMR implies spin injection from a ferromagnetic into a non-magnetic metal, its discovery, showed the importance of spin accumulation and of spin-polarized currents [13, 14]. The development of the TMR, with ratios up to almost 605% at room temperatures [15] and 1144% at $5\,K$ [16], provided the basis for application of this effect in random magnetic access memory devices (MRAM). Also, intensive theoretical studies on the spin injection from a magnetic metal into a non-magnetic semiconductor, brought to light the conductivity mismatch problem, resolved by the introduction of a thin isolating layer in between the two materials [17].

Both GMR and TMR effects thus allow an efficient detection of the magnetically encoded informations. The next important stage, for spintronics, was the ability not only to read information, but to write it using spin currents. The concept of spin angular momentum transfer, associated to the flow of a spin-polarized current into a ferromagnet, has been introduced in 1996.

Slonczewski predicted theoretically the effect [18], now currently observed in nanopillars, whereas Berger suggested to use the spin transfer to induce domain wall motion [19]. These effects are already implemented in Spin-Transfer Torque Random Access Memories (STT-RAM) [20], in pillars, which possess low power consumption, and high thermal stability. Alternatively, logic or memory applications based on current-induced domain wall motion, as the racetrack memory [21], are currently under study [22]. The spin-torque also opened a way to create oscillations of the magnetization in the microwave frequency range, which could lead to the development of new tunable micro-wave emitters [23].

Conventionally the ferro-magnetic/non-magnetic interface is used for the spin current generation, however new possible sources were developed recently, taking profits of the spin Hall effect (spin-orbit interaction) [24], the Seebeck-Peltier effect (temperature gradient) [25] and the spin pumping (ferro-magnetic resonance) [26].

In this context, the Spin Hall Effect (SHE) recently gained the interest of theoreticians and experimentalists, since it provides an alternative spin current source or spin current detector, that does not require magnetic materials nor magnetic fields [27, 28]. The spin accumulation is generated by the charge current passing through the material *via* the spin-orbit interactions [24]. In this case, the longitudinal charge current is transformed into a transverse spin current. The SHE is quantified by the ratio of the conversion of charge to spin current, called the spin Hall angle (SHA). One could imagine many possible applications of the SHE, if the ratio of conversion could be comparable to what can be obtained by magnetic materials in spin-valves or tunnel junctions.

Among the variety of possible applications of this effect, some have been already explored during the time of this thesis. The spin-torque switching of ferro-magnets, using SHE induced spin currents was recently demonstrated experimentally for tantalum [29], event at room temperature. Moreover, experiment on the spin-torque ferromagnetic resonance, induced by the SHE, was also reported [30]. There were also propositions of the spin Hall effect transistors, allowing detection directly along the gated semiconductor channel [31].

In the SHE, the same spin accumulation is generated everywhere at the surface of the material. One can thus imagine a spin current generation line, with multi terminals connection to it. At each terminal the same amount of the spin current would be generated, independently on the terminals number. This could be used, for example, in a massive depinning of the domains walls by exerted spin-torque. Nevertheless, as the SHE deals with spin current and do not induce voltage drop in a material, new experimental techniques and schemes are required.

The SHE-induced spin accumulation in semiconductors has drawn much attention because of its compatibility with the conventional CMOS technology. Up to now, semiconductors such as GaAs, ZnSe have exhibited a very small SHE and no electrical detection has been reported. In contrast, metals, such as Pt or Ta, have been successfully used to detect the SHE, even at room temperature, exhibiting the largest spin Hall angle ($> 10^{-2}$), reported so far for pure materials [32, 33]. Large spin Hall angles, reaching 0.025 (2.5% of conversion), were found many years ago for materials doped with non-magnetic impurities, what was demonstrated by Fert *et al.* [34] for

Cu doped with Ir, Ta and Lu. Also, very recent experiments showed large SHA, of the order of 2% for Cu doped with Ir impurities [35]. The quantitative estimation of the spin Hall angle is actually under intensive debate, and the experimental procedure has still to be carefully defined. At the beginning of this thesis, the highest spin Hall angle was reported for Pt, with a value smaller than 10^{-2}.

Electrical detection has been shown for metals, even with reversible conversion of spin to charge current, reflecting the inverse and direct spin Hall effects. These measurements were made using either tunneling [36] or ohmic contacts [32, 33, 37] in lateral spin-valve (LSV) devices or spin-pumping technique [38, 39, 40, 41]. The spin pumping and the LSVs with ohmic contacts, where the SHE material was integrated, are the two complementary techniques, allowing good characterization of new SHE materials.

The spin pumping can now give access to the quantitative determination of the SHE [26, 42]. The ferromagnetic resonance is used to induce oscillations of the magnetization in the ferromagnet, deposited on the non-magnetic layer. These oscillations pump spins into the non-magnetic material, thus creating a vertical spin current detectable *via* the inverse SHE [43]. The spin diffusion length, necessary for SHA estimation, can be only evaluated by studying of the thickness variation of the SHE material. However, that requires several samples preparation, and becomes difficult for materials with short spin diffusion length, as it would require fabrication of the ultra-thin layers [44]. Complementary techniques are thus required.

The electrical SHE experiments are based on lateral spin-valves, which consist of two ferromagnetic electrodes linked by the non-magnetic channel. In these devices, the material with strong spin-orbit interaction is inserted between the two ferro-magnetic electrodes. Most of the work done on spin transport has focused on the vertical [8], with much less effort concentrated on the lateral spin-valve structure. The development of this aspect is equivalently important, since many future spintronics components will require lateral integration [45]. Moreover, the LSVs allow for the spatial separation of the charge and spin currents [46, 47], thus providing a powerful tool for detecting spin-related phenomena without the Anisotropic Magneto-Resistance (AMR) nor the Hall effect contributions to the output signal [48]. The additional advantage of the lateral structures comes from the possibility of applications in multi-terminal geometries, like a spin-flip transistor [49]. That is much more complicated in the case of the vertical devices.

The electrical spin injection in metallic LSVs was first demonstrated, in the non-local geometry, by Johnson and Silsbee [47] for permalloy ferro-electrodes deposited on top of a bulk aluminum. The real interest however, flourished after the work of Jedema *et al.* [50] on the nano-scale LSVs, patterned by electron beam lithography, resulting in the investigation of many different materials, using different geometries [51, 52, 53, 54, 36]. However, one has to resolve technical issues such as efficient injection, transport, control, and detection of spin polarization as well as spin-polarized currents.

In the frame of this PhD thesis, **the main challenge consists of the development of efficient characterization means of the SHE and its application to the characterization of dilute alloys.** New materials are forecasted to target enhanced spin-orbit interaction,

as demonstrated recently by *ab-initio* and analytical calculations [55, 56]. For this purpose, the lateral spin-valve devices will be first optimized, in order to achieve highly efficient injection and reliable non-local detection of the spin currents. They will be further adapted for the study of the SHE, using electrical generation of spin currents in the hybrid geometry.

Outline

This PhD manuscript is divided into six chapters, organized in the following order:

Chapter 1 Description of the basic transport theory in lateral spin vales, necessary for understanding the work presented in the manuscript. The GMR and Non-Local injection and detection concepts are introduced and explained in the framework of the electro-chemical potential distribution.

Chapter 2 Optimization of the spin signal in LSV, aiming at highly efficient spin injection and reliable spin detection, is presented. The description is based upon the 1D spin transport model and underlines the importance of the interface, geometry and nano-fabrication methods. All these aspects are discussed in details, and the optimization procedures are presented.

Chapter 3 Description of the basic methods and their application for spin dependent transport characterization in the lateral nano-structures is presented. Material parameters are extracted using 1D standard model and the Finite Element Method (FEM) approach. Also an alternative analysis based on the transfer matrix approach is made. The evaluation of the parameters is also combined with FEM simulations providing a powerful tool for these analyses.

Chapter 4 Further optimization of the LSV by confining laterally the spin accumulation into the useful, active part of the nano-structure is demonstrated. Analysis based on the transfer matrix theory, allowing complete description of the spin signal amplification in the Py/Au nano-devices is presented, underlining the role of the spin current polarization and the spin current accumulation. The discussion of the amplification regimes for various geometries is given with the numerical calculations and FEM simulations.

Chapter 5 Vertical confinement of the spin accumulation by introduction of the tunnel barriers between the ferro-magnetic and the non-magnetic material is demonstrated. This is done by inserting a natural oxide alumina barrier at the interface of the LSV. Spin precession is studied and characterized by the Hanle effect while applying the external magnetic field in and out of the samples plane.

Chapter 6 Description of the spin Hall effect is provided introducing basic ideas of the experimental detection methods. Methodology of the spin Hall angle evaluation is presented together with qualitative analyses for Pt and AuW based nano-devices, with both spin pumping and transport measurements.

Chapter 1

Theory of spin transport in lateral spin-valves

The goal of this chapter is to introduce the basic physical concepts describing spin polarized transport in lateral nano-structures. First, parameters describing the general electronic transport in metals will be introduced, taking into account the spin degree of freedom. Also, a brief overview of the main spin-flip mechanisms in the non-magnetic metal will be presented. The spin diffusion model will be introduced and applied to the case of a single ferromagnetic/non-magnetic interface. This will be further extended to the case of a ferromagnetic/non-magnetic/ferromagnetic heterostructure with the concept of a ferromagnetic voltage probe. Finally, local (GMR) and non-local measurements will be presented and described in the lateral spin-valve with an emphasis on the description of the electro-chemical landscape and the concept of pure spin currents.

1.1 Basics of spin transport in metals

In order to describe the spin transport, two important length-scales need to be taken into account. First of them is called the **electron mean free path** and is noted l_e. In lateral spin-valves, one uses a diffusive transport regime which is applicable when l_e is shorter than the device dimensions (case of all nano-devices presented in this thesis). The second important length-scale is represented by **the spin diffusion length (l_{sf}^N),** which defines the material characteristic length over which the memory of the spin will be lost, its orientation randomized. In the following, the role of these quantities will be pointed out in the description of diffusive transport. In this picture the fully occupied states well below the Fermi surface are neglected.

For systems with two spin species, it is convenient to use a thermodynamic quantity called **the electro-chemical potential** (related to the chemical potential μ_{chem} through $\mu = \mu_{ch} - eV$, where e is the absolute value of the electron charge and V is the electric potential). One can assign a separate electro-chemical potential associated to each spin specie, defined as the energy that has to be put into the system to increase by one the number of particles (containing the additional potential energy eV).

In metals, the $l_{sf}^{F(N)}$ is usually much larger than the mean free path $l_{sf}^{F(N)} \gg l_e^{F(N)}$, thus the

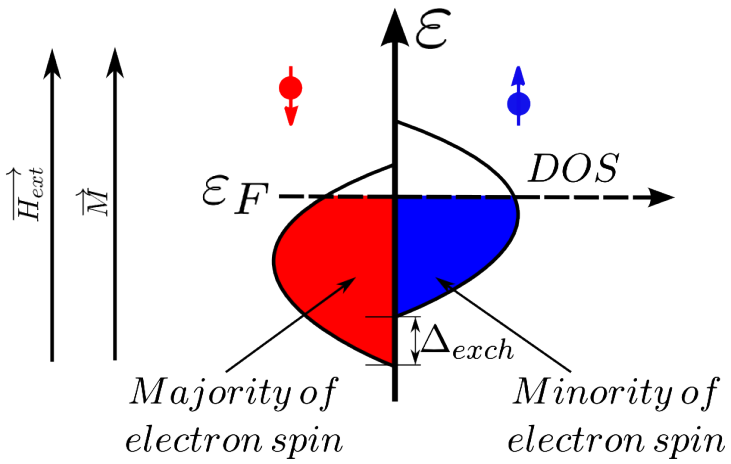

Figure 1.1: *The Stoner model of ferromagnetic transition metals, illustrated for the 3d shell. The spin states with the largest number of electrons are called majority spins, whereas those with the lower number are the minority spins. The Fermi energy level ε_F which separates the occupied from unoccupied electron states is indicated by the dashed line. The centers of the majority and minority sub-bands are separated by the exchange splitting Δ_{exch}. The quantization direction is determined by the $\vec{M}$ direction and can be controlled by the external field H_{ext}. [61]*

two spin species can be treated separately. In a first approximation, spin-dependent transport can be described by two separated independent spin channels, following the model proposed by Mott [57]. This idea was followed by Fert and Campbell to describe the transport properties of Ni, Fe and Co based alloys [58] and further extended by Van Son *et al.* [59] to describe transport through transparent ferromagnetic/non-magnetic interfaces. The use of ferromagnets to inject and detect spins led to the discovery of the Giant Magneto-Resistance effect by the groups of Fert [6] and Grünberg [7]. That quickly led to the miniaturization of the recording heads of hard-disk drives, and earned Fert and Grünberg the 2007 Nobel Prize in Physics [8, 60]. Valet and Fert [13] have developed Boltzmann equations based on the diffusion model including spin-flip scattering to analyze current perpendicular to the plane (CPP) GMR effect in magnetic multi-layers. This approach provides a full description of the spin transport in a lateral spin-valves.

1.1.1 Transport in a ferromagnetic metal

In a ferromagnetic material (F) electrons strongly interact with each other *via* the **exchange interaction**. Even in the absence of a magnetic field this interaction creates a magnetic order responsible for a non-zero average magnetic momentum. In this manner, a collective degree of order of electrons spin creates a macroscopic magnetic moment e.g., magnetization.

The Stoner model, represented schematically in figure 1.1, assumes that the density of states (DOS) for the majority and minority electrons is often nearly identical, but the states are shifted in energy with respect to each other by the exchange energy Δ_{exch}. The quantization axis is given by the direction of the magnetization $\vec{M}$. Since the magnetization represents an average magnetic moment of a volume, and the magnetic moment of each electron is defined as $m = -g\mu_B s$ (where g is the normalized dimensionless magnetic moment, μ_B is the Bohr magneton, and s is the

electron spin), the moment and the spin have opposite directions. Therefore, in the presented case, the majority states are spin-down and the minority states are spin-up [61]. The electrons responsible for electric transport in the transition metals (Ni, Fe, Co) are situated at the Fermi energy. The current is carried mainly by the s band electrons, whereas the $s-d$ diffusion probability is responsible for the conductivity value. It mainly depends on the DOS at the d sub-bands since the probability of diffusion depends on available states at ε_F. Due to the energy splitting the DOS at the Fermi level is different for the two spin directions. This means that the total conductivity σ is determined by the conductivities of both spin-up electrons, $\sigma_\uparrow$, and spin-down electrons, $\sigma_\downarrow$, being different. Note that in representation with respects to the spin-transport, the majority and minority spin population are spin-up and spin-down respectively (contrary to the magnetic moment representation).

Treating independently each spin population, one can define the conductivities $\sigma_\uparrow$ and $\sigma_\downarrow$, in a general case as follows:

$$\sigma_\uparrow^F = \alpha_F \sigma^F;\ \sigma_\downarrow^F = (1-\alpha_F)\sigma^F \tag{1.1}$$

where α_F stands for the asymmetry of conduction in F ($0 \leq \alpha_F \leq 1$), and $\sigma^F = \sigma_\uparrow + \sigma_\downarrow$.

In the bulk ferromagnet it is usually $\alpha_F^{bulk} > 0.5$ (while considering the minority channel as one having lower conductivity and considering spin up as the majority), where the case of $\alpha_F = 0.5$ describes a non-magnetic metal.

We can use **the two currents model** to define the total current density, flowing in the ferromagnet, as the sum of the up and down currents: $j = j_\uparrow + j_\downarrow$; where $j_\uparrow$ is related to the spin "up" and $j_\downarrow$ to the spin "down" population. They are defined as

$$j_\uparrow = -\frac{\sigma_\uparrow}{e}\frac{\partial \mu_\uparrow}{\partial x};\ j_\downarrow = -\frac{\sigma_\downarrow}{e}\frac{\partial \mu_\downarrow}{\partial x} \tag{1.2}$$

In this representation, **the spin polarization P of the current** can be defined as:

$$P = \frac{\sigma_\uparrow - \sigma_\downarrow}{\sigma_\uparrow + \sigma_\downarrow} = \frac{j_\uparrow - j_\downarrow}{j_\uparrow + j_\downarrow} \tag{1.3}$$

The value of the spin polarization of the current for permalloy is usually found to be close to $P = 0.77$ [50, 62].

1.1.2 Electron spin transport in a metal

In the non-magnetic material conductivities for both spin populations are equal. In order to describe the spin-dependent transport in a non-magnetic metal, the Ohm's law can be rewritten using current densities related to two spin populations, Eq. 1.2.

The charge and spin continuity equations impose that:

$$\begin{aligned} \tfrac{\partial}{\partial x}(j_\uparrow + j_\downarrow) &= 0 \\ \tfrac{\partial}{\partial x}(j_\uparrow - j_\downarrow) &= -e(\tfrac{n_\uparrow}{\tau_{\uparrow\downarrow}} - \tfrac{n_\downarrow}{\tau_{\downarrow\uparrow}}) \end{aligned} \tag{1.4}$$

Then the spin-flip mechanism is introduced. The latter, is represented by the spin-flip time

which can be defined as the average time to flip a spin-up to a spin-down: $\tau_{\uparrow\downarrow}$, and to flip a spin-down to a spin-up: $\tau_{\downarrow\uparrow}$. Note that in some ferromagnets, like NiFe, the spin-flip time and the elastic scattering time (related with l_e) can become comparable [62].

The total number of particles in the system has to be conserved, which imposes:

$$\frac{1}{e}\frac{\partial}{\partial x}j_{\uparrow} = \frac{n_{\downarrow}}{\tau_{\downarrow\uparrow}} - \frac{n_{\uparrow}}{\tau_{\uparrow\downarrow}};\ \frac{1}{e}\frac{\partial}{\partial x}j_{\downarrow} = \frac{n_{\uparrow}}{\tau_{\uparrow\downarrow}} - \frac{n_{\downarrow}}{\tau_{\downarrow\uparrow}} \tag{1.5}$$

where $n_{\uparrow}$ and $n_{\downarrow}$ are the excess particle densities for each spin population.

By using Eq. 1.2 for current densities, representing opposite spin populations, together with Eqs. 1.4 and stating that the scattering rates for spin-up and spin-down are equivalent at equilibrium (so-called detailed balance principle: $N_{\uparrow}/\tau_{\uparrow\downarrow} = N_{\downarrow}/\tau_{\downarrow\uparrow}$, where $N_{\uparrow(\downarrow)}$ is the densities of states at the Fermi level for spin-up (spin-down) species), one can obtain the diffusion equation. Note that for small variations from equilibrium ($\Delta\mu \ll E_F$), supposing that the potential energy is zero, the electro-chemical potential is related to the excess particle density $n_{\uparrow(\downarrow)}$ *via* the density of states at the Fermi energy $\mu = n_{\uparrow(\downarrow)}/N_{\uparrow(\downarrow)}$.

One can thus obtain:

$$D\frac{\partial^2(\mu_{\uparrow} - \mu_{\downarrow})}{\partial x^2} = \frac{(\mu_{\uparrow} - \mu_{\downarrow})}{\tau_{sf}} \tag{1.6}$$

where: $D = D_{\uparrow}D_{\downarrow}(N_{\uparrow} + N_{\downarrow})/(N_{\uparrow}D_{\uparrow} + N_{\downarrow}D_{\downarrow})$ is the spin average diffusion constant (linked with conductivity by so-called Einstein relation: $D = \sigma/e^2N$). The diffusion constants for each spin direction depend on the Fermi velocities and mean free paths: $D_{\uparrow(\downarrow)} = 1/(3v_{F\uparrow(\downarrow)}l_{e\uparrow(\downarrow)})$, where $v_{F\uparrow(\downarrow)}$ represents the spin dependent Fermi velocities, $l_{e\uparrow(\downarrow)}$ stands for the electron mean free paths and the factor $1/3$ deals with the dimensionality of the system. The spin-flip time τ_{sf} is defined as: $1/\tau_{sf} = 1/\tau_{\uparrow\downarrow} + 1/\tau_{\downarrow\uparrow}$. This time represents the timescale over which the non-equilibrium spin accumulation decays. One introduces the so-called **spin diffusion (relaxation) length** which is linked with the spin-flip time by $l_{sf}^N = \sqrt{D\tau_{sf}}$. The above-mentioned parameter will be used in this thesis in order to characterize the spin transport in the lateral nano-structures. Thus the diffusion equation can be written in the following form:

$$\frac{\partial^2}{\partial x^2}(\mu_{\uparrow} - \mu_{\downarrow}) = \frac{(\mu_{\uparrow} - \mu_{\downarrow})}{l_{sf}^2} \tag{1.7}$$

The general form of the steady state solution of the spin diffusion equation [cf. Eq. 1.7] in an homogeneous medium with a constant section (of the ferromagnet or the normal metal) is given by [14]:

$$\begin{aligned} \mu_{\uparrow} &= A + Bx + \frac{C}{\sigma_{\uparrow}}exp(-x/l_{sf}^N) + \frac{D}{\sigma_{\uparrow}}exp(x/l_{sf}^N) \\ \mu_{\downarrow} &= A + Bx - \frac{C}{\sigma_{\downarrow}}exp(-x/l_{sf}^N) - \frac{D}{\sigma_{\downarrow}}exp(x/l_{sf}^N) \end{aligned} \tag{1.8}$$

The coefficients A, B, C, D can be determined using boundary conditions imposed at the junctions, where the wires are coupled to other materials or vacuum [50, 62].

In the case where the interface spin-flip process and the interface resistance (transparent

interface approximation) are neglected, boundary conditions at the interface are:

(1) continuity of the electro-chemical potentials $\mu_\downarrow, \mu_\uparrow$.

(2) conservation of the spin currents $j_\downarrow, j_\uparrow$.

Otherwise, when the interface resistance and the spin-flip processes are taken into account, the interface is treated as an infinitely thin layer. One then attributes the following parameters to describe this layer: the interface spin resistance R_b^*, the spin asymmetry parameter at the interface γ and the spin-flip parameter δ. This approach will be discussed in details in *Chapter 3* where the transfer matrix method will be introduced, taking into consideration bulk and interface effects.

In the presented approach of the diffusive spin transport the densities of each spin population are controlled by the spin-flip process. It is therefore interesting to look at the mechanisms responsible for the spin relaxation.

1.1.2.1 The spin-flip mechanism

The spin relaxation in metals can be described for most metals by **the spin-orbit interaction,** governed by Elliot-Yaffet, Dyakonov mechanisms [63, 64, 24, 65]. This relaxation process can be quantified using the spin-flip time τ_{sf}. Typical values of τ_{sf} are in the range of pico-seconds (typical for metals) to nano-seconds (typical for semiconductors) with the longest spin-flip time in the order of a milli-second, reported for high-purity sodium [66].

Three important mechanisms can be pointed out for the spin relaxation process in metals. At low temperatures ***the impurity spin-flip scattering*** dominates, which is indicated by the constant behavior of $1/\tau_{sf}$, whereas at high temperatures $1/\tau_{sf}$ grows linearly with increasing temperature, indicating ***the phonon induced spin relaxation***. An important scattering mechanism can be also attributed to the **relaxation due *to surface scattering*** in the experiments with thin-film metals [50, 54, 62].

1.2 Ferromagnetic/Non-magnetic interface

When putting in contact a ferro-magnetic (F) and a non-magnetic material (N) the Fermi-levels of both metals will align provided a current is not applied. In this case, the electro-chemical potential μ will be constant across the F/N interface.

When a current (j) flows from F into N, without taking into account spins, the average electro-chemical potential μ profile, over a given distance (cf. *Figure 1.2*), is represented by a straight line with a change in the slope on both side of the F/N interface, which is due to the change in the conductivities σ, that are not equal in each material ($\sigma^F \neq \sigma^N$). This image becomes more complicated when considering the existence of two spin species in F, as for each one the conductivity is different.

Let us consider a simple ferromagnetic/non-magnetic interface, represented in Fig. 1.2 (a), with current of density j flowing through it. Conductivities for spin-up and spin-down channels

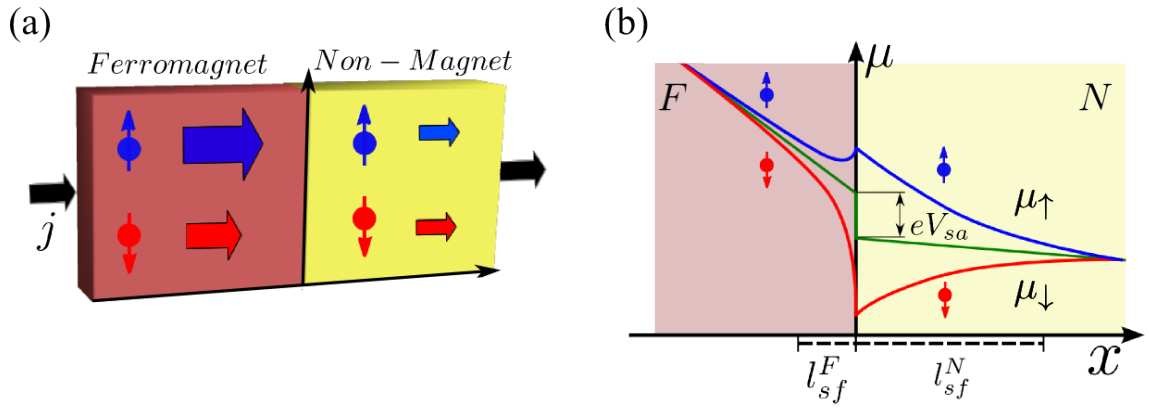

Figure 1.2: *(a) Sketch represents a ferromagnetic/non-magnetic interface with a charge current of density j flowing through it. Red and blue arrows represent respectively spin-down and spin-up populations while their sizes reflect differences in conductivities. (b) The electro-chemical potentials are represented by blue and red curves for the majority and minority spin populations respectively. Green lines stand for the spin averaged electro-chemical potentials. The spin accumulation voltage, at the vicinity of the interface, is given by the difference of the spin averaged electro-chemical potential in the ferromagnet and non-magnet, $eV_{sa} = \mu_F - \mu_N$. Here, $l_{sf}^{F(N)}$ stands for the spin diffusion length in the ferromagnetic and non-magnetic material.*

are represented by the blue and red arrows respectively. The difference in size reflects the difference in conductivities for both spin populations. When the spin-polarized current from F enters N, it will take time or distance from the interface for the current in N to reach the non-polarized value (equilibrium state of the spin-up and spin-down currents). This means that at the vicinity of the interface in N, the spin current polarization will be different from zero: $P \neq 0$. The discontinuity of the average electro-chemical potential at the interface will occur, and therefore, a voltage V_{sa}, called **the spin accumulation voltage,** will develop. In other words, since the DOS at Fermi energy in F is larger for spin-up than for spin-down electrons, most of the electrons injected into N will be the spin-up electrons. In order to preserve the charge neutrality in each material, an increase in the number of electrons with spin-up must be accompanied by a decrease in the number of spin-down electrons. Therefore, charge transport across the F/N interface is accompanied by the spin transport [54].

So as to calculate the spin accumulation voltage at the F/N interface, one can rewrite the Ohm's law [cf. *Eq. 1.2*] in the following form (combining with notation from *Eq.1.1*) :

$$\frac{\partial \mu}{\partial x} = -\frac{e}{\sigma} j = -\frac{e}{\sigma}(j_\uparrow + j_\downarrow) = \alpha \frac{\partial \mu_\uparrow}{\partial x} + (1-\alpha)\frac{\partial \mu_\downarrow}{\partial x} \tag{1.9}$$

After integration of the above equation, the average electro-chemical potentials in F and N can be expressed as follows:

$$\begin{aligned} \mu^F &= \alpha_F \mu_\uparrow + (1-\alpha_F)\mu_\downarrow \\ \mu^N &= \tfrac{1}{2}(\mu_\uparrow + \mu_\downarrow) \end{aligned} \tag{1.10}$$

Figure 1.2(b) represents the electro-chemical potential landscape at the vicinity of the F/N

interface. The slope of the average electro-chemical potential corresponds to the electric field related to the flow of the electrical current. The electro-chemical potentials $\mu_\uparrow$ and $\mu_\downarrow$, represented by blue and red color respectively, are continuous for a transparent interface. While the electro-chemical potential μ (represented by the green line) is **the average of $\mu_\uparrow$ and $\mu_\downarrow$ in N, it is a weight average in F**. Due to this, a drop of electro-chemical potential occurs at the interface: $\Delta\mu = eV_{sa}$, which reflects the difference in the number of electrons of the two spin channels.

As demonstrated by Van Son *et al.* [59], by using appropriate boundary conditions and the current flowing perpendicularly to the interface (represented by the current density j) one can define the boundary resistance related to the potential drop of a single F/N interface, as follows:

$$R_b = (\mu^F_{\uparrow(\downarrow)} - \mu^N_{\uparrow(\downarrow)})/ej = \frac{(2\alpha_F - 1)^2 l^N_{sf}\sigma_N^{-1}}{1 + 4\alpha_F(1-\alpha_F)\frac{l^N_{sf}\sigma_N^{-1}}{l^F_{sf}\sigma_F^{-1}}} \tag{1.11}$$

The spin accumulation in the N can thus act as a source of spin electromotive force which produces a voltage $V_{as} = jR_b$.

1.3 Spin current detection

In the following, the description of the GMR effect will be presented together with the electro-chemical potential landscape for local current injection. This will be then extended to the case of the non-local geometry allowing the pure spin current generation and the spin current detection.

1.3.1 GMR and the electro-chemical landscape

When adding a second $F2/N$ interface into the system with electrical spin injection, represented in Fig. 1.2(a), to form a $F1/N/F2$ multilayer, one can directly tune the resistance of the structure by changing the respective magnetic orientation of F1 and F2. This leads to the Giant Magneto-Resistance effect.

In the simple representation, when the spin-polarized electrons travel through the nano-structure, represented in Fig. 1.3(a), depending on their spin orientation and the magnetic state of the ferro-magnetic electrodes, the electrons will experience different resistances in the ferro-magnetic layers. If the direction of magnetization in F is the same as the direction of electrons spin, electrons will travel more easily (lower scattering) than in the opposite case. This means that in the parallel (P) magnetic configuration the total resistance related to electrons path will be lower than in the anti-parallel (AP) state. This can be understood using resistance-circuit representation for both magnetic states, presented in Fig. 1.3(b). Assuming there is no spin-flip in N, the total resistance can be written as the sum of the resistance for spin "up", $R_\uparrow$ and "down", $R_\downarrow$, for parallel and anti-parallel state, as follows:

$$R_P = \frac{R_\uparrow R_\downarrow}{R_\uparrow + R_\downarrow},\ R_{AP} = \frac{R_\uparrow + R_\downarrow}{2} \tag{1.12}$$

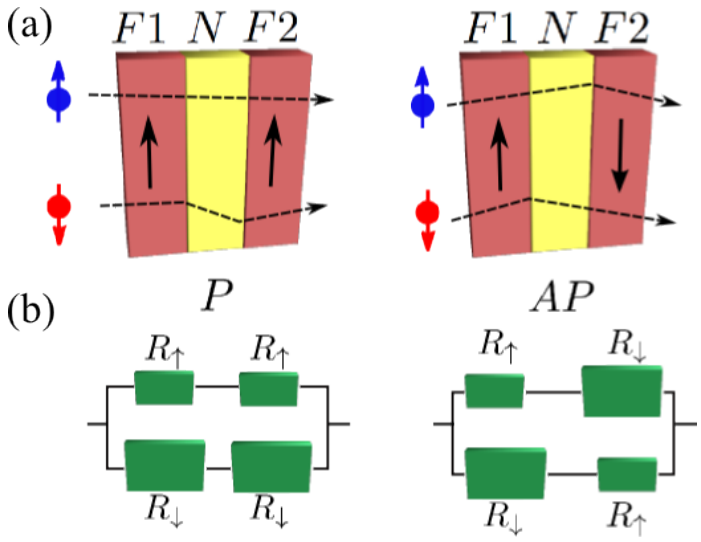

Figure 1.3: *(a) Schematic of basic GMR device showing the scattering processes at the interfaces for spin up and down populations. This depends on the relative magnetic configuration of the ferromagnets (P stands for parallel and AP for anti-parallel). (b) The resistors representation of the two channel model for GMR configuration with resistances $R_{\uparrow(\downarrow)}$ dependent on spins.*

An alternative description of this effect can be made using the electro-chemical potential distribution. Figure 1.4(a-b) shows the electro-chemical potential landscape for two identical ferromagnets ($F1$ and $F2$) connected with a non-magnetic material (N), where both ferromagnets are in (a) anti-parallel (AP) or (b) parallel (P) state of magnetization. When the charge current flows through $F1$, it spin polarizes, therefore, when entering N, a spin accumulation is created. This spin accumulation diffuses in N and can be detected at the second $N/F2$ interface. Blue and red curves in figure 1.4(a-b) correspond to opposite spin populations (up and down respectively), the average spin accumulation potential is represented by the green line (its slope reflects the electrical field driving the charge current). In the case of AP magnetic state of the ferromagnets, it will be more difficult for the majority spin population to enter into the second ferromagnet, what is represented by a higher electro-chemical potential at the second interface for this spin specie (blue). In the case of the minority spins, the situation is opposite, then it will be much easier to go into F2, what is represented by a lower electro-chemical potential at the second interface (red).

The distribution of electro-chemical potentials in the system will change with alignment of the magnetization of $F1$ and $F2$. In the parallel (P) alignment of the magnetization, represented in Fig. 1.4(b), the majority spins will not influence much resistance when traveling from $F1$ to $F2$, in contrast to the minority spin population. In this case, the spin accumulation voltage in the parallel state V_{sa}^{P}, created at both interfaces, will be smaller than the one of the AP state V_{sa}^{AP}. In other words, in the case of AP state, the spin-up electrons, coming from the injector, will have to spend more energy to become spin-down in the detector. This situation will be reflected by the higher resistance in the AP state.

The difference in the resistance of the $F1/N/F2$ heterostructure is reflecting the spin accu-

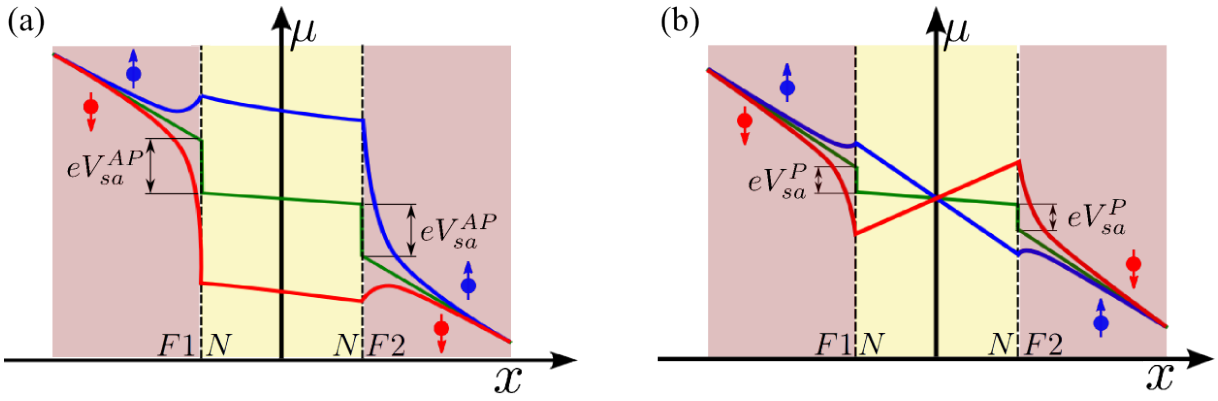

Figure 1.4: *Electro-chemical potential landscape of an heterostructure composed of two ferromagnets ($F1$ and $F2$) connected with a non-magnetic material (N) with current of density j flowing through the interfaces in the case of (a) anti-parallel and (b) parallel magnetization state. The blue curve corresponds to spin-up and the red curve to spin-down electro-chemical potentials. The spin average electro-chemical potential is represented by green lines. At each of the two interfaces, $F1/N$ and $N/F2$, the spin accumulation voltage V_{sa} develops. Note that spin-up refers always to majority spins in F1, while in $F2$ it corresponds to majority spins in P case and minority spins in AP case.*

mulation difference, as mentioned before [cf. *Eq.1.11*]. When measuring the resistance difference in anti-parallel and parallel magnetic alignments of F1 and F2, one can find the voltage difference of $2V_{sa}^{\hat{A}P} - 2V_{sa}^{P}$, which is the offset of voltage appearing in the AP state in GMR [13]. A more detailed description of this case will be presented in *Chapter* 4.

1.3.2 Pure spin current injection and detection

In the case of the lateral structures with multiple connections to the F/N interface, represented schematically in Fig. 1.5(a), it is possible to separate charge and spin currents. When the spin-polarized current, represented by the red arrow, flowing from the ferromagnetic material enters the non-magnetic material, a spin accumulation is created at the vicinity of the $F1/N$ interface. This spin accumulation diffuses in both directions from the interface, over the characteristic distance of the spin diffusion length l_{sf}^{N} in N and l_{sf}^{F} in F. While the spin current, resulting from the spin accumulation, diffuses in two directions from the interface in N, the charge current is drained out in one direction only (left side of the schematic). Thus, in the non-magnetic material, on the right side of the F/N interface of the nanostructure presented in Fig. 1.5(a), only the pure spin current flows without a net charge current [67]. In this region we can write the following relations:

$$\begin{aligned} j_{charge} &= j_{\downarrow} + j_{\uparrow} = 0 \\ j_{spin} &= j_{\downarrow} - j_{\uparrow} \neq 0 \end{aligned} \tag{1.13}$$

One can understand a **pure spin current** as the flow of spins of each specie in opposite directions, in the way that there is no net charge flow. This spin current injection process from a ferromagnet into the non-magnetic channel is represented in Fig. 1.5(b) using the electro-

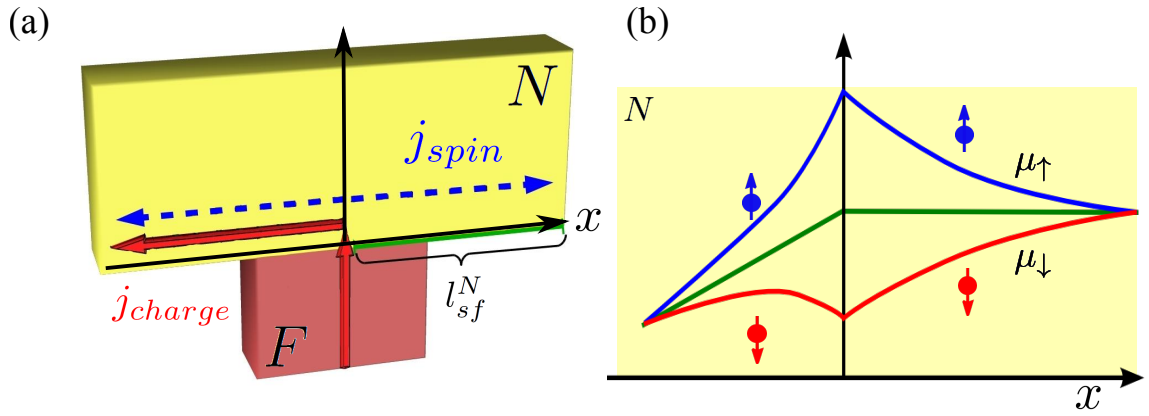

Figure 1.5: *Figure (a) represents a ferromagnetic/non-magnetic interface with three terminals (connections), thus allowing separation of charge and spin currents represented by the current densities (j_{charge} for charge and j_{spin} for spin). The spin accumulation created at the vicinity of the interface will diffuse in both directions whereas the charge current is drained out on the left side of $F1/N$ interface only, resulting in a pure spin current injection on the right side. (b) The electro-chemical potentials distribution for spin "up" (blue) and "down" (red) population in N. At the interface, where the electrical spin injection takes place, the spin accumulation is maximal (central point) decreasing exponentially over the characteristic distance of l_{sf}^N in N up to the equilibrium point.*

chemical potentials with blue (spin-up) and red (spin-down) curves. Note that at the interface we have the highest spin accumulation [cf. *Eq. 1.13*], which decays quasi-exponentially on the scale of l_{sf}^N and tends to zero far away from the interface (right side of the figure). At this point, both spin species are equilibrated, and there is no more spin accumulation in the non-magnetic material.

The pure spin current can be detected electrically by using the so-called Non-Local configuration. Figure 1.6(a) represents a typical Lateral Spin-Valve (LSV), consisting of two ferro-magnetic stripes connected by a non-magnetic channel, with the probe configuration for non-local spin current detection. Here, the spin accumulation is created at F1/N, by the flow of electrons, and is further detected at the distance L, using a second F2/N interface [46, 47]. Figure 1.6(b) shows the electro-chemical potential landscape for this kind of configuration, where $\mu_\uparrow$ represents the spin-up and $\mu_\downarrow$ the spin-down population. The output signal is proportional to the difference of the average electro-chemical potential in μ_F F2 and μ_N in N, and it can be defined for each magnetization state (P and AP) as follows:

$$\mu_{P(AP)} = \mu_{F,P(AP)} - \mu_N = \pm\frac{\mu_\uparrow - \mu_\downarrow}{2} \tag{1.14}$$

The sign on the right-hand side of the equation 1.14 depends on the magnetic state of the ferro-magnetic detector. The two possible states of $\mu_{P(AP)}$ are displayed in figure 1.6(b) by the green lines in F2. The output voltage is proportional to the difference of electro-chemical potentials for both magnetic configurations (P and AP):

$$V_{as}^{P(AP)} \sim \pm(\mu_P - \mu_{AP})/2e = \pm\Delta\mu/2e \tag{1.15}$$

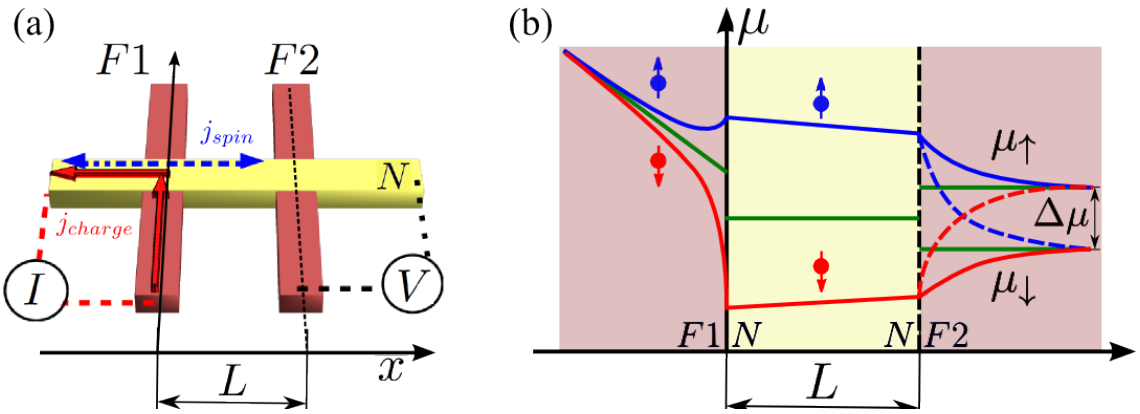

Figure 1.6: *(a) Schematic representation of the* Non-Local *probe configuration in the LSV. The charge current represented by the red arrows is drain-out on the left side of the F1/N interface, while the pure spin current diffuses on both sides in N. A potential drop* V_{sa}^{AP} *develops at the second interface. In contrast to the Local probe configuration we will detect only the spin related phenomena as there is no charge current flowing through the central part of the non-magnetic channel. (b) Electro-chemical potential landscape in the* Non-Local *probe configuration. Blue color stands for spin-up, red for spin-down population, green is the average spin electro-chemical potential. One can notice that the charge current contribution is indicated by the slope in F1, while in N (on the right side from F1/N interface) and in F2, there is no charge current flow, what removes the slope in the average spin electro-chemical potential. For the spin-up population coming from F1, it is more difficult to enter F2 as the magnetization direction is opposite, therefore the electro-chemical potential for spin-up is higher than that for spin-down which passes the F2/N interface more easily.*

One can notice that this voltage does not contain any offset signal and depends only on the spin related phenomena (spin accumulation), without charge related spurious effects, like in the case of GMR type measurements (for instance the ohmic loss).

The main difference between the Local and Non-Local configurations is that in the GMR probe configuration there is no spatial separation of the charge and spin currents. This means that the output signal will be influenced by charge current effects (like anisotropic magneto-resistance, Joule heating, Hall effect etc.) adding an offset voltage to the detected signal. Moreover, the charge current, in the case of GMR type measurements, is passing through two F/N interfaces polarizing current at both of them, contrary to the NL type measurements where it is flowing only through one of the interfaces. Thus the output signal of the local measurements is the double of the one from NL (cf. *Chapter 4*).

An alternative description, based on the band structure representation, can be also used for the understanding of the non-local detection of the spin accumulation. Figure 1.7 shows the "d" band structures scheme for the ferro-magnetic and non-magnetic material. Depending on the magnetic state of the ferro-magnetic detector F2, the Fermi level in F2, aligns with the minority (anti-parallel) or majority (parallel) spin population injected in the non-magnetic metal. This corresponds to the generated voltage V_{F2}^{AP} and V_{F2}^{P} respectively. The total voltage, related to the spin accumulation in N, can be thus defined as $V_{sa} = (V_{F2}^{P} - V_{F2}^{AP})/2$.

Figure 1.8 represents the typical output signal V/I as a function of the external magnetic

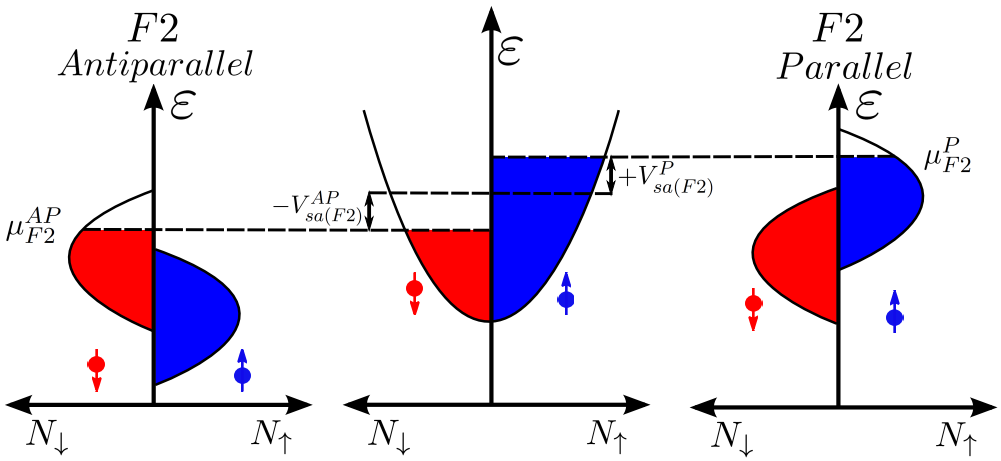

Figure 1.7: *Schematic representation of the "d" band structures in the detector (F2) and the non-magnetic channel (N), for two magnetic states of F2. The spin accumulation in N can be related with the difference of voltages $V_{F2}^{P} - V_{F2}^{AP}$ corresponding to P and AP configuration, in respect to the magnetization direction of the injector.*

field for (a) the Non-Local and (b) Local probe configurations. The external magnetic field is swept along the direction of the ferromagnetic stripes (easy axis). The red curve is a schematic representation of the output signal while sweeping the external magnetic field from the positive to the negative field values, and the blue one for the opposite sweep direction. For the GMR probe configurations, depending on the relative orientation of the ferromagnets magnetization, two different levels of output signal will be recorded as explained in *Section 1.3*.

Similarly, for the Non-Local probe configuration two levels of the output signal will appear. In the parallel state of the magnetization (P) the output signal will be positive in respect to zero voltage, reflecting the number of the majority spin population. Then when the direction of the ferro-magnetic detector is switched to the opposite one (AP state), the minority spin population is probed at F2/N interface, giving a negative signal in respect to zero.

In the case of NL probes configuration [cf. *Fig. 1.8(a)*] no offset signal will be recorded, and therefore the output signal is centered through zero. This configuration is then more sensitive to small effects as it removes some noises coming from high resistance elements and MR of the electrodes. We will now concentrate on a quantitative description of the output signal for the NL configuration.

In order to quantitatively describe the output signal of NL probe configuration, presented in figure 1.8(a), one can use Eq. 1.8 imposing the boundary conditions for a LSV structure, as proposed by Takahashi *et al.* [14, 13]. In that case, the non-local spin signal ΔR_s based on a one-dimensional spin diffusion model is then given in the general form:

$$\Delta R_s^{Takahashi} = \frac{R_N(P_F\frac{R_F^*}{R_N} + P_{int}\frac{R_{int}}{R_N})^2 exp(-L/l_{sf}^N)}{(1 + 2\frac{R_{int}}{R_N} + 2\frac{R_F^*}{R_N})^2 - exp(-2L/l_{sf}^N)} \tag{1.16}$$

where: P_F and P_{int} are the bulk and the interface spin polarizations of the ferromagnet, R_{int} stands for interface resistance and $R_{N(F)}^{(*)} = \rho_{N(F)}^{(*)} l_{N(F)}/A_{N(F)}$ represents the non-magnetic

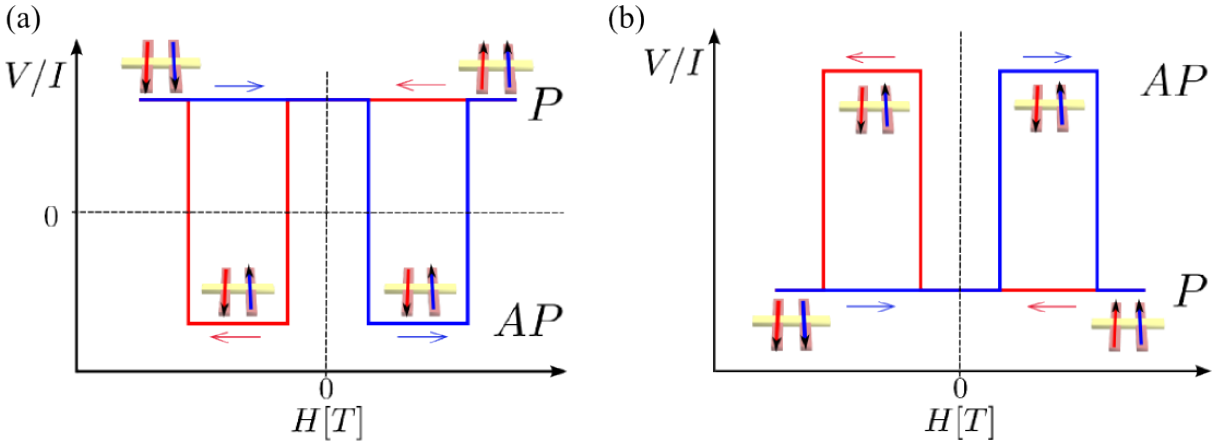

Figure 1.8: *Expected V/I output signal as the function of external magnetic field for (a) Non-Local and (b) Local (GMR) probe configuration in the LSV device. The magnetic field is swept along the ferromagnetic nano-wires from the negative to positive field values (blue) and in the opposite direction (red). When one of the ferromagnets switches, this results in the anti-parallel state (AP), a change in the output signal is observed to lower (NL) or higher (GMR) state. Then the parallel (P) magnetization state is recovered when the second ferromagnetic wire switches. While in NL we are detecting only spin related effects, without an offset, the signal output is centered around zero. In GMR measurements the resistance of the device will contribute to the output signal.*

(ferromagnetic) spin resistances. Here $A_N = w_N \times t_N$ and $A_F = w_F \times w_N$ stand for the cross-section areas of respectively non-magnetic and ferromagnetic material. The effective spin relaxation in the ferromagnet occurs only at short distances [68], therefore its cross section can be considered to be the one of the F/N junction (defined by the widths of N and F). Parameters $\rho^{(*)}_{N(F)}$ ($\rho^*_F = \frac{\rho_F}{(1-P_F^2)}$), $l_{sf}^{N(F)}$, t_N, $w_{N(F)}$ stand for the resistivity, the spin diffusion length in the normal material N (in the ferromagnetic material F), the thickness, the width of the ferro (F) or non-magnetic (N) material respectively.

When assuming transparent interfaces (neglecting interface resistance) this equation can be further rewritten in the simpler form:

$$\Delta R_s \backsimeq \frac{2P_F^2}{(1-P_F^2)^2}\frac{R_F^2}{R_N}[sinh(\frac{L}{l_{sf}^N})]^{-1} \tag{1.17}$$

This model will be of a particular interest for the discussion developed in the following chapter, on how the spin signal amplitude can be increased.

Chapter 2

Optimization of the spin signal amplitude in metallic lateral spin-valves with transparent interfaces

In this chapter, an efficient way to increase the spin signal in all-metallic lateral spin-valves with metallic contacts will be presented [69]. This optimization was done by carefully choosing the geometry, the materials and the fabrication method of the sample. Numerical calculations using 1D analytical models will be shown in order to evidence the importance of those aspects and their influence on the amplitude of the spin signal.

The experimental results on LSVs based on Al, Cu and Au magnetic channel will be presented, where the distance separating the ferro-magnetic electrodes was varied so as to extract material parameters l_{sf}^{N} and P_{eff}. Analysis combining 1D model and the transfer matrix approach, taking into account the bulk and the interface effects, was carried out. These evaluations were be checked by the use of the Finite Element Method in order to refine and test the validity of the data analysis. This combination of methods provides a powerful tool for spin transport characterization.

2.1 Introduction

In a first approximation, the spin signal of a LSV can be calculated theoretically on the basis of a 1D diffusive transport modeling [70]. As seen in *Chapter 1*, in the case of transparent contacts (i.e. when the interface resistance is much smaller than the spin resistance of the ferromagnetic and non-magnetic material: $R_b \ll R_F, R_N$), the amplitude of the spin signal can be defined as follows:

$$\Delta V/I \backsimeq \frac{2P_F^2}{(1-P_F^2)^2}\frac{R_F^2}{R_N}[sinh(\frac{L}{l_{sf}^N})]^{-1} \tag{2.1}$$

Where $R_{N(F)}$ is the spin resistance in N (F), the resistance experienced by the spin current while diffusing over a distance equal to the spin diffusion length ($l_{sf}^{N(F)}$). That is expressed as

$R_{N(F)} = \rho_{N(F)} l_{sf}^{N(F)} / A_{N(F)}$, with $A_N = w_N \times t_N$, $A_F = w_F \times w_N$, where $\rho_{N(F)}$, $l_{sf}^{N(F)}$, t_N, $w_{N(F)}$, $A_{N(F)}$ are respectively the resistivity, the spin diffusion length in the normal material N (in the ferromagnetic material F), the thickness, the width and the cross-sectional area of the ferro (F) or non-magnetic (N) material. This approach is valid in the case where $l_{sf}^{F} \ll t_F, w_F$ (which is valid for all nano-structures presented in this thesis). In the case of permalloy (Py) ferro-electrodes, the relaxation process of the spin accumulation takes place at very short distances ($l_{sf}^{Py} = 5.5\,nm$) [68]. One can then suppose that the active cross-section area for the ferromagnet is determined by the junction size: $A_F = w_F \times w_N$. Here P_F is the spin polarization of F, L is the distance between injector and detector (distance from center to center of the F/N crosses). Nevertheless, P_F should be considered as an effective spin polarization P_{eff} to take into account the interface effect, especially the depolarization by the spin-flip. This reduces the value of P_F from bulk, as argued in [71].

There are three important aspects that have to be taken into account in order to increase the spin signal amplitude. They come naturally from Eq. 2.1 and consist in **geometry**, **interface** and **materials** used in a LSV structure. We will now concentrate on a more detailed description of these aspects.

2.2 Geometry

As it can be noticed in Eq. 2.1, the geometry manifests itself first by the $\frac{R_F^2}{R_N}$ ratio.

To increase the spin signal amplitude, one has to increase R_F and to decrease R_N (while keeping high l_{sf}^{N}), what can be done from the point of view of geometry, by first reducing the width w of the wires. For the geometry of the nano-structure in which the nanowires have the same widths: $w_N = w_F = w$, we have:

$$\frac{R_F^2}{R_N} \sim \frac{A_N}{A_F^2} = \frac{t_N}{w^3} \tag{2.2}$$

As it can be noticed in this prefactor, the width, since it is in cubic relation, has stronger influence on the spin signal amplitude than thickness t_N, contributing linearly.

Figure 2.1 shows 1D numerical calculations, using Eq. 2.1 of the spin signal amplitude for various geometries of the nano-device. The distance between the ferromagnetic electrodes is fixed to be $L = 500\,nm$, the resistivity and the effective spin polarization correspond to the experiment performed at $T = 77\,K$: (respectively: $\rho_{77K}^{Al} = 1.5\,\mu\Omega.cm$, $\rho_{77K}^{Py} = 11.8\,\mu\Omega.cm$, $P_{eff} = 0.35$, cf. *Chapter 3*). We can notice that shrinking the width of the nanowires can lead to a strong increase of the signal. When taking into consideration commonly used geometries, where the wires widths are larger than $200\,nm$ [53, 54, 72, 73], one could expect the spin signal amplitude to be very small (according to the calculations presented in *Fig. 2.1*). The spin signal amplitude can be increased up to 60 times by using small width of the nano-wires what represents the case of a decrease of the width from $200\,nm$ down to $50\,nm$. In order to evidence experimentally the validity of these expectations, nano-devices with different non-magnetic channel widths were prepared. In this experiment the width of the ferromagnetic wires was fixed to $50\,nm$.

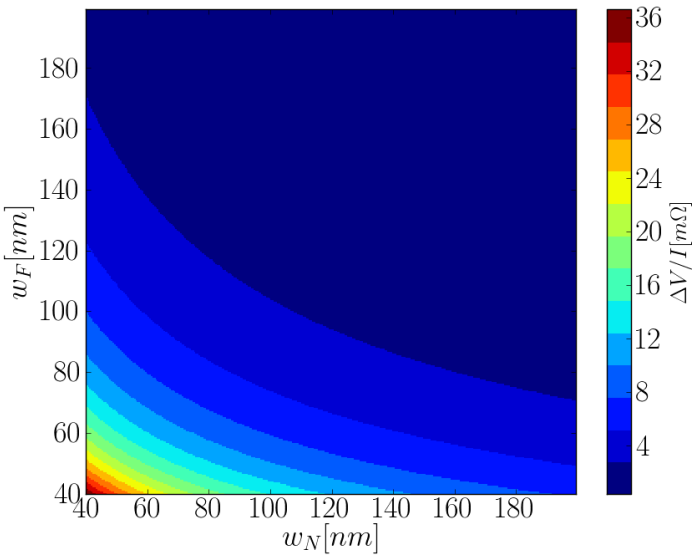

Figure 2.1: *Numerical calculation of the spin signal amplitude as a function of the width of ferromagnetic and non-magnetic nanowire according to [cf. Eq. 2.1]. One can notice that the shrinking of the nano-wires leads to a drastic increase of the spin signal amplitude.*

In the designed LSV [cf. *Fig. 2.2*], both ferromagnetic and normal wires are $50\,nm$ wide in order to obtain high spin signal amplitudes. The width has been reduced to increase the geometrical prefactor appearing in Eq. 2.1, to such a point that the quality of the lithography was not affected. This is an important aspect to increase the amplitude of the spin signal and to target efficient spin injection and detection.

The two $15\,nm$ thick ferromagnetic electrodes (Py) are connected by a non-magnetic $60\,nm$ thick Al (Cu or Au) wire [cf. *Fig. 2.2*]. The probe configuration for non-local spin signal measurements or GMR are illustrated in Fig 2.3 (b) and (c) respectively.

Figure 2.3(a) presents typical experimental data of V/I signal as a function of external magnetic field, recorded at $T = 77\,K$ for Py/Al based nano-device with $L = 200\,nm$. The red curve represents a nano-structure with larger width of the non-magnetic channel ($w_N = 100\,nm$) and the blue one stands for $w_N = 50\,nm$. The spin signal amplitude is clearly increased from $8\,m\Omega$ to $21\,m\Omega$. One can notice a good agreement with the numerical simulations from figure 2.1, where the ratio of the spin signal amplitudes for similar nano-wires is $10/22\,m\Omega$.

2.3 Interfaces (multi-level and multi-angle nanofabrication methods)

Apart from the geometry of the device, the second parameter, that needs to be considered for the optimization of the spin signal amplitude, is the effective spin polarization P_{eff} [cf. *Eq. 2.1*]. To optimize P_{eff}, the F/N interfaces have to be clean, without any contamination that could cause depolarization of the spin when crossing this interface [74]. There are two basic methods

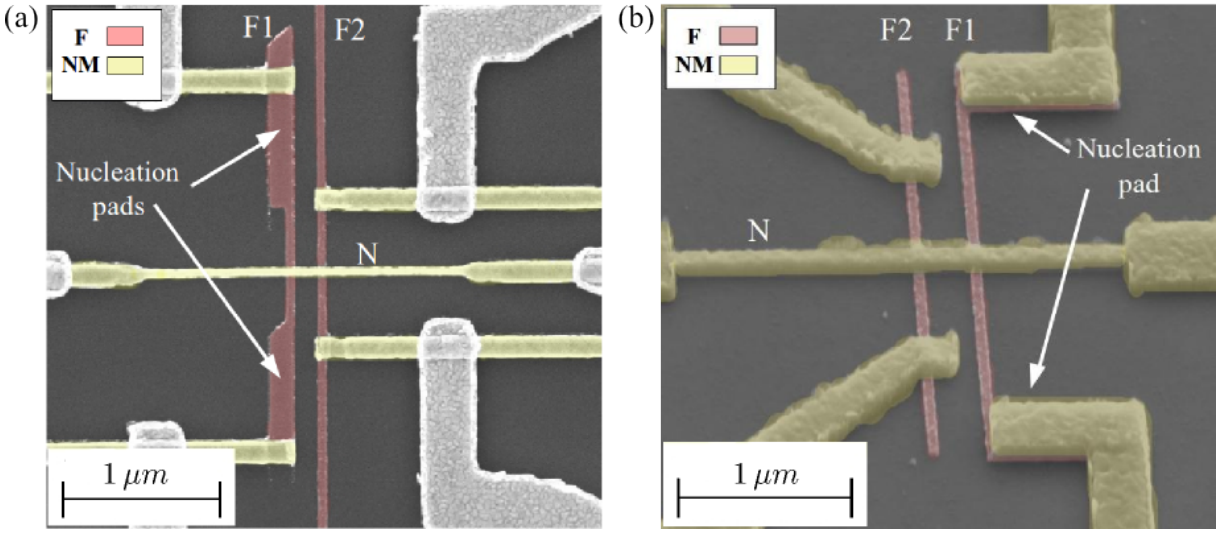

Figure 2.2: *SEM images of the Lateral Spin-Valve nano-structure made by (a) multi-angle evaporation technique and (b) multi-level technique (cf. Section 2.3). Two ferro-magnetic (F)* 15 *nm thick nanowires are connected by a non-magnetic (N)* 60 *nm thick channel. One of the magnetic stripes (F1) contains nucleation pads in order to facilitate the domain wall nucleation process leading to the lowering of its reversal field.*

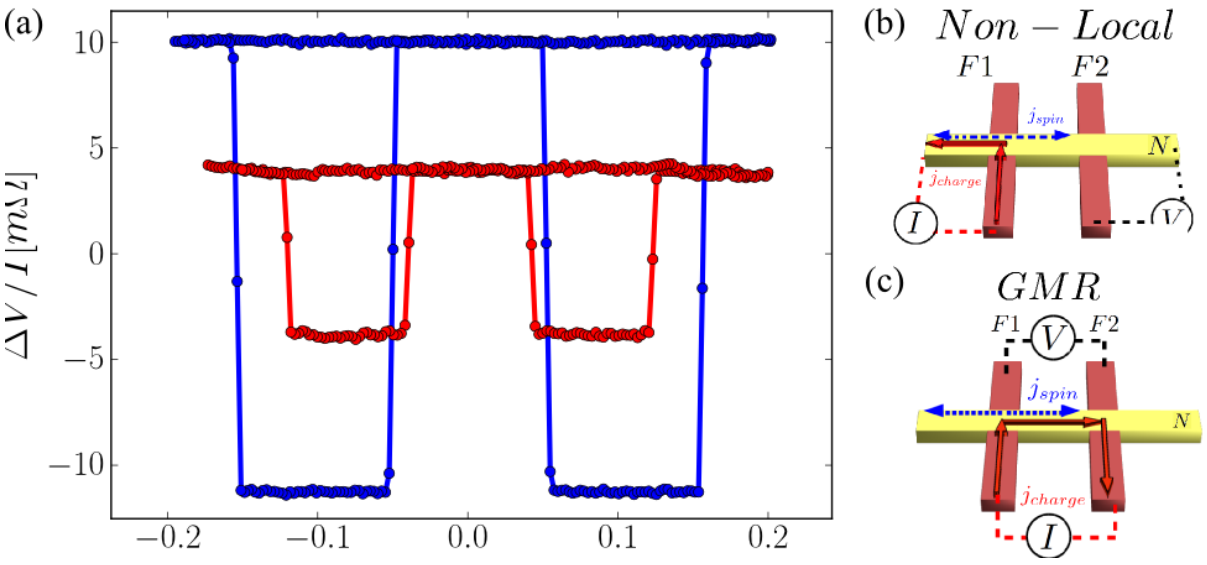

Figure 2.3: (a) *V/I signal in the Non-Local probe configuration as a function of the external magnetic field for Py/Al nano-structures with* $L = 200\,nm$*, recorded at* $T = 77\,K$*. In red, data for nano-device with a* 100 *nm and in blue with a* 50 *nm wide N channel. Increase of the amplitude of the spin signal is of the order of 100%, when reducing the N channel width by a factor of 2. (b) The Non-Local and (c) GMR probe configuration schematics in LSVs.*

	$\Delta V/I\,[m\Omega]$	$T\,[K]$	$L\,[nm]$	$ref.$
Au	0.025	10	150	[45]
	2	15	100(400)	[75]
Cu	2.5	77	250	[76]
	0.7	300	200	[74]
Al	1.3	4.2	250	[48]

Table 2.1: *Examples of typical spin signal amplitudes $\Delta V/I$ for lateral spin-valve with Al, Cu and Au (with Py electrodes), taken from literature.*

of nano-fabrication of the lateral nano-structure using lithography processes that can be used for this purpose. Both of them will be discussed in the following.

2.3.1 Multi-level method

The first, and a most used method (named the multi-level method) consists in two sets of processes: lithography, deposit and lift-off [cf. *Appendix B*] of the F material, followed by the same steps for the N. The first difficulty in the lithography process is that for each material the sample needs to be realigned using special realignment marks. This, eventually, brings uncontrolled shifts in the nano-device patterns, especially for the overlaps between different e-beam lithography levels. These problems are usually overcome when increasing the nano-structures size or the gap between wires (thus decreasing the spin signal amplitude). In our samples we were able to optimize the realignment conditions in order to reduce the alignment error down to $20\,nm$. The multi-level method brings forward another important aspect that involves the cleaning by ion milling of the ferromagnetic/non-magnetic interface before the deposition of the nonmagnetic channel. It is necessary, as the non-controlled oxidation and contamination by resist residues, leading to spin depolarization at the F/N, interface exist after the first step. This leads to the decrease of the spin signal amplitude down to its disappearance.

Several nano-structures using the same technique and similar design, with Al non-magnetic channel, were fabricated. A Scanning Electron Microscope (SEM) image of the typical nano-device is presented in Fig. 2.2(b). The widths of the ferro-electrodes and non-magnetic stripe are $w_F = w_N = 50\,nm$. In this geometry, the ferro-magnetic stripes are connected by a $80\,nm$ thick non-magnetic Al channel.

Typical spin signal amplitudes for LSV nano-structures with transparent interfaces are presented in table 2.1. The highest value reported up to now for similar type of nano-devices was achieved for Py/Cu nano-pilars type structures by Yang *et al.* [77] yielding $18.5\,m\Omega$, with a shadow fabrication approach. A high spin signal amplitude was also reported for Py/Ag reaching up to $10\,m\Omega$ at $77\,K$, the reason being high interface resistance. However, the typical values of the spin signal do not overcome $2\,m\Omega$, according to the calculation presented in Fig. 2.1, with $w = 100\,nm$, and in a literature overview.

Figure 2.4 represents the V/I signal in the Non-Local (a) and Local (b) probe configurations [cf. *Fig. 2.3(b-c)*] as a function of magnetic field for nano-devices made by the multi-level nanofabrication method. Before the deposition of the normal channel, connecting the two ferro-

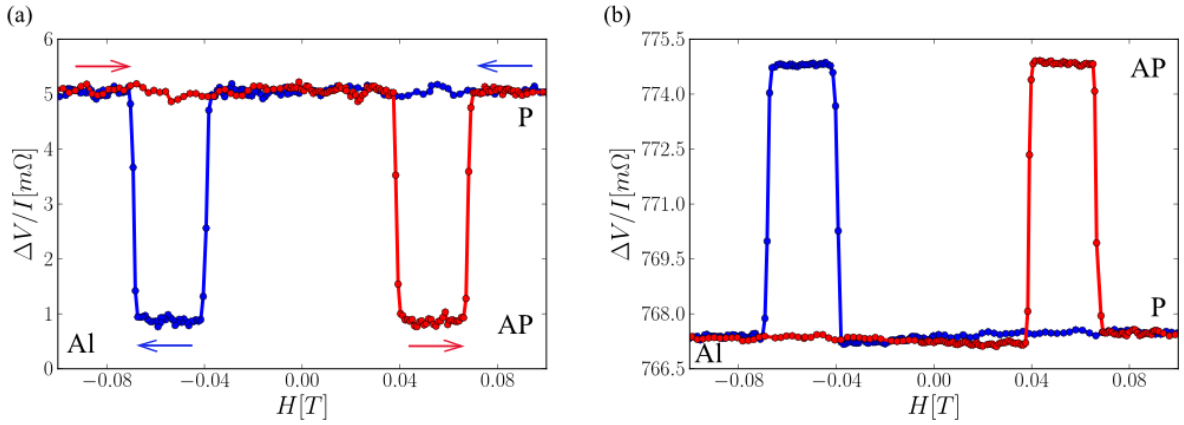

Figure 2.4: *V/I measurements in (a) Non-Local and (b) Local (GMR) probe configurations shown in Fig.2.3(b-c), recorded at $T = 77\,K$ for Py/Al nano-device made using the multi-level nano-fabrication method. The distance from center to center of the ferro-electrodes is equal to $L = 200\,nm$. The amplitude of variation is (a) $4.16\,m\Omega$ and (b) $7.55\,m\Omega$ for Non-Local and Local configuration respectively* [cf. *Fig. 2.3(b-c)*]. *Blue and red curves correspond to positive and negative magnetic field sweep directions.*

magnetic electrodes, the interface needs to be cleaned by ion-milling. The duration of the ion-milling process has been optimized in order to obtain the highest spin signal, similarly to the work presented by Yakata *et al.* [78] and Jedema *et al.* [50]. In our approach, the optimum time was found to be $50\,s$ using $400\,V$ acceleration voltage. However, it can vary with the geometry of the nano-structure and with the nano-fabrication method, as the resists openings can be different for different designs. The amplitude of the spin signal yields $4.16\,m\Omega$ in NL compared to $7.55\,m\Omega$ in the GMR configuration [cf. *Fig. 2.3(b-c)*], at $77\,K$, which are the highest values reported so far using this method for Py/Al based LSV with transparent junctions [48, 46, 47, 79, 53].

In order to avoid the uncontrolled oxidation at the F/N interface, one can use the so-called shadow evaporation technique, which will be described in the following.

2.3.2 Multi-angle method

In the case of the shadow evaporation technique [36, 77, 80], the sample is kept in vacuum between the F and N wire depositions and hence for the F/N interface fabrication. This ensures good contacts quality, without the need of interface cleaning between the deposition of the ferromagnet and of the non-magnetic channel.

2.3.2.1 Standard shadow method

The most commonly used shadow technique is based on a bi-layer resist approach, where one uses two resists of different molecular weight [81]. The under-layer, of a lower molecular weight can be exposed and developed while the over-layer is unaffected. This results in the formation of very large undercuts due to its higher sensitivity.

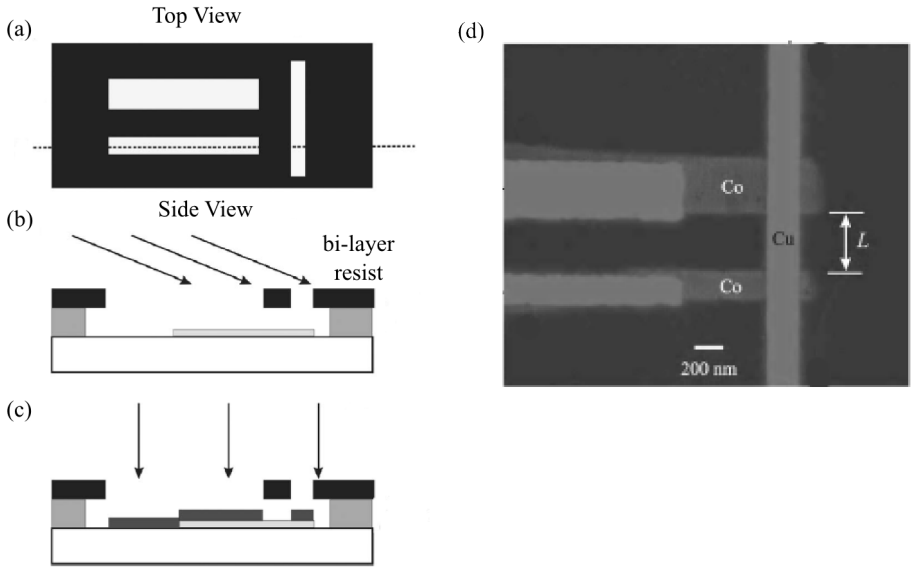

Figure 2.5: *Schematic representation of the commonly used shadow evaporation technique. (a) top view of the bi-layer resist mask with patterned regions in white. (b) Deposition of one material at an angle respect to the normal direction to substrate plane. (c) Deposition of the second material using the shadowing effect of the top resist layer. (d) SEM image of typical Co/Cu nano-structure made using shadow evaporation method. Extracted from [80].*

First, a bi-layer resist is deposited on a substrate [cf. *Fig. 2.5(a)*]. This step is followed by the e-beam insolation of the desired pattern. Then one of the two materials is evaporated at an angle with respect to the direction normal to the substrate [cf. *Fig. 2.5(b)*], through a bi-layer, in order to form two straight continuous nano-wires. The evaporation of the second material is done perpendicularly to the substrate plane [cf. *Fig. 2.5(c)*]. The top layer induces a shadowing effect which results in the gap forming two separated nano-stripes of the second material. A typical nano-structure, made by using the standard shadow evaporation technique for Co and Cu, is represented on the SEM image in Fig. 2.5(d).

The main advantage of this technique is that the active part of the structure is fabricated in the vacuum, assuring clean interfaces between the two materials. However, there are also some limitations. The nano-structure made with this method is limited in the number of terminals (3) that can connect a single junction, since otherwise the nano-device would be shortcut with the same material. Fig. 2.5(d) represents a nano-structure with three terminals connected to a single interface. Moreover, it is not possible to form small gaps between parallel wires (L in *Fig. 2.5(d)*). Therefore, a single resist multi-angle evaporation technique was developed for a more flexible nanofabrication approach.

2.3.2.2 Multi-angle shadow method

In this technique, one single Poly-Methyl Methacrylate (PMMA) layer is used. The central part of the device is patterned entirely in one step, using electron beam lithography without distinction between the ferromagnetic and non-magnetic wire parts. We make high aspect resist openings in

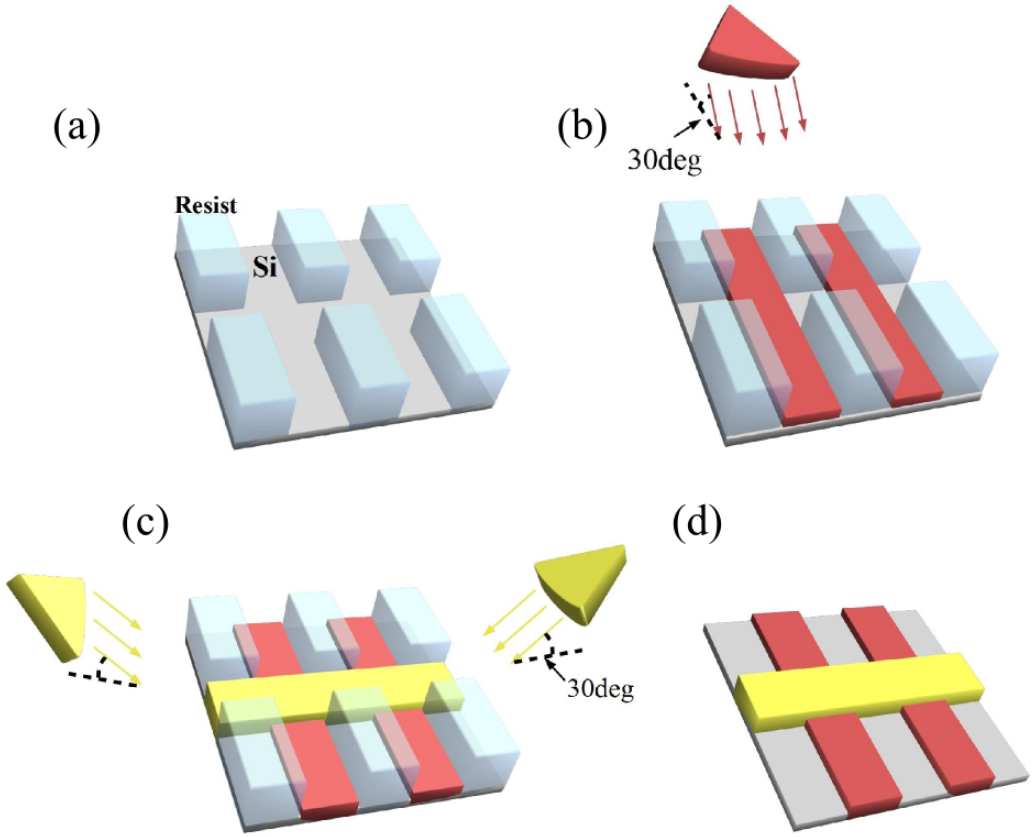

Figure 2.6: *Schematic representation of the multi-angle evaporation method. High aspect ratio openings of a single resist are used for in vacuum processing of the active part of the nano-structure. (a) The central part of the device is patterned by the means of e-beam lithography, followed by (b) the evaporation of the ferromagnetic material at 30 degrees with respect to the direction normal to the substrate plane. Then (c) the sample is rotated by 90 degrees* in-plane *and a non-magnetic material is evaporated at 30 degrees and -30 degrees.*

the PMMA layer, and design the wires in a cross geometry [cf. *Fig. 2.6(a)*]. When depositing at a suitable angle, this allows depositing material in only one of the wire orientations, thus taking advantage of the shadowing effect in the perpendicular trenches. This approach does not need a bilayer resist, and big undercuts formation for lift-off process, as it prevents undesirable material deposition at the junction between the substrate and the resist. This allows us to build a more flexible device geometry with numerous electrodes and a much smaller gap between parallel wires (down to $50\,nm$ in our case). Additionally, the presence of the nucleation pads on one F wire allows us to obtain a quite stable anti-parallel state, without having to increase one wire width and thus decreasing the spin signal [cf. *Sec. 2.4.2*].

Permalloy stripes (Py) are evaporated at an angle of 30 degrees [cf. *Fig. 2.6(b)*]. Since trenches in the PMMA are $300\,nm$ deep and their maximum width is $140\,nm$ (the reservoir), all trenches perpendicular to the deposition axis are protected against deposition by a shadow effect. Then the sample is rotated in its plane by an angle of 90 degrees, and the non-magnetic material (Al, Cu or Au) is deposited with the same 30 degree angle [cf. *Fig. 2.6(c)*]. This time, however, one needs to evaporate from both directions in order to avoid the formation of a gap due to the shadowing effect by the first deposit. This can be done using sequences of evaporations at +/- 30 degrees. All wires have a sharp apex to limit the deposition of the material on the side of the resist, thus facilitating the lift-off process.

This technique allows for the formation of ultra-clean interfaces. The microscopic Ti(5 nm)/Au(100 nm) contact electrodes are either deposited before or after the fabrication of the active part of the device.

2.4 Materials dependence

Beyond the reduction of the wire width to increase the spin resistances, and the development of techniques for in-vacuum interface fabrication, the third parameter that can be changed to maximize the spin signal amplitude is the choice of materials. This parameter turns out to manifest itself through the terms P_{eff}, $\rho_{N(F)}$ and l_{sf}^N, which are present in the resistance ratio and in the hyperbolic sinus part of Eq. 2.1. By using a non-magnetic material with short l_{sf}^N and thus low spin resistance, as in Au [37], the spin resistance ratio and thus the spin signal could be increased as it will be easier to inject spins into N. However, there is an opposite effect of l_{sf}^N on the spin signal, which comes from the $[sinh(\frac{L}{l_{sf}^N})]^{-1}$ factor. We thus choose to study Al and Cu, which possess long l_{sf}^N, and compare these materials to Au.

2.4.1 Spin signal for different materials

Measurements were performed at room temperature and at $77\,K$ with the magnetic field oriented along the ferromagnetic wires. Three types of nano-structures were studied, based on Al, Cu and Au non-magnetic channel, fabricated by the multi-angle evaporation method.

The V/I non-local signal as a function of magnetic field is shown in Fig. 2.7(a), for an Al-based LSV at $77\,K$. For this LSV, the center to center distance L between the injector and

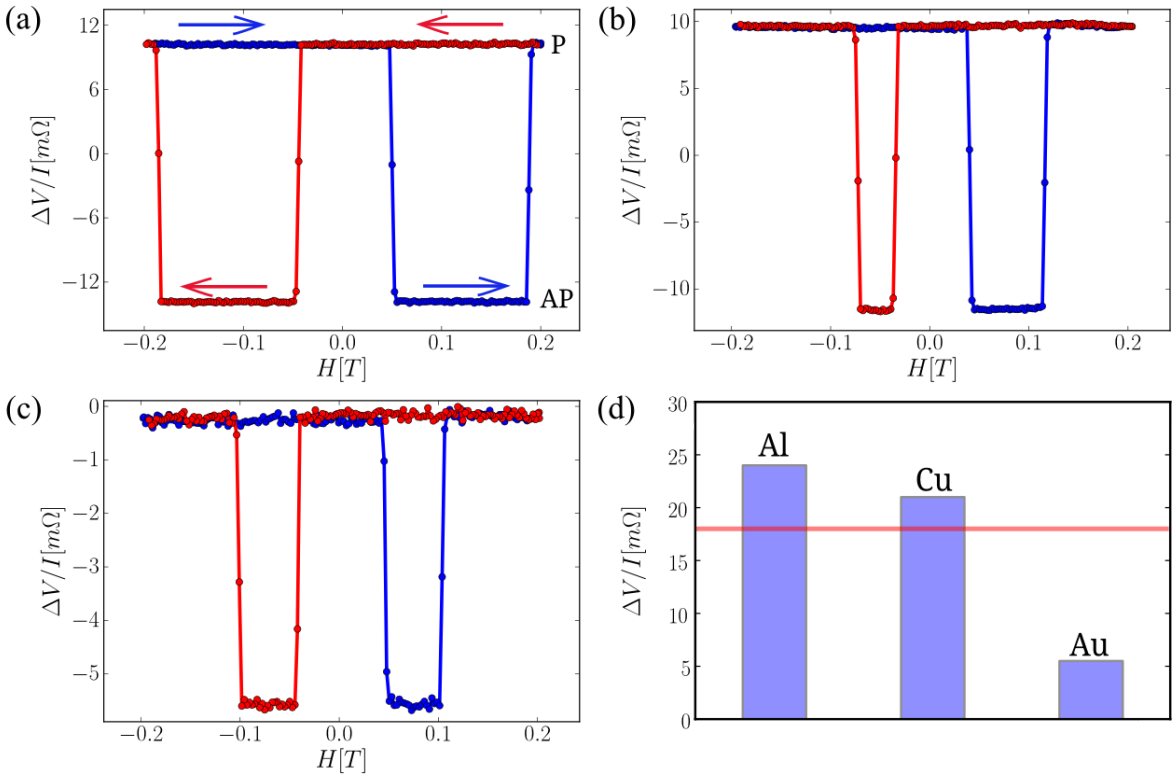

Figure 2.7: *Non-local magneto-transport measurements for three types of Lateral Spin-Valves with (a) Al, (b) Cu, (c) Au non-magnetic channel. Data-points were recorded at* $T = 77\,K$ *for the same nano-devices geometry:* $L = 150\,nm$ *(distance from center to center of the ferromagnetic electrodes), with nano-wires of* $50\,nm$ *width. (d) Comparison of the spin signal amplitudes from three N materials. The red line representing the highest value reported in the literature [77].*

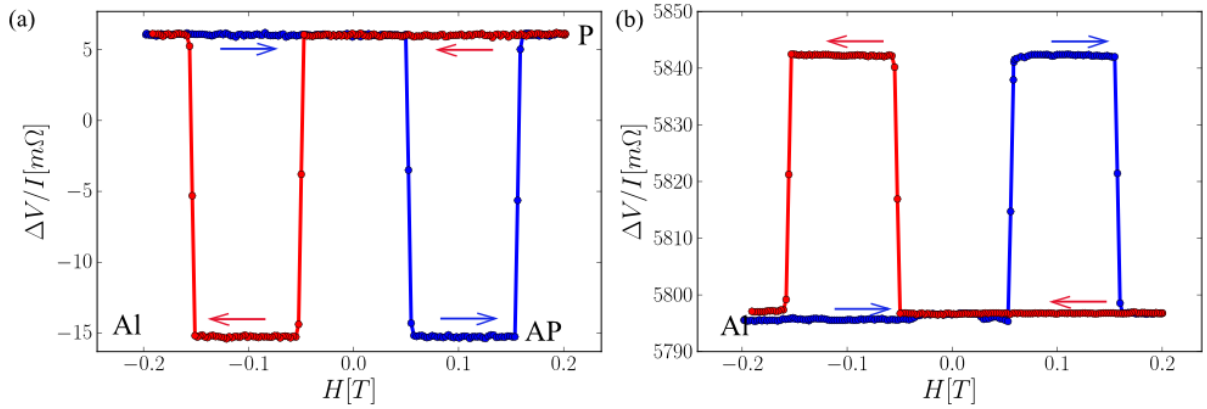

Figure 2.8: *V/I measurements in (a) the Non-Local and (b) Local (GMR) probe configurations (shown in Fig.2.3(b-c)) recorded at $T = 77\,K$, for Py/Al nano-device made using the multi-angle evaporation method. The distance from center to center of the ferro-magnetic electrodes is equal to $L = 200\,nm$.*

the detector is equal to $150\,nm$. A clear spin signal can be seen, with a well-defined plateau in the anti-parallel magnetization state of the ferromagnetic electrodes. The spin signal is equal to $\Delta V/I_{Al} = 24\,m\Omega$, which is the highest value reported up to now for ohmic interfaces by Yang *et al.* [77], yielding $18\,m\Omega$, by mixing pillar nanofabrication and lateral connection in vacuum.

Moreover, this result is in agreement with the GMR measurements (local detection) presented in Fig. 2.8(b) for $L = 200\,nm$, where the resistance change for GMR is of $48\,m\Omega$ instead of $21\,m\Omega$ for the spin signal of Fig. 2.8(a). Note that the GMR/spin signal ratio is close to the expected value of 2, which corresponds to the sum of the spin signals at the two identical interfaces [82]. Note that in the Non-Local configuration the current path and the voltage lines are a little bit more separated than in the local GMR measurement, which may explain why the ratio is a little bit smaller than 2.

Spin signal measurements were also performed for Cu-based devices, with $L = 150\,nm$. Clear spin signals were observed, up to $9\,m\Omega$ at room temperature [cf. *Fig. 2.9(b)*] and $21\,m\Omega$ at $77\,K$ [cf. *Fig. 2.7(b)*]. Interestingly, for Py/Cu, made by the multi-level method, we obtained very recently signals up to $18\,m\Omega$, demonstrating a very good cleaning of the F surface.

For Au-based devices, and still with a width L of $150\,nm$, a much smaller spin signal amplitude was observed, the magnitude being of the order of $1.5\,m\Omega$ [cf. *Fig. 2.9(a)*] and $5.5\,m\Omega$ [cf. *Fig. 2.7(c)*] at $300\,K$ and $77\,K$ respectively. Also, the small spin signals obtained using Au can be accounted by the equations of 1D models for the case of Ohmic contacts: the amplitude of spin signals is mostly governed by the *sinh* part of the equation, even for as small as possible L/l_{sf} ratio. Note that in the case of Au $L > l_{sf}^{Au}$.

The ratios in amplitudes of the spin signals between the liquid nitrogen and room temperatures of almost 3.5 times for Au and 2.3 times for Cu come from the decrease of l_{sf}^{N} and $P_{eff.}$, when going from $77\,K$ to $300\,K$. In this case, the scattering mechanism [cf. *Chapter 1*] of the spins on phonons becomes dominant, resulting in shorter spin diffusion lengths, smaller effective

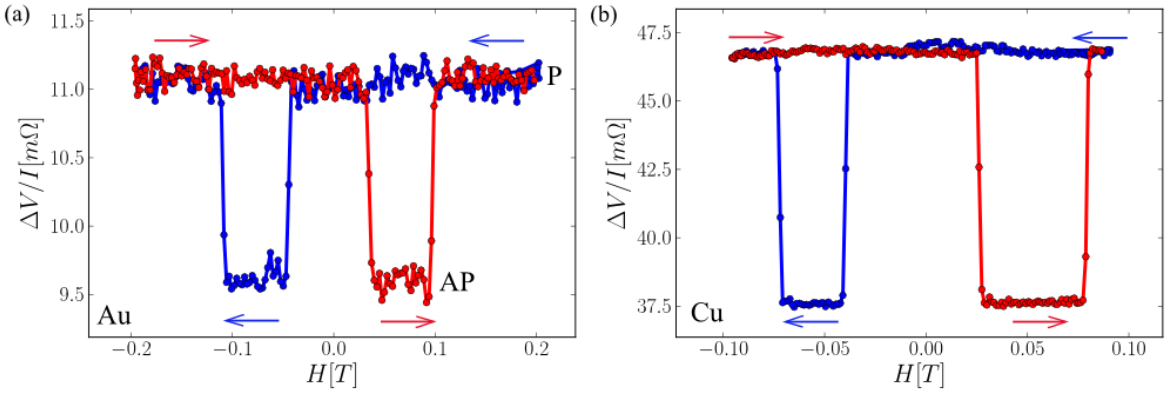

Figure 2.9: *V/I measurements recorded at $T = 300\,K$ for (a) Py/Au and (b) Py/Cu nano-structures using the Non-Local probe configuration for $L = 150\,nm$ (cf. Fig.2.3(b)).*

mat.	$\rho_N\,[\mu\Omega.cm]$	$l_{sf}^N\,[nm]$	$T\,[K]$	$\rho_N l_{sf}^N\,[\Omega.nm^2]$	$R_N\,[\Omega]$	*ref.*
	5.24	60 ± 15	300	3144	1.26	[83]
Au	3.5	90 ± 20	77	3325	1.4	*this work*
	2	63	10	126	0.05	[45]
	2.86	300 ± 50	300	8580	3.43	[48]
Cu	2	500	77	10000	2.5	*this work*
	1.41	1000 ± 200	4.2	14100	5.64	[48]
	3.23	600 ± 50	300	19380	7.75	[48]
Al	1.5	600	77	9000	3.6	*this work*
	1.25	1200 ± 200	4.2	15000	6	[48]
Py	26.8	3	300	804	0.32	[83]

Table 2.2: *Summary of material characteristic parameters for Py, Au, Cu and Al from electric transport experiments in LSV nano-structures. The spin resistance is calculated for a cross section area of $50 \times 50\,nm^2$ in comparison with results from other groups.*

spin polarization and higher resistivity.

Figure 2.10 shows results of numerical computation of the spin signal amplitude as a function of the spin resistance and of the l_{sf}^N of N material, following Eq. 2.1. Parameters used to perform this simulation were taken from experiments (a more detailed discussion will be presented in *Chapter 3*): $\rho_{77K}^{Py} = 118\,\Omega.nm$, $P_F = 0.35$, $L = 150\,nm$ and literature: $l_{sf}^{Py} = 5.5\,nm$ [68, 62].

The experimental values for *Au*, *Cu* and *Al* based nano-structures (for more details refer to *Chapter 3*) are presented in table 2.2:

One can find spin signal amplitude values from the numerical calculations which are in the range of $20 - 30\,m\Omega$ for *Al* and *Cu* and of $5 - 10\,m\Omega$ for Au [cf. *Fig. 2.10(a)*]. Nevertheless, the fact that the section does not take into account the additional surface from the side of the F wires, what in this approximation should result in higher spin signal amplitudes values compared to the experiments [74], the experimental results are in a very good agreement with the numerical calculations. Note that the signals amplitude is more influenced by l_{sf}^N than R_N variations. This

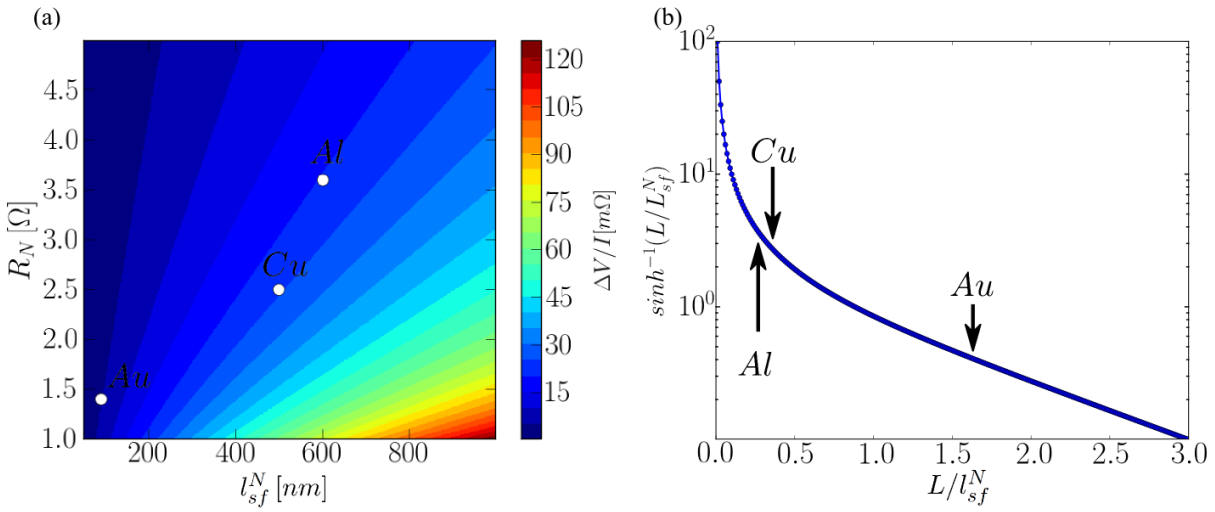

Figure 2.10: *Numerical simulations using simple 1D spin diffusion model [14] of (a) the spin signal amplitude as a function of R_N and l_{sf}^N. Both simulation were performed using values at $T = 77\,K$: $\rho_{77K}^{Py} = 11.8\,\mu\Omega.cm$, $P_{eff} = 0.35$, $L = 150\,nm$, $l_{sf}^{Py} = 5.5\,nm$.* Here, the spin signal amplitudes for Au, Cu and Al are estimated to be around: $8\,m\Omega$, $25 - 30\,m\Omega$, $20 - 30\,m\Omega$ respectively. *(b) $sinh(L/l_{sf}^N)$ as a function of L/l_{sf}^N where $L = 150\,nm$.*

means that the dominating effect comes form the *sinh* part of the equation 2.1 , and that it is more preferable to use materials with large l_{sf}^N rather than materials with small R_N in order to increase the spin signal amplitude.

To summarize the experimental results: in the case of Al and Cu the spin current propagates to longer distances than in the case of Au, however, it is more difficult to inject the spin current into N since $R_N > R_F$. This is not the case of Au, where R_N is much smaller than for Al and Cu, meaning that the spin current polarization in N will be higher. The final effect on the spin signal amplitude comes from both the spin current polarization and the propagation length of the spin currents together. It gives advantage to the material with longer spin diffusion lengths even in the case of shorter separation, i.e. $L = 150\,nm$.

Finally, so as to increase the spin signal amplitude, instead of changing the N materials, one can also vary the ferromagnetic material. This will reflect itself through R_F^2 in the prefactor of equation 2.1. Therefore, to obtain higher spin signals, R_F should be increased, which can be done by using ferromagnets with higher spin diffusion lengths compared to permalloy (Py). Several groups showed experiments on spin injection using various ferromagnetic electrodes: Ni [50], Co [53], CoFe and CoFeAl [84]. While the spin signal amplitude was reported to increase when using Co based ferromagnets, compared to Py ones, up to now, there has been no report on electrical spin injection from Ni ferromagnets. However, we developed the nano-fabrication technique using Ni/Al and Ni/Cu LSV nanostructures by means of the multi-angle evaporation method. No significant or clear results were obtained for those nano-devices, similarly to Jedema *et al.* [50]. The reasons for that are the spin depolarization at the interface (bad interface quality such as interface alloying) and a non-sufficient spin polarization. By using the multi-

angle evaporation technique, we were able to fabricate ultra-clean interfaces with efficient spin injection as proved for Py/Al, Py/Cu and Py/Au nano-structures with low interface resistance. This suggests that the main problem is due to the weak polarization of Ni.

2.4.2 Permalloy ferro-magnetic electrodes

In order to detect a spin signal in LSV, one needs to establish the anti-parallel state of the magnetization orientation of the ferromagnetic wires, what can be achieved by choosing a specific geometry of the F wires. This aspect of the magnetic properties of the nano-device can be studied by means of the micro-magnetic simulation, discussed in the following.

The geometry of the ferromagnetic electrodes, ensuring clearly different reversal fields, was anticipated using the micro-magnetic simulations in the frames of Object Oriented Micro-Magnetic Framework (OOMMF) based on the Landau–Lifshitz–Gilbert (LLG) equation [85]. The difference in the reversal fields is necessary so that a distinguishable anti-parallel state of magnetization could be established, allowing that a clear spin signal could be observed. Different geometries were studied in order to choose the most convenient one.

Figure 2.11 shows the simulations results of the magnetization curve M(H). In this case, we choose the width of both ferromagnets to be $w_F = 50\,nm$. The inset of figure 2.11 represents the geometry of the Py nano-wires. The blue line corresponds to the projection of magnetization of the nano-wire (M_y) on the Y axis, along the sweep of the external magnetic field, normalized by the saturation magnetization (M_s). Since the two ferro-magnetic electrodes are treated as one system, two switching events occur (marked by red circles), which are around $40\,mT$ and $110\,mT$. This reflects the change in magnetization orientation of the ferromagnet F1 having the nucleation pads, then followed by the magnetization reversal of the F2 straight wire. This particular geometry was then used in the design of our LSVs nano-structures, since it gives a quite good contrast of switching fields, and thus a quite stable AP state. Note that defects of the fabricated devices or change in temperature can modify these values. OOMMF simulation corresponds to the case for $T = 0\,K$.

The results of the nanofabrication process are represented in Fig. 2.2(a). One of the ferromagnetic wires is connected at both its ends to a ferromagnetic pad. These pads facilitate the nucleation of the reversed domain, followed by domain-wall propagation within the wire, thus lowering its switching field [86]. The other ferromagnetic wire has a sharp apex in order to increase the contrast in the reversal field of the two F nanowires.

For the experimental evaluation of the switching fields, Anisotropic Magneto-Resistance (AMR) transport measurements were performed on the nano-structures. In this type of measurements, the angle (θ), between the charge current passing through the nanowire and the magnetization direction, is reflected by the variation of the resistivity of the ferromagnetic wire [87]:

$$\rho = \rho_{\perp} + (\rho_{\parallel} - \rho_{\perp}) cos^2\theta \tag{2.3}$$

where $\rho_{\perp}$ and $\rho_{\parallel}$ are the resistivities of the ferromagnetic wire, when the current is perpen-

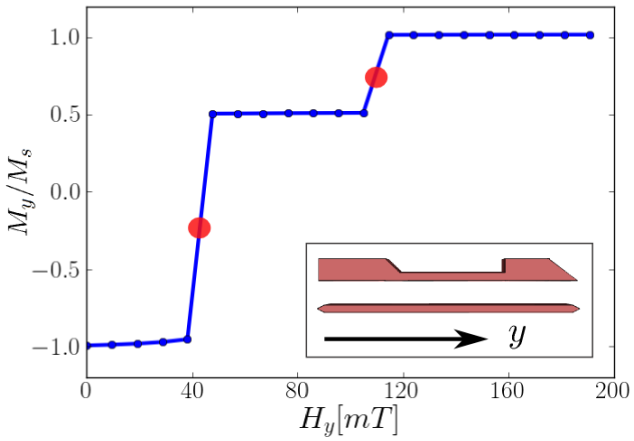

Figure 2.11: *Micro-magnetic simulation by OOMMF of the magnetization curve of the two ferro-magnetic contacts. Two distinguish switching fields (marked by red circles) at* $40\,mT$ *and* $110\,mT$ *correspond to the wire with the reservoir and the straight one, respectively. Figure in the inset represents the sketch of the studied geometry of Py nano-wires. The field is applied along the wire axis (y), with a small in-plane misalignment (2%).*

dicular and parallel to the magnetization respectively.

Figure 2.12 represents the experimental AMR curves for two ferro-magnetic nano-wires. Figure (a) corresponds to F1 (the left ferromagnet) and figure (b) to F2 (the right ferromagnet). Reversal fields of wires with and without reservoirs are found to be $50\,mT$ (a) and $110\,mT$ (b) respectively. These values are in agreement with those from the micro-magnetic simulations for this geometry [cf. *Fig. 2.11*]. Nevertheless, some sample to sample variations exist, but the good contrast always allowed to reach the AP state. In the case of permalloy nano-wires, the saturation field was not reached for the perpendicular direction (out-of plane) of the external magnetic field, because the maximum applied field of the measurement setup is limited to $0.9\,T$. One should note that the saturation field for this material is around $1.2\,T$, which was verified by our later experiments [88].

When characterizing the magnetic properties of presented nano-structures using AMR measurements, an interesting effect appears while working with narrow Py nano-wires (less than $150\,nm$ width). In the parallel direction, we observed a similar behavior as in FePt nanowires of a very high magneto-crystalline anisotropy [cf. *Fig. 2.13*].

When the applied external magnetic field is parallel to the orientation of the magnetization of Py nano-wire, the resistivity decreases linearly with the applied field, whereas, according to AMR theory, it should be constant, since the magnetization orientation stays constant. This effect is ascribed to the Magnon Magneto-Resistance reflecting the magnon contribution to the resistivity of the ferromagnet. The magnon population is characterized by the higher resistance for small magnetic fields than for higher magnetic fields, where the magnon population is reduced, resulting in a smaller resistivity.

An alternative explanation based on the AMR can be disregarded, as it would require an

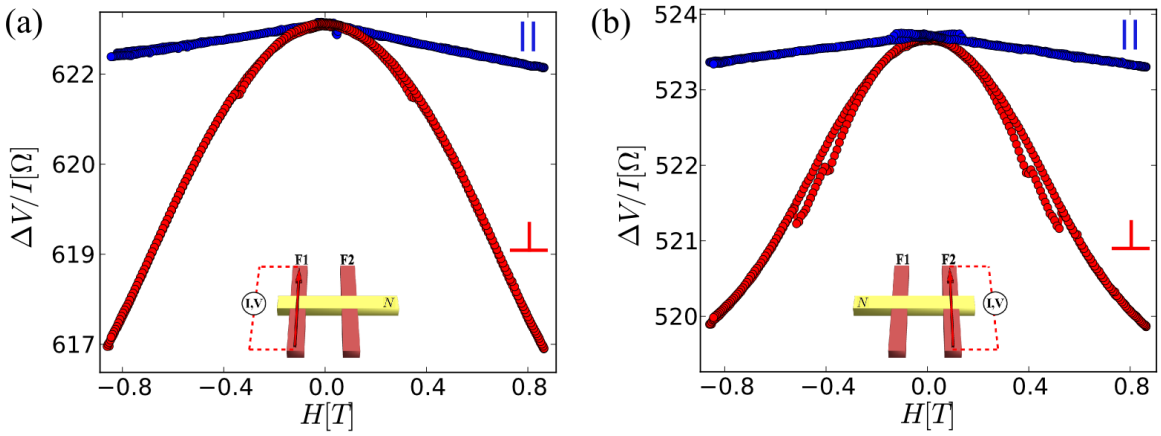

Figure 2.12: *Anisotropic Magneto-Resistance measurements of the two ferromagnetic permalloy nano-wires ((a) with nucleation pad, (b) straight wire), recorded ad* $T = 300\,K$*. Red curve stands for perpendicular and blue curve for parallel to the wire external magnetic field sweep. Inset represents the schematic probes configuration of the lateral spin-valve.*

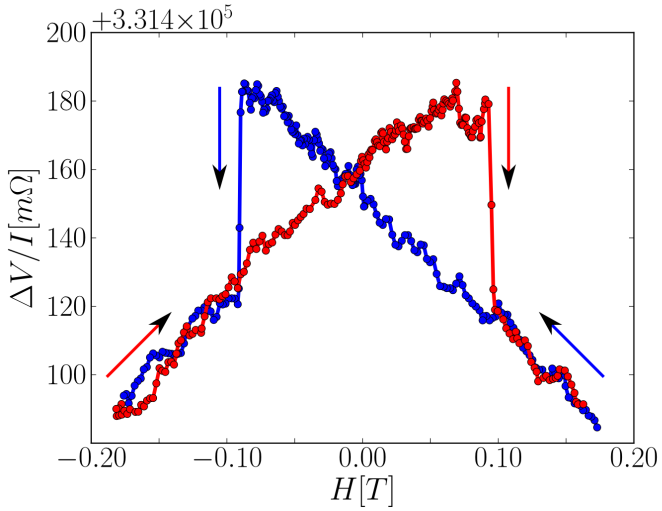

Figure 2.13: *MR measurements of narrow Py nano-wire, recorded at* $300\,K$*. The external magnetic field is swept along the wire direction, evidencing the magnon MR.*

unusual misalignment of almost 20 degrees in order to take into account the change of resistance at $0.9\,T$ [cf. *Fig.2.12*]. Moreover, while reversing the field, the resistance keeps on increasing linearly, up to a sharp decrease of resistivity, due to the abrupt change of magnon density at M reversal. The disappearance of the AMR contribution in narrow Py wires is caused by the enhancement of the shape anisotropy. In those wires, the increased importance of the demagnetization energy keeps the magnetization along the wire axis. Consequently, the AMR contribution vanishes in the parallel field.

Such observation led to several studies of the magnon MR in systems with planar magnetization. We showed that it can give access to the precise position of the domain wall as that was evidenced by pinning a domain wall on constrictions of narrow Py wires [88, 89].

2.5 Conclusions

We developed the multi-angle evaporation technique in high aspect ratio resist openings, for the fabrication of multi-terminal LSVs made of narrow wires, with an accurate control of the switching fields confirmed with both micro-magnetic simulations and experiment.

This approach, based on the commonly used shadow evaporation method, takes advantages of the masking effects of a single resist. The active part of the device can be thus fabricated in one single evaporation sequence, avoiding exposing the interfaces to air during the process targeting, the fabrication of depolarization-free F/N interfaces.

We were able to obtain clear spin signal for nano-devices with different non-magnetic materials, as Al, Cu and Au at room temperature as well as at $T = 77\,K$. The large spin signals we obtained, validate the efficiency of the spin injection and the spin detection in our devices. Our results show that the use of materials with large l_{sf}^{N}, combined with the multi-angle evaporation and a careful optimization of the LSVs geometries, can lead to high spin signals, and are in an excellent agreement with numerical calculations [90, 91] performed by using 1D models.

Chapter 3

Characterization of the spin dependent transport properties in lateral spin-valves

In order to study the spin Hall effect in lateral nano-structures, one needs to characterize the spin-dependent transport in LSVs. Thus the main material parameters, the spin diffusion length (l_{sf}) and the spin polarization (P_F) have to be estimated. For this purpose, the geometry of the nano-structures (width, thickness, gap size) and such parameters as resistivities or interface resistances need to be known. In this chapter, the basic techniques allowing the extraction of these quantities will be described, in order to show the analysis procedures applied for a given sample set. Then the standard 1D model, commonly used for the estimation of l_{sf} and P_{eff}, will be described together with Finite Element Method (FEM) simulations. Both the 1D model calculations and the 3D FEM simulations will be used for the analysis of the spin signal amplitude with the separation of the ferro-magnetic electrodes for Py/Al, Py/Cu and Py/Au sample sets. Also, an extended 1D model, based on the transfer matrix approach, which takes into account the bulk and the interface effects, will be introduced. In this chapter, it will be used to extract the spin-flip probabilities at the sample interfaces.

3.1 Basic characterization techniques

In this paragraph the methods allowing extraction of such parameters as widths, thicknesses, resistivities, and the interface resistances will be discussed. This stage is necessary since the models describing spin dependent transport rely on these parameters.

The quality of the nano-structures has been investigated by means of **Scanning Electron Microscopy** (SEM). This basic characterization technique enables systematical mapping of the device batch (6×11 devices) in order to identify defects and to provide an image support for the characterization process. The most valuable aspect, when using this technique for the device characterization, is a possibility to extract the nano-structures dimensions, in particular, the widths of the nano-wires ($w_{F(N)}$), since they can be different from nominal ones after the nano-

fabrication process. Also, in the case of the nano-structures designed to study the spin Hall effect [cf. *Chapter 6*], the gap between a ferro-magnetic injector and an inserted SHE material also needs to be extracted. This gap can vary since the two nano-wires are made in two separate e-beam lithography steps, involving the realignment of the sample for each one of them.

These geometrical parameters have been extracted for each sample presented in this thesis. For this purpose, different SEM acceleration voltages were used, laying in the range of $3-10\,keV$. For the imaging of surfaces a lower voltage is used (usually around $3\,keV$) to increase the surface contrast. A working distance of $3\,mm$ with the in-lens Secondary-Electrons detector was used, giving the highest resolution of the SEM of $1\,nm$.

For the nano-devices coming from the same batch, basic material parameters are the same as they were submitted to the same nano-fabrication procedure. Therefore, the average values of the width, the resistivity and the interface resistance have been used each time for the analysis. Note that all sample sets were designed in order to allow extraction of every parameter needed in further analysis. This aspect is very important as many of the electric transport properties can change from one sample set to another. Slight nano-fabrication conditions variations (base pressures, widths, thicknesses and quality of the deposit according to crucible and an evaporation chamber condition) can significantly influence the properties. Note that the nominal distance L, separating the two ferro-magnetic electrodes in LSVs, presented in this thesis, is constant and does not change in the nano-fabrication process, since both ferro-magnets are made in the same lithography step.

In the following, methods of evaluation of all parameters needed to perform a complete analysis are presented.

3.1.1 Cross-shaped devices for resistivity measurements

In order to measure the resistivity of the materials used in the LSVs, special cross-shaped nano-structures have been fabricated. For a given set of nano-structures, each time, two cross-shaped structures (for each material) are prepared for resistivity estimations. Figure 3.1 represents a SEM image of a cross nano-structure with wires widths of $200\,nm$, with Al electrodes connecting the nano-structure to larger Au pads.

In order to measure the resistivity of a given material, the Van Der Pauw method is used [92]. The charge current is sent through two neighboring arms of the cross, and the voltage is measured on the opposite arms. This procedure is done for two different probe configurations, called vertical (V) and horizontal (H). Thus two resistance values are obtained: R_H and R_V, by permuting one current probe with one voltage probe. These resistances are extracted from $V(I)$ curves, performed for each configuration in the current range of $1-200\,\mu A$, and represents the mean values of the resistance over several experimental points. The Van Der Pauw equation used in this approach takes the following form:

$$exp(-\pi R_V/R_s) + exp(-\pi R_H/R_s) = 1 \tag{3.1}$$

This equation is then solved in respect to the sheet resistance R_s. The value of the samples

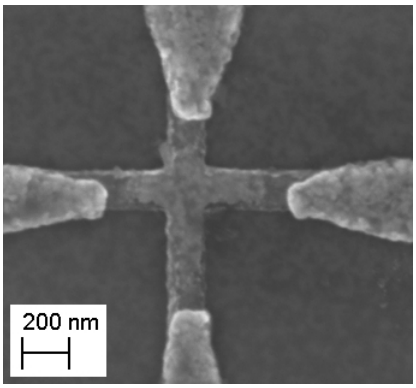

Figure 3.1: *(a) SEM image of a typical nano-structure dedicated to resistivity measurement using the Van der Pauw method.*

resistivity can be further calculated by:

$$\rho = R_s \cdot t_s \tag{3.2}$$

Note that advantage of this technique is that for the extraction of the resistivity of a given material, only the samples thickness t_s is required, without other geometrical parameters. The assumption is that the resistivity is homogeneous in the material of the measurement zone (the cross and its surroundings).

Another method for evaluation of the resistivity of the non-magnetic channel takes advantage of the LSV design. Here, the charge current is injected into the channel, while the two ferro-magnets are used as a voltage probes (4 probe resistance measurements of the channel). When knowing the device geometry one can calculate the non-magnetic channel resistivity. Moreover, similar estimation can be made, when performing GMR measurements. The measured GMR resistance can be expressed as: $R_{GMR} = R_{channel} + 2R_{int}$ (because in GMR measurements the voltage is measured between the two ferro-magnetic wires). One can suppose that the resistance of the channel dominates over the interface resistance (transparent interfaces) contribution and therefore can calculate the resistivity of the non-magnetic material knowing its dimensions.

For a complete geometry characterization a thickness of the nano-structures also need to be evaluated. Since the SEM images do not provide this possibility, another technique was adopted.

3.1.2 Atomic Force Microscope measurements

The Atomic Force Microscopy (AFM) is used for the evaluation of nano-wire thicknesses. This parameter is nominally precisely controlled during evaporation of the materials by means of a quartz micro-balance oscillator, but is affected by the angle deposition. Moreover, after the lift-off process, the re-depositions and left-overs of evaporated materials can strongly influence the spin dependent transport. This can also lead to lower switching fields of the ferro-magnetic electrodes, as the domain wall can be easily nucleated inside these defects. Finally, in the worst case scenario, the nano-structure can be destroyed by the electrical shortcuts formed by the re-deposited materials.

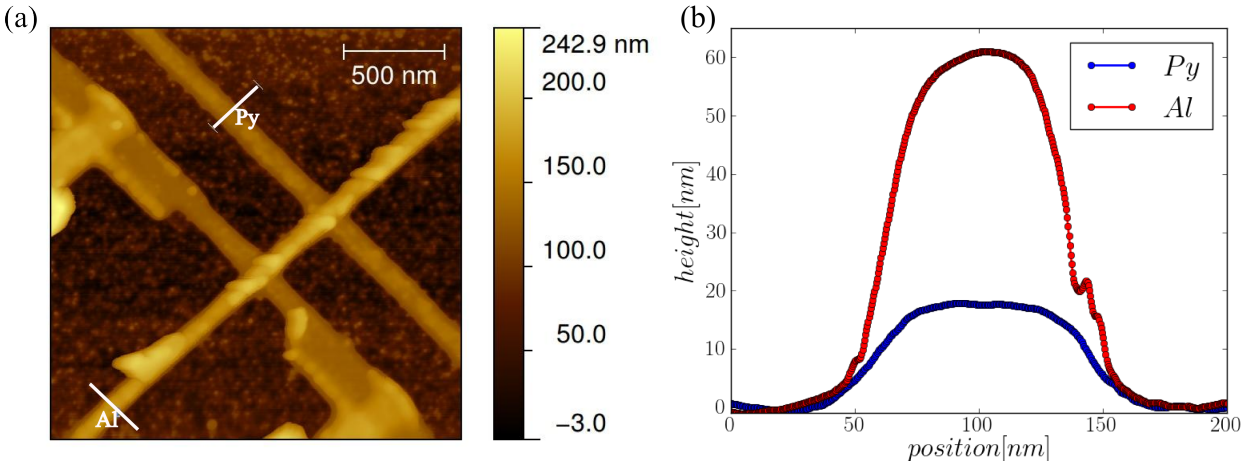

Figure 3.2: *(a) Atomic Force Microscopy image of the nano-device made using the multi-angle evaporation method for Py (15 nm) and Al (60 nm) based structure. The white lines represent places where the estimation of the thickness for both materials was performed. (b) Height profile obtained along the white lines of Fig. (a), providing the mean value of thickness for Py (blue) and Al (red).*

Figure 3.2(a) represents the results of an AFM scan over a typical Py/Al-based nano-structure, made by using the multi-angle evaporation technique. One can notice the re-depositions on the Al channel, nevertheless, it proves a quite good quality of the structure, even made by the lift-off process. Figure 3.2(b) shows the corresponding profiles for Py and Al nano-wires, confirming the good material rate deposition control during the evaporation process (nominal thickness was set-up to $60\,nm$ for the non-magnetic material and to $15\,nm$ for the ferro-magnetic material). Nano-wires profiles have been extracted, on several places on the device, and mean value of height was used for transport analyses. In this case, the values were found to well correspond to $t_{Al} = 60\,nm$ and $t_{Py} = 15\,nm$.

Once all geometrical parameters have been extracted, only the interface resistance still remains unknown.

3.1.3 Interface resistance

Another important parameter can be directly extracted from the experiments. Taking advantages of the four connections to a single F/N interface of the lateral nano-structures, four probe measurements of the interface resistance can be carried out. This resistance is extracted in each nano-structure, for both interfaces, and the mean value, for a given set of sample, is used in theoretical material parameters evaluation.

Figure 3.3(a) represents the interface resistance measurements extracted from four Py/Al based nano-structures from the same batch, where the red line stands for the mean value of $350\,m\Omega$. One can notice that the resistance variations are of the order of $100\,m\Omega$, however, variations of this order does not contribute much to the output spin signal amplitude. Only about 5% signal variation in the Non-Local configuration is noticed in the FEM simulations,

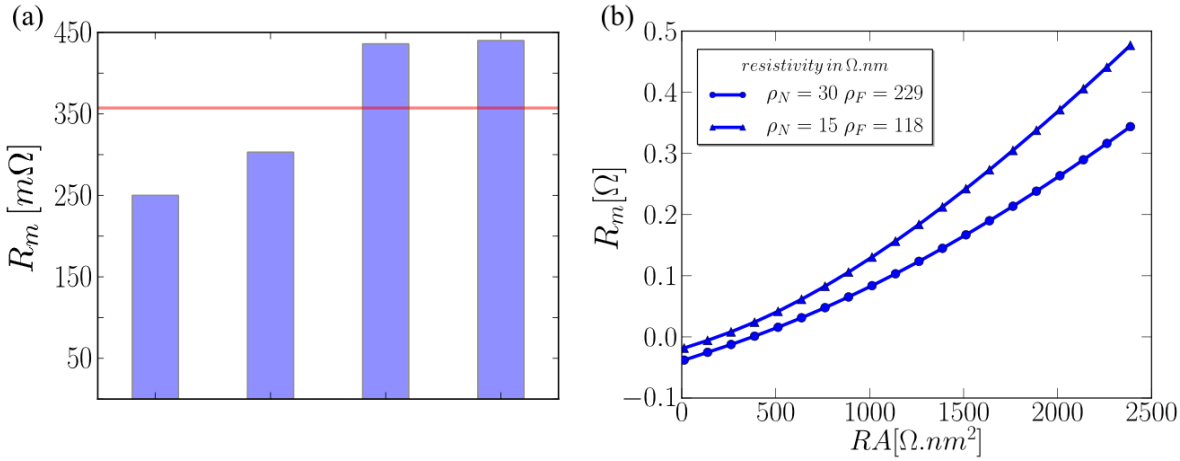

Figure 3.3: *(a) Measured interface resistance using a four probe connection to a single F/N interface for four nano-structures in a given sample set. The red line represents the mean value of the interface resistance. (b) Results of the FEM simulations of the measured resistance R_m as a function of the interface product RA (considering $A = 2500\,nm^2$), for two sets of the experimental parameters (displayed in the label). The measured value of the interface resistance R_m contains also some ohmic loss in F and N.*

when comparing the extreme values.

When performing this type of four probe measurements, the voltage drop within F and N sums up with the interface resistance. In order to extract the pure interface resistance area product (RA) without this additional voltage contribution, FEM simulations have been used. A detailed description of this method can be found in *Appendix A*, whereas here only the basic useful overview will be presented. Taking advantage of a simple cross-geometry, an important aspect of simulation will be pointed out at this stage, which becomes crucial in further 3D model analysis (for more complex geometries).

Figure 3.3(b) represents results of the FEM simulations, for two pairs of resistivity $\rho_{F(N)}$ of a ferromagnetic (F) and non-magnetic material (N), using the geometry represented in figure 3.4(a). The colored arrows express the charge current distribution (represented in a logarithmic scale). The resistivity values, displayed in the legend of figure 3.3(b), correspond to the case of typical resistivities for Py/Al nano-structures at $77\,K$ (triangles) and at $300\,K$ (circles). While changing RA, the corresponding measured resistance can be estimated. The measured resistance values (R_m) of a given sample (either Al, Cu or Au based) are usually found to be in the range of $50 - 400\,m\Omega$. This depends, however, on the technique and on the materials used for the nano-fabrication process (cf. *Chapter 2*). Here, for Py/Al, the mean value of $350\,m\Omega$ was found, what leads to an RA of $2\,f\Omega.m$. This classifies the presented nano-structures in the range of low resistance transparent interfaces (ohmic contacts) and shows the good quality of the interfaces. The RA products for Py/Au, Py/Cu and Py/Al are found usually in the range $1 - 2\,f\Omega.m$. These values are in a good agreement with values estimated from the CPP-GMR heterostructures, grown by sputtering [93, 68], and indicate a good interface quality.

As far as it concerns the FEM simulation, the signal output as a function of total tetrahedrons

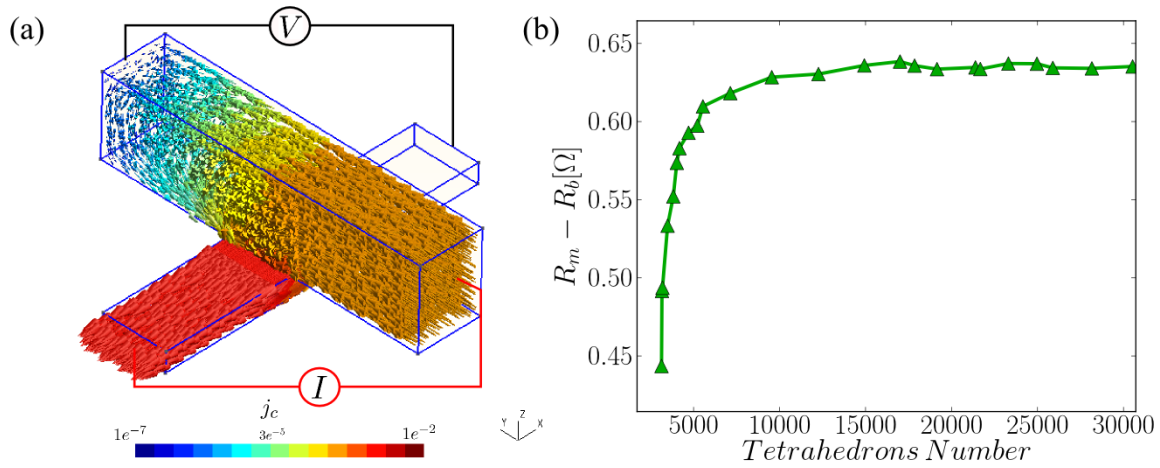

Figure 3.4: *(a) FEM simulation results of cross-shaped geometry in a pseudo four probes configuration for interface resistance simulations. The charge current is injected through two F and N contacts while the voltage is probed on two opposite contacts. The modules of the charge current vectors are displayed in the logarithmic scale. (b) Variation of the signal as a function of mesh density (expressed by the total number of tetrahedrons). The output signal $R_m - R_b$ represents the difference of the resistance calculated in a four probes configuration R_m and the real interface resistance R_b, introduced in the simulation. Note that the result depending on the mesh density for low tetrahedrons number stabilizes, when the meshing is sufficiently refined.*

number, used in order to mesh the given geometry, needs to be studied, since it can significantly change the simulation results. For low mesh densities, the output signal can be even up to 40% higher/lower than for high mesh densities. Figure 3.4(b) shows simulation results for an ohmic voltage drop $R_m - R_b$, between the F and N nano-wires, performed for the cross-shaped geometry represented in figure 3.4(a). The evaluation of the correct mesh density becomes very important as the geometries include right angles. In this case, the density of the mesh should be increased at the proximity of those points in order to reproduce the spin dependent transport with good accuracy. This crucial study of the mesh density will be performed for all FEM geometries presented in this thesis, before the simulations of the transport properties. The tetrahedrons number, which is set-up for a given geometry, corresponds to the situation where the output signal is saturated. When taking the example of figure 3.4(b), the tetrahedron number higher than 20000 is selected, since $R_m - R_b$ does not change significantly in this range, converging to $0.625\,\Omega$. The $R_m - R_b$ difference comes from the additional ohmic losses in the F and N material, in this four probe characterization of the interface.

When knowing all sample's parameters, the analysis of spin dependent transport can be performed. For this purpose, 1D and 3D models will be used for Py/Al, Py/Cu and Py/Au sample sets. A short description of the methods will be given in the following.

3.2 Spin diffusion length and the effective spin polarization evaluation methods

Further, fundamental material parameters for a sample set can be evaluated using methods presented below. This is usually done by fitting the experimental data-points, representing the spin signal amplitudes as a function of the distance separating the two ferro-magnetic electrodes. Two models will be presented and used for the evaluation. The 1D model is commonly used and allows the comparison of the obtained results with the literature. The 3D Finite Element Method will be used, in the same context, as a more accurate method for the extraction of l_{sf} and P_{eff}.

3.2.1 Standard 1D diffusive models

Two 1D models can be found in the literature for the non-local spin transport in metallic lateral spin-valves with transparent (ohmic) interfaces. Both are based on 1D wire-circuit device approximation, in which the propagation of the electro-chemical potential $\mu_{\uparrow(\downarrow)}$ and the spin polarized current $j_{\uparrow(\downarrow)}$ is described by the standard Valet-Fert model [13]. The first of the above-mentioned models was given by Jedema *et al.* [50] and is based on the following assumptions:

(1) l_{sf}^F, $l_{sf}^N \gg w_F$, w_N - the spin diffusion lengths of both ferromagnetic and non-magnetic wires are much larger than the width of those wires.

(2) The cross-sectional area of all the wires are the same in the device.

In the case of ferromagnet with short l_{sf}^F, like permalloy (case of this thesis), the first assumption is not fulfilled, since $l_{sf}^{Py} \sim 5\,nm$, compared to the wire width of $w_{F(N)} = 50\,nm$. Moreover, for commonly used geometries of metallic nano-structures found in the literature, the second assumption does not hold neither.

These limitations were partially overcome in the second model given by Takahashi and Maekawa [14], in which they assumed that:

(1) $l_{sf}^F \ll w_F$, $w_N \ll l_{sf}^N$ - the l_{sf}^F of the ferromagnet is much smaller that the wires widths, and the l_{sf}^N of non-magnetic metal is larger than the widths.

(2) The current at the ferromagnetic/non-magnetic F/N interface is homogeneous.

The first assumption of this model is still valid for the geometry of the nano-structures presented in this thesis. However, the second one is not correct for the case of ohmic (transparent) junctions, where non-homogeneous current distribution can be present at the interfaces, but holds for tunnel barriers. In the nano-devices presented in this thesis, the width of the nano-wires is small, what allows to use this model with a good approximation.

In the general case of a metallic lateral spin-valve with two ferromagnetic electrodes, separated by the distance L and connected by a non-magnetic channel, the non-local spin signal amplitude ΔR_s, based on a one-dimensional spin diffusion model, is given by the general equation [14, 71, 13]:

$$\Delta R_s^{Takahashi} = \frac{R_N(P_F\frac{R_F^*}{R_N} + P_{int}\frac{R_{int}}{R_N})^2 exp(-L/l_{sf}^N)}{(1+2\frac{R_{int}}{R_N}+2\frac{R_F^*}{R_N})^2 - exp(-2L/l_{sf}^N)} \tag{3.3}$$

where P_F and P_{int} are the bulk and the interface spin polarizations of the ferromagnet, R_{int} stands for the interface resistance and $R_{N(F)}^{(*)} = \rho_{N(F)}^{(*)} l_{N(F)}/A_{N(F)}$ stands for the non-magnet/(ferromagnet) spin resistances, with: $A_N = w_N \times t_N$, $A_F = w_F \times w_N$ (this assumption holds for the case of short l_{sf}^F in the ferromagnet, e.g. case of Py). Here $\rho_{N(F)}^{(*)}$ ($\rho_F^* = \frac{\rho_F}{(1-P_F^2)}$), $l_{sf}^{N(F)}$, t_N, $w_{N(F)}$, $A_{N(F)}$ are the resistivity, the spin diffusion length in the normal material N (in the ferromagnetic material F), the thickness, the width and the cross sectional area of the ferro (F) or non-magnetic (N) material respectively.

When limiting this model to the case of transparent interfaces (neglecting the interface resistance R_{int}), it can be rewritten in the simpler form:

$$\Delta R_s \backsimeq \frac{2P_{eff}^2}{(1-P_{eff}^2)^2}\frac{R_F^2}{R_N + 2R_F/(1-P_{eff}^2)}[sinh(\zeta + \frac{L}{l_{sf}^N})]^{-1} \tag{3.4}$$

with $sinh(\zeta) = \frac{2R_F^*}{R_N}\frac{1+R_F^*/R_N}{1+2R_F^*/R_N}$ corresponding to $\zeta \approx 2R_F^*/R_N$, in the limit where $R_F^* \ll R_N$ and $R_F^* = R_F/(1-P_{eff}^2)$ [69].

Note that in this approach the bulk polarization P_F is expressed as P_{eff}. It has a smaller value than the bulk value of the ferro-magnetic electrodes, reflecting the spin depolarization at the interfaces by spin-flip, which has not been taken explicitly into account in the model.

This model will be used in the following analysis of the experimental data, allowing the extraction of the spin diffusion length l_{sf}^N and of the effective spin polarization P_{eff}. Since this model gives a range of possible solutions in data fitting, and discrepancies in 1D approach can exist, the same analysis will be also performed by the 3D method presented bellow.

3.2.2 Finite Element Method simulations - 3D model

Finite Element Method simulations have been carried out for the used geometries for extraction of l_{sf}^N and P_{eff}. In these simulations, the distribution of the charge current, the spin current and the spin current accumulation was calculated for two magnetic system configurations (either parallel P or anti-parallel AP). The spin signal amplitude is reproduced by taking the difference of the output signals for the two states. In each case, the spin signal was evaluated from the difference of electro-chemical potentials integrated on the end surface of the voltage contacts (cf. *Fig.3.5*). The contact wires have to be long enough (several l_{sf}) to cancel spin accumulation, so both up and down electro-chemical potentials are equal to the pure electric potential. This corresponds to the Non-Local probe configuration setup detection, where the voltage is probed between the right side of the non-magnetic channel and the lower part of the ferromagnetic wire. Note that the extraction of the potentials is made far from the F2/N interface.

The FEM simulations are based on a simple diffusion equation, similar to the 1D model. The charge current conservation principle is imposed, as well as the spin relaxation through l_{sf}, and the potential distribution in desired geometry is calculated (more detailed description can

be found in *Appendix A*). The charge current is injected in the left side of the device through the ferro-magnetic wire and passes the F1/N interface. It is then drained out on the left side of N. This situation is represented in figure 3.5(a) where the charge current j_q is displayed using colored arrows (modulus in the logarithmic scale). Thus the created spin accumulation diffuses in the non-magnetic channel, creating the spin currents j_s. The spin current distribution is represented for the case of the AP magnetic state in figure 3.5(b), using the logarithmic color scale.

The resulting spin accumulation distribution $\mu_a = \mu_\uparrow - \mu_\downarrow$ for the AP magnetic state is represented in figure 3.6(a-b), using the iso-surface representation (in logarithmic scale). Note that two cases have to be considered depending on the experimental data-points coming either from the multi-angle or from the multi-level nano-fabrication method. Figure 3.6(a) stands for the case where the charge current is injected into N through the top surface of the ferro-magnetic electrode F1. This corresponds to the case of the multi-level nano-fabrication method, where only the top surface is cleaned before the deposition of the non-magnetic channel, and the sides of F1 are not supposed to contribute to the current injection. Figure 3.6(b) represents the case corresponding to the multi-angle nanofabrication method where the active part of the device is evaporated in a single step, without breaking a vacuum, and therefore all surfaces of contact between F and N need to be taken into account in the current injection process analysis.

For all used geometries presented in this thesis, the studies of the output signal as a function of mesh density were carried out.

After a short description of used 1D and 3D models, their application for material parameters extraction will be presented in the following for Py/Al, Py/Cu and Py/Au sample's data sets.

3.3 Analysis of the experimental data

In order to characterize the spin dependent transport by extracting l_{sf}^N and P_{eff} , LSV nano-structures with different separation L of the ferro-magnetic electrodes were fabricated. The spin signal amplitude has been measured as a function of the distance L for samples with Al, Cu and Au non-magnetic channels, at both temperatures, $300\,K$ and $77\,K$. These samples were fabricated using the multi-angle (Al and Au) evaporation method or the multi-level method (Cu) [cf. *Chapter 2*]. The SEM image of a typical nano-device made by using the multi-angle method is presented in figure 3.7(a), in which the red line indicates the varied distance L. The SEM image of a typical nano-device made by using the multi-level method, is presented in figure 2.2(b) [cf. *Chapter 2*].

3.3.1 1D model

First, the experimental data have been fitted using equation 3.4, which is considered as a simple model since it is based on a simple 1D resistor model approximation, and does not take into account the current distribution at the F/N interface or in the non-magnetic channel [74]. By using this model, l_{sf}^N and the effective spin polarization P_{eff} have been estimated for a given

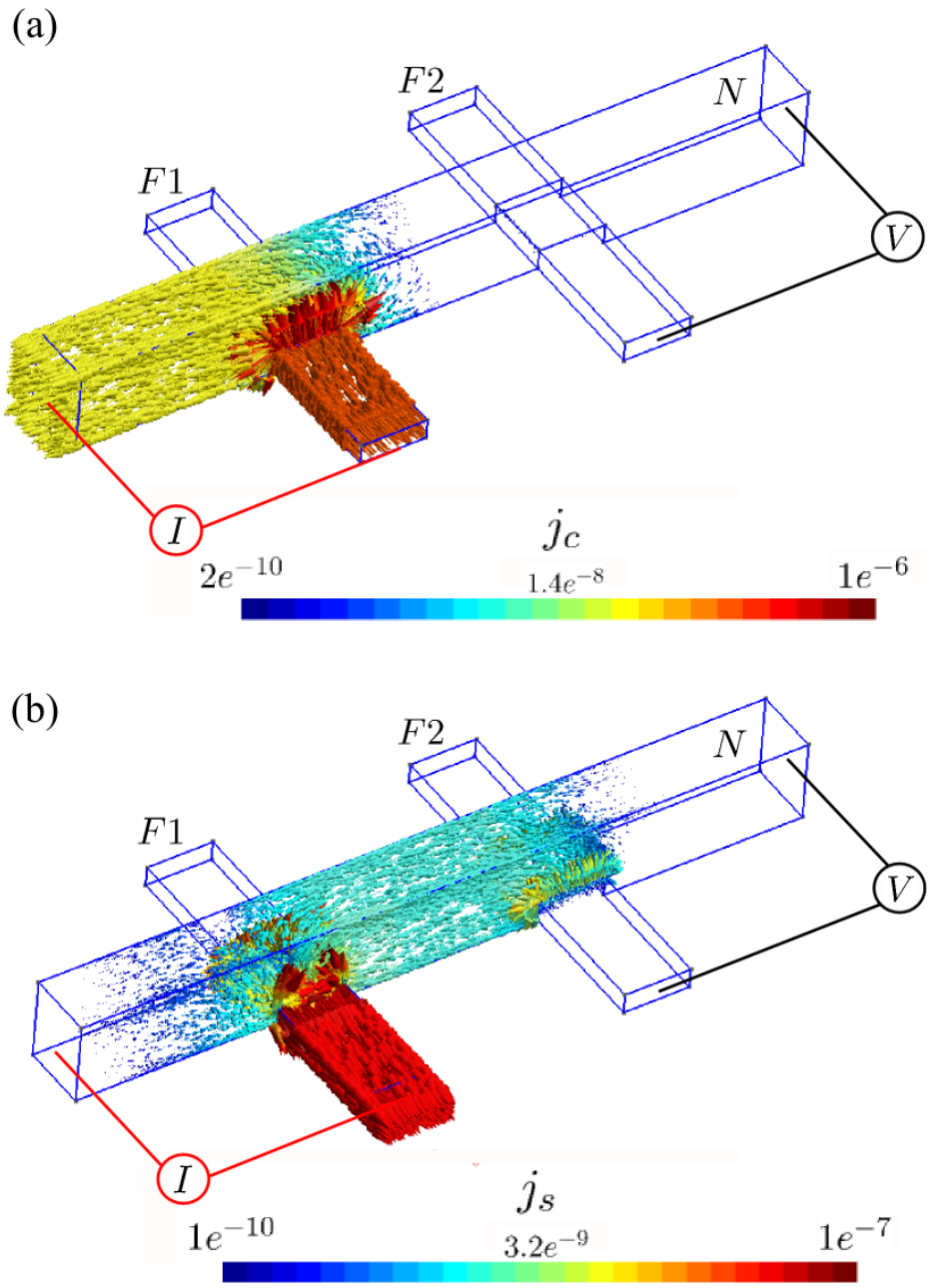

Figure 3.5: *FEM simulations results for a given geometry of the nano-structure with (a) charge current j_q injected at the bottom of the ferro-magnetic electrode F1 (bottom part) and drained out through the left side of a non-magnetic material, and (b) spin current j_s, with the efficient absorption of F2, reflecting the situation with $R_F < R_N$. Both j_c and j_s are displayed in the logarithmic scale.*

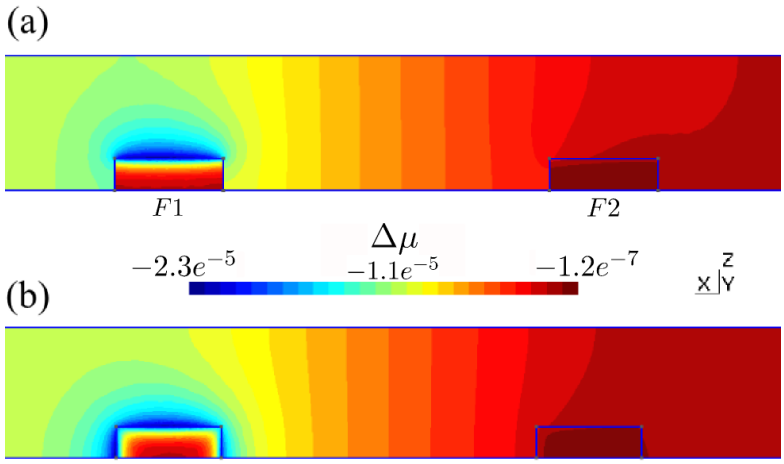

Figure 3.6: *FEM simulations results of the spin accumulation distribution* $\mu_a = \mu_\uparrow - \mu_\downarrow$ *in a LSV, displayed by using the iso-surfaces representation (logarithmic scale) on the longitudinal cut at the center of N. The charge current is injected on the left side of the ferro-magnetic material (F1) while the difference of the spin accumulation (for a given magnetic state of the system that can be parallel or anti-parallel) is measured between F2 and the right side of N. Figures represent the situations where (a) only top F1 surface and (b) top surface and both side surfaces of F1 contribute to the current injection, what corresponds to the case of the LSV, fabricated by using different methods (the multi-level and the multi-angle).*

set of nano-structures. Data fitting was done by using optimization algorithms of the least-square method, where one minimizes the sum of squares of given function residuals [94, 95]. Additionally Levenberg-Marquardt and the genetic algorithm methods were also used for these evaluations. Error values have been estimated using χ^2 distribution based on the standard deviations calculated from the covariance matrix.

Table 3.1 shows the fitting results summary for three sample sets, after extraction of the parameters from this model.

material	P_{eff}	$l_{sf}^N\,[nm]$	$T\,[K]$
Py/Al	0.18 ± 0.01	450 ± 42	300
	0.33 ± 0.01	850 ± 183	77
Py/Cu	0.26 ± 0.04	290 ± 42	300
	0.40 ± 0.01	750 ± 77	77
Py/Au	0.37 ± 0.05	100 ± 16	77

Table 3.1: *Representation of the fit results (for a given temperature) obtained by using equation 3.4 for Py/Al, Py/Cu and Py/Au LSV sample's data-sets.*

3.3.2 3D simulations

The 3D simulations have also been used for material characteristic parameters evaluation. Note that it represents the ideal case of a lateral nano-structure, where there are no defects in the sample, no spin loss at the interface, nor other not mentioned scattering centers, and the interface

is homogeneous. As it will be pointed out later in this chapter, this model will be further extended to a more realistic case, by introducing the spin dependent interface resistance parameters. Nevertheless, in these analyses, in order to remain consistent with the presented 1D model, this aspect will be omitted.

The l_{sf}^{N} and the P_{eff} obtained from this method are very similar to the 1D model. Table 3.2 summarizes 3D model fitting results for Py/Al, Py/Cu and Py/Au nano-structures. For all samples only very-slightly lower values of l_{sf}^{N} and P_{eff} were found compared to the 1D model, independently on the temperature. This validates the 3D simulations and confirms the 1D approximation.

material	P_{eff}	$l_{sf}^{N}\,[nm]$	$T\,[K]$
Py/Al	0.15	450	300
	0.31	750	77
Py/Cu	0.22	290	300
	0.38	770	77
Py/Au	0.36	110	77

Table 3.2: *FEM simulations estimation of the l_{sf}^{N} and P_{eff} allowing to reproduce the experimental data-points.*

3.3.3 Fitting results discussion

Figure 3.7(b) shows the variation of the amplitude of the spin signal as a function of the distance L. The experimental data-points for Py/Al nano-structures are represented by blue and red dots for $77\,K$ and $300\,K$ respectively, where the dashed curves display the fit results using equation 3.4. The FEM simulations results are represented by green triangles in figure 3.7(b).

The spin diffusion length is significantly increased when going to low temperatures, since the spin-flip mechanism (described in *Chapter 1, section 1.1.2.1*) on phonons becomes less important. The spin-polarized electrons in N are diffusing to longer distances until their spin orientation gets randomized. The effective spin polarization is, in the case of low temperature, increased, since less spin scattering occurs at the interface between Py and Al, and therefore more spin-polarized current can be injected from the ferromagnetic metal into the non-magnetic channel.

Figure 3.8(a) represents the experimental data-points of the spin signal amplitude as a function of L, extracted from Py/Cu LSV nano-structures for $300\,K$ and $77\,K$. The dashed curves represent the 1D fit results by using equation 3.4, and the green triangles stand for the 3D model fits. Note that this data-set comes from the multi-level nano-fabrication method.

When comparing Cu with Al channel, one can notice a higher effective spin polarization for Cu at both temperatures. This means that in case with Cu the current injected into the non-magnetic material is more spin-polarized than the current in the case with Al. This can be explained by a higher spin asymmetry γ at the interface for Py/Cu than for Py/Al; for Al, $\gamma_{Py/Al} = 0.025$ and for Cu it is found to be as high as $\gamma_{Py/Cu} = 0.7$, which is not far from the bulk polarization of Py ferro-magnetic electrodes ($P_{bulk}^{Py} = 0.77$) [96, 97, 98]. This aspect will be investigated in details in the next paragraph, where the spin transfer matrix application for

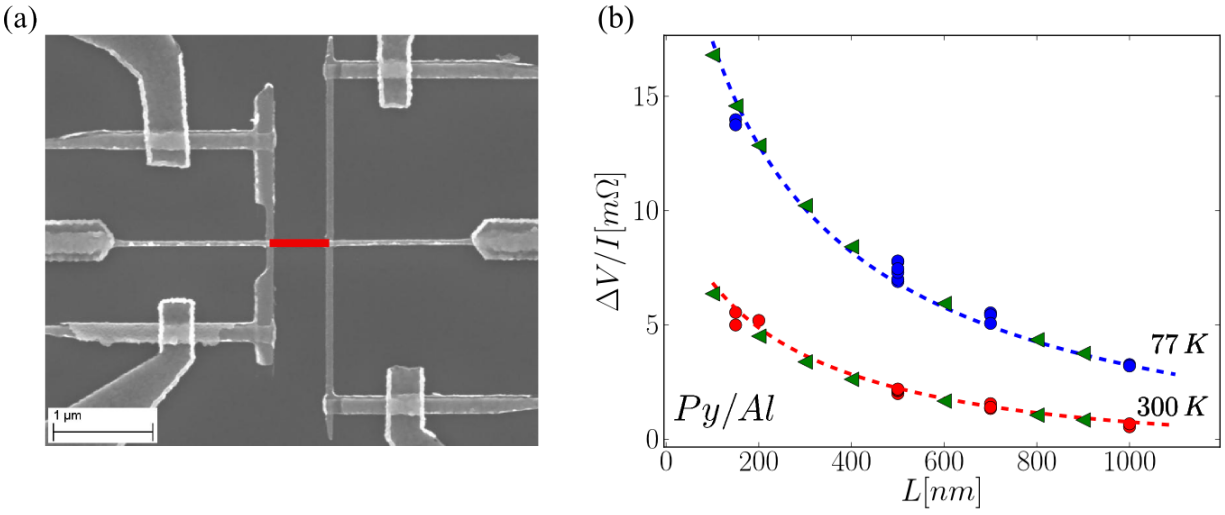

Figure 3.7: *(a) The SEM image of the nano-device made by using the multi-angle method, with the distance L separating two Py ferro-magnetic electrodes (marked by a red line) connected with a non-magnetic Al channel; (b) Experimental data-points for a given set of the Py/Al samples for* 300 *K (red dots) and* 77 *K (blue dots). Dashed curves represent results of the 1D model fit using equation 3.4. Green triangles represent the FEM simulations results.*

extraction of the spin-flip probability at the interfaces will be presented.

An interesting fact to be noticed is that the various band-structure anomalies (so-called spin hot spots), such as crossings of the Brillouin zone boundaries and accidental degeneracy points on the Fermi surface, can increase the spin-orbit interaction by several orders of magnitudes, strongly enhancing spin relaxation in polyvalent metals (Al, Pd, Be, Mg), as compared to the simple estimates [99, 100]. Also, the spin relaxation for Al strongly depends on the magnetic field (B), at low temperatures. The spin resonance measurements show that at temperatures below 100K, $1/\tau_{sf}$ increases linearly with increasing B [101]. It has been suggested that the observed behavior is due to the cyclotron motion through spin hot spots [102].

As for the l_{sf}^N of Cu and Al, at the room temperature, one can find a longer spin diffusion length for Al than for Cu , contrary to the low temperature where the l_{sf} of Cu is longer than the l_{sf} of Al. The main differences for presented sets of samples come from the resistivity variations, which strongly influence the spin diffusion length. These differences depend also on the thickness of the used non-magnetic channel, especially for the Cu based samples [103], what can explain a longer l_{sf}^N of Cu than the l_{sf} of Al, at low temperature. The typical values of the residual ratio resistivities ($\rho^{300\,K}/\rho^{77\,K}$) for Al, Cu and Au are 2.3, 1.7 and 1.3 respectively (considering resistivities presented in *Chapter 2*). Despite a smaller residual ratio resistivities, l_{sf}^N in Cu is much more increased compared to Al, while going to low temperature.

Note that the amplitudes of the spin signals for Py/Al, Py/Cu and Py/Au nano-structures (presented in *Chapter 2*) suggested that Al has the longest l_{sf}^N followed by Cu and Au. However, since the resistivity of Al and Cu evolved to higher values during this thesis, the l_{sf}^N length and the effectiveness of spin injection were also significantly reduced. In the case of Al, for the first sample sets, resistivity was estimated to be $15\,\Omega.nm$, whereas for succeeding sample sets this

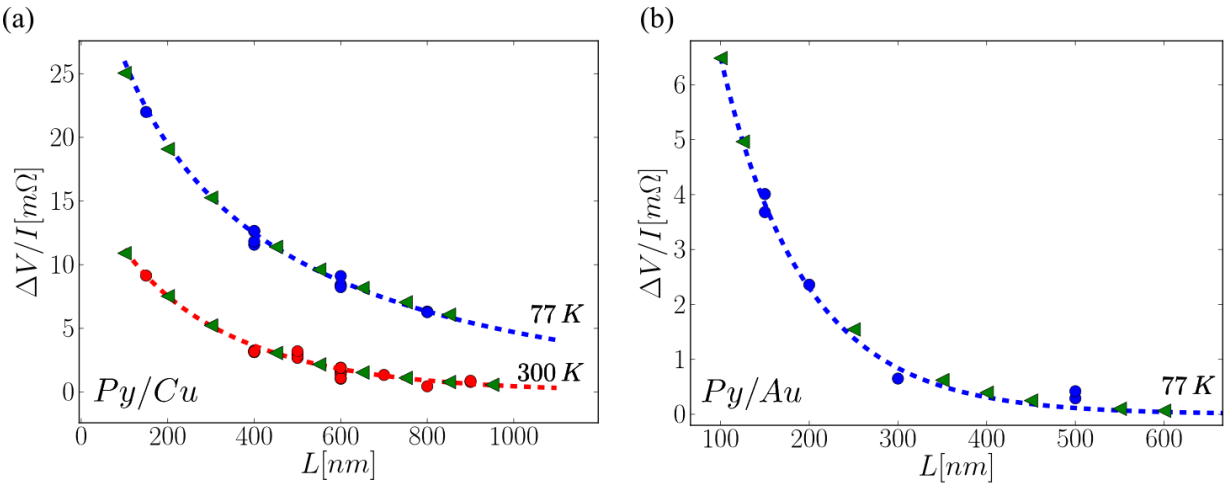

Figure 3.8: *Experimental data-points as a function of distance L for* 300 *K (red dots) and* 77 *K (blue dots), altogether with the fit results using the 1D model described by the equation 3.4 (dashed curves) and the FEM simulations results (green triangles) for (a) Py/Cu and (b) Py/Au based nano-structures.*

value increased up to $30\,\Omega.nm$. Thus the amplitude of the spin signal decreases by the factor of two, when considering this case by using equation 3.4. For Cu, usual resistivity values are found to be $25\,\Omega.nm$ at $77\,K$ and $35\,\Omega.nm$ at $300\,K$.

Figure 3.8(b) represents the experimental data and the fit results using 1D and 3D models, for Py/Au nano-structures fabricated using the multi-angle method. The data-points were recorded only at $77\,K$, since a not sufficient measurement resolution was available at the time, and the amplitude of the spin signal at $300\,K$ was too small to be detected. In this case, the two models are in an excellent agreement for both evaluated parameters. Note that for the nano-structures with Au channel, the effective spin polarization is the highest, compared to Al and Cu. The high spin injection rate for this material contrasts with low l_{sf}^{N}, compared to Al and Cu. This low spin diffusion distance, in the case of Au, can be explained by a strong spin-orbit interaction.

3.3.4 Summary of the fits results

The summary of the fit results obtained on a given sample sets of LSV nano-structures, with Py ferro-magnetic electrodes and Al, Cu, Au non-magnetic channels, is presented in the table 3.3. These results are in a good agreement with what can be found in the literature for similar nano-structures [cf. *Table 3.4*]. Finally, 3D and 1D models give very similar results for such experiments, validating the 1D assumption, despite the non-homogeneous current injection.

material	*model*	P_{eff}	$l_{sf}^{N}\,[nm]$	$T\,[K]$
Py/Al	$1D$	0.18 ± 0.01	450 ± 42	300
	$3D$	0.15	450	
	$1D$	0.33 ± 0.01	850 ± 183	77
	$3D$	0.31	750	
Py/Cu	$1D$	0.26 ± 0.04	290 ± 42	300
	$3D$	0.22	290	
	$1D$	0.40 ± 0.01	750 ± 77	77
	$3D$	0.38	770	
Py/Au	$1D$	0.37 ± 0.05	100 ± 16	77
	$3D$	0.36	110	

Table 3.3: *Summary of the fit results from 1D and 3D models, for Py/Al, Py/Cu and Py/Au sample sets.*

With regards to Al and Cu, similar results were found compared to leading groups in this field, which is not the case of Au, where a higher effective spin polarization and a longer spin diffusion length were found. Nevertheless, the narrowing of our wire widths led to much higher spin signal amplitudes.

device	$T\,[K]$	$l_{sf}^{N}\,[nm]$	$P_{eff}(\%)$	*ref.*
Py/Au	10	63 ± 15	3	[45]
	15	168	26	[104]
Py/Al	4.2	1200 ± 200	3	[48]
	293	600 ± 50	3	
Py/Cu	4.2	1000 ± 200	2	[48]
	293	300 ± 50	2	
	300	500	25	[105]

Table 3.4: *Example of the fit results for the similar LSV nano-structures extracted from the literature.*

One can also perform an analysis taking into account bulk and interface effects. For this purpose, the transfer matrix model will be shortly described and then used for extraction of the probability of spin-flip at the F/N interface and the spin diffusion length.

3.4 Transfer matrix method

In this model the interface is treated as an infinitively thin layer. One can attribute parameters describing this layer: the interface spin resistance R_b^*, the spin asymmetry parameter at the interface γ and the spin-flip parameter δ.

Figure 3.9 represents the electro-chemical potentials landscape at the F/I/N interface. The majority spin population is represented by the blue and the minority by red curves, while the average electro-chemical potential is represented by the green curves. Note that the discontinuity of the electro-chemical potentials occurs at the interface and can be described by $\Delta\mu_{\uparrow(\downarrow)} = 2eR_b^*(1 \pm \gamma)J_{\uparrow(\downarrow)}$ [13].

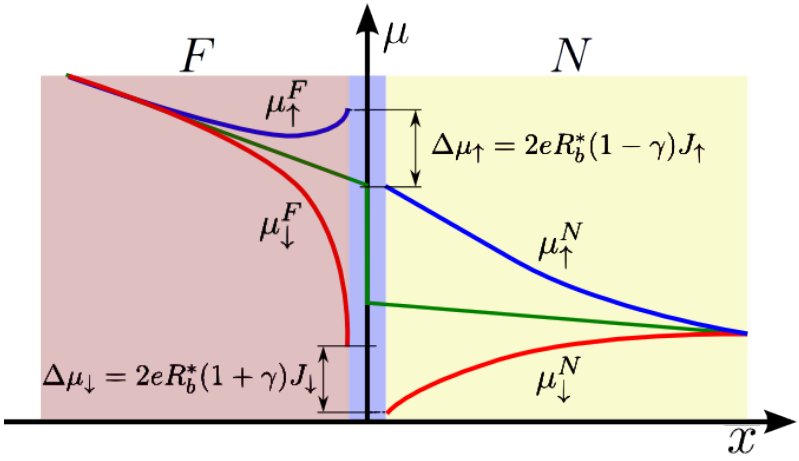

Figure 3.9: *Schematic representation of the electro-chemical potentials landscape, at the vicinity of the $F_{(red)}/I_{(blue)}/N_{(yellow)}$ interface. Blue curves represent the spin-up and red curves the spin-down population, described by the potentials $\mu_\downarrow^{F(N)}$ and $\mu_\uparrow^{F(N)}$. The green line stands for the average electro-chemical potential.*

In this model the spin-dependent current density ($J_{\uparrow,\downarrow}$) for a given spin population ($\mu_{\uparrow,\downarrow}^i$) in the i-th layer (F, N) can be expressed as follows:

$$J_{\uparrow,\downarrow} = (1 \pm \beta_i)\frac{J}{2} \mp \frac{1}{2eR_i^*}[\mu_\uparrow^i exp(x/l_{sf}^i) - \mu_\downarrow^i exp(-x/l_{sf}^i)] \tag{3.5}$$

where the spin polarization is given by $P = \frac{J_\uparrow - J_\downarrow}{J} = \frac{\beta R_F^* + \gamma R_b^*}{R_F^* + R_N + R_b^*}$, following notation from Valet-Fert [13]. Here, $\mu_\uparrow^i$, $\mu_\downarrow^i$ are the amplitudes of the electro-chemical potentials for spin up or down populations and μ_i is the asymptotic electro-chemical potential, equivalent to the weighted average value of electro-chemical potentials (it is actually a supplementary potential constant needed to match the boundary conditions) [106].

In the frame of the transfer matrix technique, we define the spin accumulation vectors for the input and output of the analyzed system, as follows:

$$\nu_{in(out)} = \frac{1}{JeR_{in(out)}}[1, \mu_\uparrow^{in(out)}, \mu_\downarrow^{in(out)}, \mu_{in(out)}^0] \tag{3.6}$$

In this approach, the matrix M describes all processes occurring when passing through the system. It can be represented in the form $M = (\Pi[I^{i/i+1} \times \pi_i] \times I^{1/0})$, where the matrix π_i propagates the spin accumulation vector from the left to the right interface, in the material i, and $I^{i/i+1}$ is a matrix describing the $i/i+1$ interface. One can thus write:

$$\nu_{out} = M \times \nu_{in} \tag{3.7}$$

In the case of the lateral spin-valve devices the spin signal can be described, as demonstrated by Jaffres *et al.* [82], in the following form:

$$\Delta R = R_N \frac{M_{42}^2 exp(-\frac{L}{l_{sf}^N})}{M_{22}^2 - M_{32}^2 exp(-\frac{2L}{l_{sf}^N})} \tag{3.8}$$

Where $M_{22,32,42}$ are the M matrix coefficients depending on the system geometry. When introducing the transfer matrix coefficient for LSV presented in this thesis, as calculated in [82], and taking into account the spin memory loss at the interface as in the analysis of Bass and Pratt [93], one obtains:

M_{22}	M_{32}	M_{42}
$[(\frac{1}{2} + \frac{R_F^*}{R_N})cosh(\delta) + (\frac{R_b^*}{\delta R_N} + \frac{1}{2}\frac{\delta R_F^*}{R_b^*})sinh(\delta)]$	$(P_F R_F^* + \gamma R_b^*)$	$\frac{1}{2}$

Note that in an ultra-thin layer of thickness t_{int}, an interface resistivity $\rho_{intr}^* = R_{int}^*/t_{int}$, an asymmetry coefficient γ and a spin diffusion length equal to $l_{sf}^{int} = \frac{t_{int}}{\delta}$, have been introduced. Here, δ is the spin-flip parameter, related to the probability of the spin-flip at the interface $P_{spin\,flip} = 1 - exp(-\delta)$.

Thus equation 3.8 can be expressed in the following form:

$$\Delta R = \frac{(P_F R_F^* + \gamma R_b^*)^2}{R_N\{[(\frac{1}{2} + \frac{R_F^*}{R_N})cosh(\delta) + (\frac{R_b^*}{\delta R_N} + \frac{1}{2}\frac{\delta R_F^*}{R_b^*})sinh(\delta)]^2 exp(\frac{L}{l_{sf}^N}) - \frac{1}{4}exp(-\frac{2L}{l_{sf}^N})\}} \tag{3.9}$$

On can use this model to analyze the experimental data by fitting with four free parameters l_{sf}^N, δ, γ, R_b^*. However, this would give many possible solutions, as all values are highly correlated. Therefore, γ will be taken from the literature, and R_b^* will be replaced by the mean interface resistance extracted from the experiments.

3.4.1 Experimental data fitting using the transfer matrix method

When making an analysis using the transfer matrix method, that takes into account interface and bulk effect, one can find different values of l_{sf}^N than when using 1D and 3D models. The differences between the transfer matrix method and the 1D model (*Equation 3.4*) may come from the 1D model sensibility to the free parameters variation, especially for small gaps. Therefore, any small variation, like the reproducibility problems of the spin signal amplitude, can significantly change extracted values of l_{sf}^N and P_{eff}. When using equation 3.9, in the case of small gaps it does not converge so fast, however, lower values of l_{sf}^N need to be used in order to reproduce the experimental data. The slight differences from the 3D model come mainly from the introduction of the spin dependent interface effects in the transfer matrix. Note that similar values could be obtained with the FEM by introducing a similar system description taking into account interface effects. This approach will be used in the FEM analysis presented in *Chapter 6*.

material	δ	$l_{sf}^{N}\,[nm]$	$R_b\,[\Omega]$	$P_{sf}\,[\%]$	$T\,[K]$
Py/Al	1.29	395	0.21	73	300
	0.93	590	0.20	61	77
Py/Cu	1.28	290	0.24	72	300
	1.04	560	0.20	65	77
Py/Au	1.15	100	0.20	68	77

Table 3.5: *The spin asymmetry for Py/Al and Py/Cu was taken to be* $\gamma_{Py/Al} = 0.025$ *and* $\gamma_{Py/Cu} = 0.7$ *[96, 97, 98]. For Py/Au interface* $\gamma_{Py/Au}$ *was supposed to be similar to Py/Cu.*

In the presented analysis, the interface asymmetry parameter γ was taken from the literature for Py/Al ($\gamma_{Py/Al} = 0.025$) and Py/Cu ($\gamma_{Py/Cu} = 0.7$) interfaces [97, 96, 107]. These parameters are given for the temperature of $4.2\,K$, however, here they are used independently on the temperature, and are supposed to be constant. One can suppose that the variations of γ, while keeping it constant, will be reflected through other free parameters.

Table 3.5 shows a summary of results obtained using the transfer matrix method where the spin-flip effects at the interfaces are taken into account. Smaller values of the l_{sf}^{N} are found compared to 1D and FEM analysis results, for all Py/Al, Py/Cu and Py/Au samples. Moreover, the spin-flip probability is of the order of P_{sf} (60%), which explains that P_{eff} in 1D model is estimated to be half of the bulk value (0.77). An important fact to be noticed is that the nano-fabricated Py/Cu samples were not protected by a capping layer. Thus transport in Cu based nano-device could be strongly affected by oxidation. This could also lead to lower spin diffusion length in this material, compared to the values reported in the literature.

Concerning the spin-flip probability P_{sf} at the interface, the analysis for all presented materials at low temperatures reveals its decreased value compared to the room temperatures, what can explain a decrease of the spin-flip process and thus higher spin signal amplitudes. At low temperatures, the highest spin-flip probability is found for Py/Au, then medium for Py/Cu and the lowest one for Py/Al. Note that in the case of Py/Au nano-structures, since $\gamma_{Py/Au}$ cannot be found in the literature, a similar value was used in the analysis as for the case of Py/Cu interface. One would expect that in regards to a higher spin-orbit interaction in Au, Py/Au would have a higher spin-flip probability at the interface than Py/Al. Moreover, for Py/Cu sample sets the interface cleaning is needed before the deposition of the non-magnetic channel, and therefore, comparing with the multi-angle nano-fabrication method, one should also expect a higher depolarization occurring at the interfaces. One shall note that in the analysis, an increase in the value of P_{eff} is counterbalanced by a lower value of l_{sf}^{N}.

3.5 Conclusions

In conclusion, for characterization of the spin dependent transport in LSVs, the nano-structures with different separation of the ferro-magnetic electrodes, going down to $100\,nm$, were fabricated. This was made using both the multi-angle and multi-level methods. By means of standard characterization techniques (SEM, AFM), which provide basic support for a qualitative description

of the lateral nano-structures, geometrical parameters such as widths, thicknesses, gaps, resistivities and the interface resistances were extracted for several sample sets, based on Al, Cu and Au non-magnetic spin channels. These parameters have been used in 1D and 3D models for the extraction of the material parameters l_{sf}^{N} and P_{eff}, for Al, Cu and Au based nano-structures. A good agreement of both models and the experimental data was found. At the end of this thesis, similar efficiency of spin injection has been achieved for both the multi-level and the multi-angle approaches, what is important, since SHE experiments involve the LSV nano-structures where both nano-fabrication methods are combined. Also, an alternative 1D model, based on the transfer matrix approach, has been used for l_{sf}^{N} and the interface spin-flip probability evaluation, which takes into account the bulk and the interface effects. This model revealed that a higher interface spin-flip probability is responsible for a lower effective spin polarization. However, the large number of correlated free parameters gives high incertitudes for extracted values. Similarly, as for the 1D model, presented earlier, several sets of free parameters can be found, which allow good fitting of the experimental data. Nevertheless, we can well predict and analyze quantitatively the evolution of the spin signal in view of spin Hall effect experiments.

Chapter 4

Lateral confinement effect

In standard all-metallic LSVs the level of spin accumulation and the resulting spin signal are primarily limited by the relaxation of the spin accumulation in the ferromagnet. Then, eventually, the spin signal can be governed by the relaxation in the lateral channel, in the central part, but also in its two extensions outside the central part. It has been recently shown that the introduction of tunnel barriers at the interface between the lateral channel and the electrodes, by preventing the diffusion of the spin accumulation into these electrodes, suppresses a part of the spin relaxation and enhances the spin signal significantly [108, 82, 109, 110]. In this chapter, in the same context, we demonstrate that the spin signal can be significantly enhanced (by 100%) in LSV structures, confining the spin accumulation into the useful central part of the channel [111]. This prevents its diffusion and relaxation outside the central part, avoiding a significant mechanism of spin relaxation occurring in standard open geometries.

4.1 Samples and measurements

Let us consider the equivalent electrical resistor-circuit, corresponding to the LSV, represented in figure 4.1(a-c). In this representation, the size of the rectangular resistor reflects its spin resistance value ($R^{(*)}_{N(F)} = \rho^{*}_{N(F)} l^{N(F)}_{sf}/A$). The spin currents flow preferably in the material having lower spin resistance, and therefore this material will mainly contribute to the relaxation process of the spin accumulation. As it can be clearly seen, the injected spins, in the case of $R^{*}_{F} \ll R_N$, will flow mainly in the magnetic material [cf. *Fig. 4.1(a)*]. In the other case, when $R_N \sim R^{*}_{F}$, they will flow mostly in N.

Thus, since the Py ferro-magnetic electrodes are used, the best situation to evidence the lateral confinement effect is the case where $R^{*}_{F} \sim R_N$. In this range, since the spin resistances for both ferro-magnet and normal channel become comparable, almost the same amount of the spin current relaxes in the ferro-magnet as in the non-magnetic channel.

In order to evidence the spin signal enhancement by lateral confinement, we prepared two kinds of lateral spin-valves (LSV), with non-magnetic Au channels: a standard one, hereinafter called open (O), characterized by a channel extending outside the two contacts over distances larger than the channel spin diffusion length (cf. *Fig. 4.2(b)*), and another one with a confined

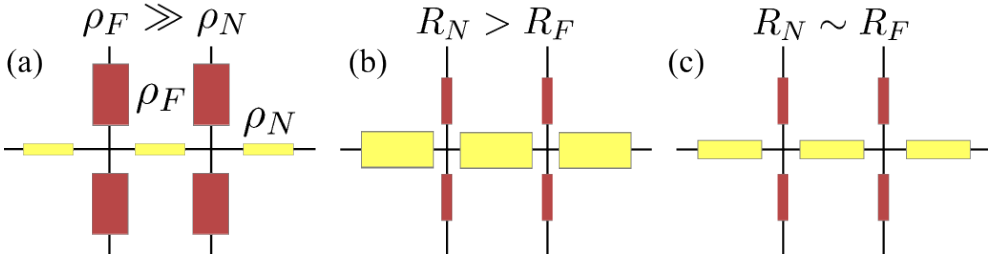

Figure 4.1: *Electric circuit schematics of the lateral spin-valve nano-structure for (a) charge and (b-c) spin current. The normal (spin) resistances are represented by red and yellow squares for ferro-magnetic and non-magnetic material respectively, and their size reflects the value of the resistance attributed to flowing charge/spin current. In the case of the spin current circuit two cases are represented: (b) $R_N > R_F^*$ which is valid for Py/Al and Py/Cu, and (c) $R_N \sim R_F^*$ which stands for the case of Py/Au nano-structures.*

geometry, hereinafter called confined (C) [cf. *Fig. 4.2(a)*].

In this confined geometry, the Au channel only connects $F1$ and $F2$ without extending further to the left and to the right. In each configuration, we note L, the distance between $F1$ and $F2$, calculated from the center of the F/N cross to the center of the second cross. We emphasize that both types of nano-devices were batched on the same run of material evaporation, ion-milling and nano-lithography processes with the results that their material characteristics (resistivity, spin diffusion length and spin asymmetry) are identical. The local spin signals (or magneto-resistance MR) will be compared for the devices O and C. Additional information is taken from non-local (NL) measurements (see central sketch in *Fig. 4.2(c)*) on devices O (non-local measurements are not possible on devices C).

The devices are fabricated by means of the multi-level e-beam lithography. They consist of the two permalloy (Py) stripes connected with a non magnetic Au channel (cf. *Fig. 4.2*). First, $15\,nm$ thick (t_F) and $50\,nm$ wide (w_F) Py electrodes are deposited on a SiO_2 substrate. A nucleation pad in the injector (F1) makes its reversal field smaller than that of the detector ($F2$). The next step in the nano-fabrication process is the cleaning of the F/N interface by ion-milling before the deposition of a $70\,nm$ thick (t_N) and $50\,nm$ wide (w_N) non-magnetic Au channel (N), connecting the two Py contacts. The ion-milling procedure has been optimized as presented in *Chapter 2*.

Concerning the parameters of the materials, we note $R_F^* = \rho_F^* l_{sf}^F / A_F = \rho_F l_{sf}^F / [(1 - P_F^2) A_F]$ and $R_N = \rho_N l_{sf}^N / A_N$, the respective spin resistances of Py and Au, where $\rho_{N(F)}$, P_{eff}, $l_{sf}^{N(F)}$ and $A_F = w_F \times w_N$ ($A_N = w_N \times t_N$) stand for the resistivity of F or N, the spin polarization of the resistivity in F, the spin diffusion length and the area of the ferromagnetic injector/detector contacts (the section of the channel). Typical values at $77K$, deduced from previous experiments [cf. *Chapter 3*] [69], are $\rho_F = \rho_F^* \times (1 - P_F^2) \simeq 11.8\,\mu\Omega.cm$, $\rho_N \simeq 3.5\,\mu\Omega.cm$, together with $l_{sf}^F \simeq 5.5\,nm$ [68] and a relatively short $l_{sf}^N \simeq 90 - 100\,nm$. Those values are in a close agreement with those reported in the literature for similar Py/Au LSV structures [104, 112]. The effective bulk spin polarization of Py, P_{eff}, is estimated to be approximately 0.31 ± 0.05, from preliminary experiments on a series of Py/Au LSV. This value is close to other findings for the spin injection

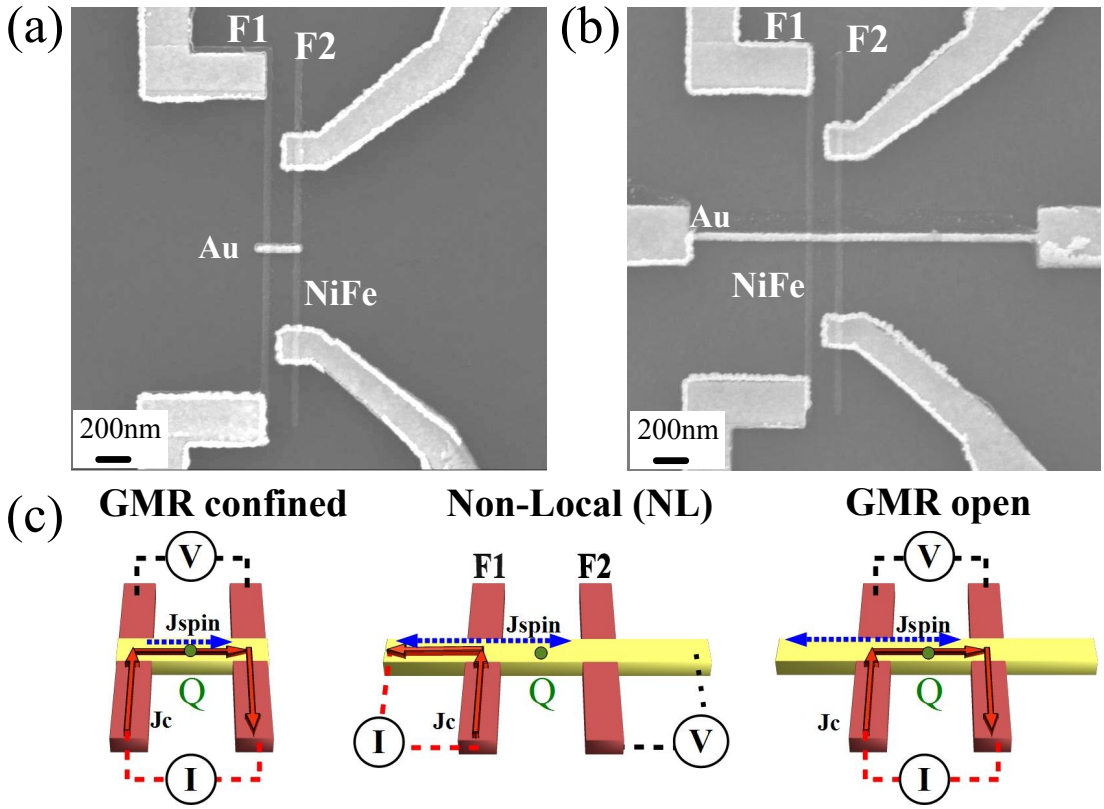

Figure 4.2: *Scanning Electron Microscopy (SEM) image of Py/Au lateral spin-valve (LSV) nano-devices characterized by (a) a lateral confined (C) geometry and (b) standard open (O) geometry. (c) Sketches of the current and voltage contacts to measure local spin signals (MR) in confined (left) or open (right) geometry and non-local spin signals (center). The Q point is the central point of the channel between the two ferromagnetic contacts.*

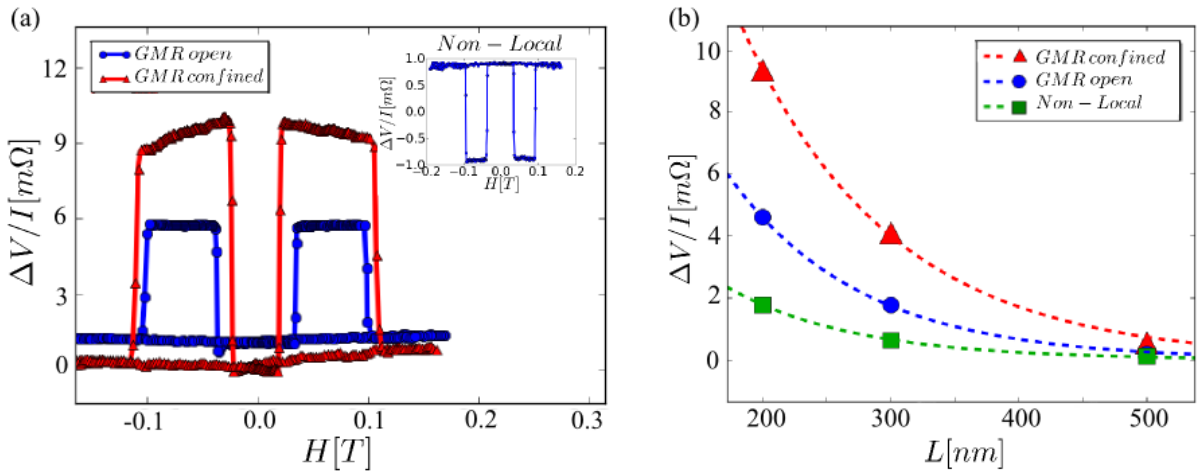

Figure 4.3: *$\Delta V/I$ versus magnetic field at $77K$ for a Py/Au LSV with $L = 200nm$ for the distance between the two ferromagnetic contacts. The blue dotted curve corresponds to an open channel whereas the red curve with triangles corresponds to a confined channel. The non-local (NL) signal obtained for the open channel is displayed in the inset of (a). (b) Local (MR) spin signals for confined (red triangles) or open (blue dots) LSV and non-local spin signals (green rectangles) as a function of the L between the ferromagnetic stripe injector ($F1$) and ferromagnetic stripe detector ($F2$). Data were recorded at $77K$. The dashed curves represent the fit with theoretical expressions for the spin signal (see text).*

from Py in similar LSV, $P_{eff} \approx 0.26$ [104]. This gives *in fine* $R_F^* \simeq 0.5\,\Omega$ and $R_N \simeq 1\,\Omega$ and a characteristic ratio R_F^*/R_N for Py/Au close to 0.5. The same ratio is only about 0.25 for Py/Cu and 0.1 for Py/Al (when taking $\rho_{Cu} = 10\,\Omega.nm$, $l_{sf}^{Cu} \sim 500\,nm$ and $\rho_{Al} = 20\,\Omega.nm$, $l_{sf}^{Al} \sim 600\,nm$). As the spin relaxation in F and N is inversely proportional to R_F^* and R_N respectively, the proportion of spin relaxation in N is expected to be more important in Py/Au than in Py/Cu or Py/Al, which makes that Py/Au is a more favorable system for the observation of a signal enhancement due to the reduction of the relaxation volume in N by confinement. The best situation for the observation of confinement effects would be the limit $R_F^* \gg R_N$, as shown below. As presented in figure 4.2, we expect to increase the spin signal by cutting the lateral channel outside the ferro-magnetic electrodes, if $R_F^* \sim R_N$.

For both types of devices, a $100\,\mu A$ ac current was injected using a lock-in amplifier at $379\,Hz$ to measure the in-phase component of the output voltage. Data were acquired at $77\,K$, with a magnetic field oriented along the ferromagnetic wires. In Fig. 4.3(a) we show the magnetoresistance for O (blue dots) and C (red triangles) samples with $L = 200\,nm$. A well-defined plateau of higher resistance is clearly seen in the anti-parallel magnetic configuration of $F1$ and $F2$. The amplitude of the MR signal equals $\Delta R_O = 4.6\,m\Omega$ for sample O and $\Delta R_C = 9.3\,m\Omega$ for sample C which evidences an enhancement by almost 100 % when the Au channel is confined. Those measurements represent the experimental proof of a signal enhancement by lateral confinement. As a corollary, the NL spin signal acquired for sample O and displayed in the inset of Fig. 4.3(a) equals $\Delta R_{NL} = 1.8\,m\Omega$, is a little less than one half of the local signal of the same sample. The change in the current and voltage probe configurations, enlarge the distance

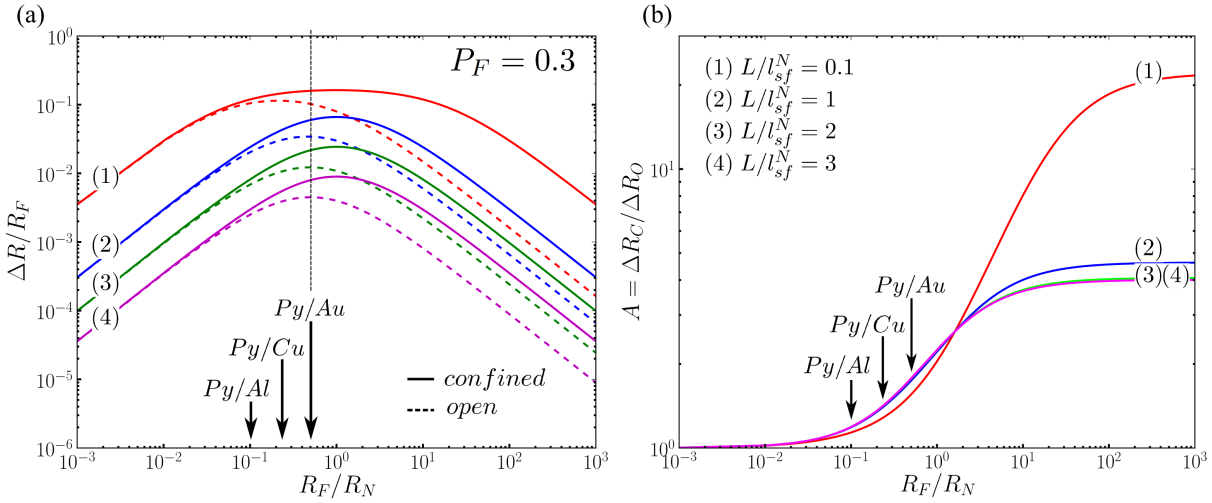

Figure 4.4: *(a) The magneto-resistance ratio $\Delta R/R_F$ calculated for O and C structures and (b) the corresponding amplification factor between O and C, $A = \Delta R_C/\Delta R_O$. These are plotted versus R_F/R_N for different values of the gap L between F1 and F2: (1) $L/l^N_{sf} = 0.1$, (2) $L/l^N_{sf} = 1$, (3) $L/l^N_{sf} = 2$ and (4) $L/l^N_{sf} = 3$.*

between center of current distributions in the injector and detector for the NL configuration with respect to GMR. This can explain the factor between GMR and NL measurements is a little larger than 2 (inhomogeneous distribution of current lines at the interfaces) [74]. Similar open and confined Py/Au nano-devices were fabricated with different distances L=200 (a), 300 (b) and 500 nm (c). The variation of the spin signals for O and C devices are presented on Fig. 4.3(b). The enhancement of the local MR signals for the confined geometry compared to the open one is clearly observed, corresponding to an increase of ΔR from 1.9 $m\Omega$ (O) to 3.9 $m\Omega$ (C) for $L = 300\,nm$ and from 0.4 $m\Omega$ (O) to 0.8 $m\Omega$ (C) for $L = 500\,nm$. Otherwise, from the quasi-exponential decrease of the signals with L, the spin diffusion length can be estimated to be about $90 - 100\,nm$ using equations 4.1 presented in the following. One will see below (cf. *Fig. 4.6(d)*), that a constant value of the enhancement by confinement is expected by the calculation for $L > l^N_{sf}$. This is what has been observed, with an amplification factor approximately constant and of the order of 100% for large L compared to l^N_{sf}. On the other hand, the non-local signals for samples of type O are respectively (1.9 $m\Omega$ for $L = 200\,nm$) 0.8 $m\Omega$ for $L = 300\,nm$ and 0.2 $m\Omega$ or $L = 500\,nm$, which are close to the half values of the corresponding MR in the conventional open geometry expressions [113].

4.2 Results and theory/simulation comparison

The enhancement of the spin signal by confinement in Py/Au nano-devices can be understood in the frame of the 1-dimensional (1D) analytical theory of spin transport [13] and of the formalism of the transfer matrix method developed by Jaffres *et al.* [82]. When describing the used system with the transfer matrix theory, the following expressions can be developed for open and close geometry [cf. *Chapter 3*] $\Delta R_{O(C)}$ [111]:

	$R_F \gg R_N$		
Geometry of LSV	$L \geq l_{sf}^N$	$L < l_{sf}^N$	$L \ll l_{sf}^N$
Amplification factor A	$\sim L/l_{sf}^N$	$> L/l_{sf}^N$	$4\,l_{sf}^N/L$

Table 4.1: *Summary of the results of the amplification factor A for different geometries of the LSV nano-structures in some limit cases.*

$$\begin{aligned} \frac{\Delta R_O}{R_N} &= \frac{8P_F^2 R_F^{*2}}{(2R_F^*+R_N)^2 \exp\left(\frac{L}{l_{sf}^N}\right) - R_N^2 \exp\left(-\frac{L}{l_{sf}^N}\right)} \\ \frac{\Delta R_C}{R_N} &= \frac{8P_F^2 R_F^2}{(R_F^*+R_N)^2 \exp\left(\frac{L}{l_{sf}^N}\right) - (R_F-R_N)^2 \exp\left(-\frac{L}{l_{sf}^N}\right)} \end{aligned} \tag{4.1}$$

from which one can deduce the enhancement factor:

$$A = \Delta R_C/\Delta R_O \tag{4.2}$$

As shown in Fig. 4.3(b), a good fit is obtained by introducing $l_{sf}^N = 98\,nm$ in the above equations, as well as for the variation of the ΔR_C and ΔR_O with L (dashed lines). Thus the enhancement factor by confinement in our samples is $A = \Delta R_C/\Delta R_O = 2$, what gives 100%. The calculated $MR = \Delta R/R_F$ and the enhancement factor are presented on Fig. 4.4 *versus* R_F^*/R_N. For a low R_F^*/R_N ratio, it will give $\Delta R \approx 4P_F^2 R_F^{*2}/[R_N \sinh(L/l_{sf}^N) + 2R_F \exp(L/l_{sf}^N)]$, in each case ($O$ and C). There is no signal enhancement for $R_F^* \ll R_N$, because in this limit the spin relaxation process occurs mainly in the ferromagnet F and not inside the channel N. The spin signal enhancement A begins for $R_F^*/R_N \simeq 0.5$ (in the case of Py/Au) and flattens out for $R_F^*/R_N \gg 1$ [cf. *Fig. 4.4(b)*]. The enhancement coefficient A depends weakly on the ratio L/l_{sf}^N of the LSV in the range of $L \geq l_{sf}^N$ (our samples and curves 2-4 in *Fig. 4.4(b)*). It becomes much larger (curve 1 in *Fig. 4.4(b)*) for $L < l_{sf}^N$ with also $R_F^*/R_N \gg 1$, and very large, of the order of $4\,l_{sf}^N/L$, for $L \ll l_{sf}^N$ [82]. This ratio can be easily understood if we consider the volume, where spins relax: for open geometry, spins produced at the 2 interfaces spread in length l_{sf} on each side, whereas they relax in a volume proportional to L in the close geometry.

It is interesting to understand how the enhancement of the magneto-resistance results from the enhancements of both the spin polarization of the current and the spin accumulation. We call $\mathcal{P}^{\uparrow\uparrow}$ the current spin polarization at midway between F1 and F2 (Q in *Fig. 4.2(c)*) in the parallel magnetic configuration of F1 and F2, and we call $\Delta\mu^{\uparrow\downarrow}$ the spin accumulation at Q in the anti-parallel configuration. In the case of two identical contacts in nature and size we can write:

$$\begin{aligned} \mathcal{P}_C^{\uparrow\uparrow} &= \frac{\mathcal{M}_{42}\mathcal{M}_{22}\exp(\frac{L}{2l_{sf}^N}) - \mathcal{M}_{42}\mathcal{M}_{32}\exp(-\frac{L}{2l_{sf}^N})}{(\mathcal{M}_{22})^2\exp(\frac{L}{l_{sf}^N}) - (\mathcal{M}_{32})^2\exp(-\frac{L}{l_{sf}^N})} \\ \frac{\Delta\mu_C^{\uparrow\downarrow}}{2R_N} &= \frac{\mathcal{M}_{42}\mathcal{M}_{22}\exp(\frac{L}{2l_{sf}^N}) + \mathcal{M}_{42}\mathcal{M}_{32}\exp(-\frac{L}{2l_{sf}^N})}{(\mathcal{M}_{22})^2\exp(\frac{L}{l_{sf}^N}) - (\mathcal{M}_{32})^2\exp(-\frac{L}{l_{sf}^N})} \end{aligned} \tag{4.3}$$

where M_{22}, M_{32}, M_{42} can be extracted from the transfer matrix approach:

	M_{22}	M_{32}	M_{42}
open	$\frac{R_F^*+R_b^*}{R_N}+\frac{1}{2}$	$-\frac{1}{2}$	$\frac{\beta_F R_F^*+\gamma R_b^*}{R_N}$
closed	$\frac{R_F^*+R_b^*+R_N}{2R_N}$	$\frac{R_F^*+R_b^*-R_N}{2R_N}$	$\frac{\beta_F R_F^*+\gamma R_b^*}{R_N}$

The general law for the O and C systems can be written in the form:

$$\mathcal{P}^{\uparrow\uparrow}\Delta\mu^{\uparrow\downarrow}-\mathcal{P}^{\uparrow\downarrow}\Delta\mu^{\uparrow\uparrow}=eJ\Delta R \tag{4.4}$$

Note that in this formulation ΔR represents only the one F/N interface. In the case of symmetric devices ($F1\equiv F2$), one can take advantage of $\mathcal{P}^{\uparrow\downarrow}=0$ and $\Delta\mu^{\uparrow\uparrow}=0$, at the central point Q (cf. *Fig. 4.2*) between $F1$ and $F2$ [cf. *Chapter 1, Fig. 1.4*], and write:

$$eJ\Delta R_{O(C)}=2\mathcal{P}^{\uparrow\uparrow}\Delta\mu^{\uparrow\downarrow} \tag{4.5}$$

As shown in Fig. 4.5, and in Fig. 4.6, the product of the calculated values of $\mathcal{P}^{\uparrow\uparrow}$ and $\Delta\mu^{\uparrow\downarrow}$ at point Q, reproduces the bell-shaped variation of $\Delta R_{O(C)}/R_F^*$ as a function of R_F^*/R_N shown in Fig. 4.4(a), and also directly calculated in several publications [cf. [114]]. The situation in which $\mathcal{P}^{\uparrow\uparrow}$ is tending to zero for $R_F^*\propto\rho_F^* l_{sf}^F\ll R_N\propto\rho_N l_{sf}^N$ in Fig. 4.5(a), is well-known in the problem of spin injection from a magnetic metal into a semiconductor with $\rho_F\ll\rho_N$ (conductivity mismatch effect [115, 17, 114, 116]). When both F and N are metals, the equivalent situation $R_F^*\ll R_N$, occurs when the spin diffusion length is much shorter in F than in N, for example, in the couple Py/Al this leads to $R_F^*/R_N\approx 0.1$. As R_F^*/R_N increases, $\mathcal{P}^{\uparrow\uparrow}$ increases and flattens off for $R_F^*/R_N\gg 1$. For $\Delta\mu^{\uparrow\downarrow}$ the variation in Fig. 4.6(a) illustrates the drop of the spin accumulation, when for $R_F^*/R_N>l_{sf}^N/L$ the electron dwell time exceeds the spin lifetime [114].

The enhancement of ΔR_C with respect to ΔR_O by confinement comes from the enhancement of both terms of Eq. 4.5, $\mathcal{P}^{\uparrow\uparrow}$ (the shift between the solid and dashed lines in Fig. 4.5(a-b)) and $\Delta\mu^{\uparrow\downarrow}$ (the shift between the solid and dashed lines in *Fig. 4.6(a) and (b)*). Of course, on both $\mathcal{P}^{\uparrow\uparrow}$ and $\Delta\mu^{\uparrow\downarrow}$ the enhancement is the largest for $R_F^*\gg R_N$, when the spin relaxation is predominantly in N rather than in the electrodes. The importance of the confinement effects depends also on the ratio between L and l_{sf}^N. The reduction of the spin relaxation zone in N by a factor $\approx L/(L+2l_{sf}^N)$, increases the spin accumulation $\Delta\mu^{\uparrow\downarrow}$, more for $L<l_{sf}^N$ than for $L>l_{sf}^N$ (compare curves 1 and 4 in *Fig. 4.6(b)*). This is explained by the fact that the enhancement of the spin accumulation by confinement is more effective when $L<l_{sf}^N$. The situation is opposite for the current spin polarization in the parallel configuration, $\mathcal{P}^{\uparrow\uparrow}$, with confinement effects larger for $L\geq l_{sf}^N$ (curves 2-4 in *Fig. 4.5(b)*) and tending to zero for $L\ll l_{sf}^N$ (curve 1 in Fig. 4.5(b)). This is explained by the fact that for $L<l_{sf}^N$, $P_{\uparrow\uparrow}$ tends to the bulk polarization of the F electrodes, and there is no influence of the confinement. Our **experimental results correspond to the**

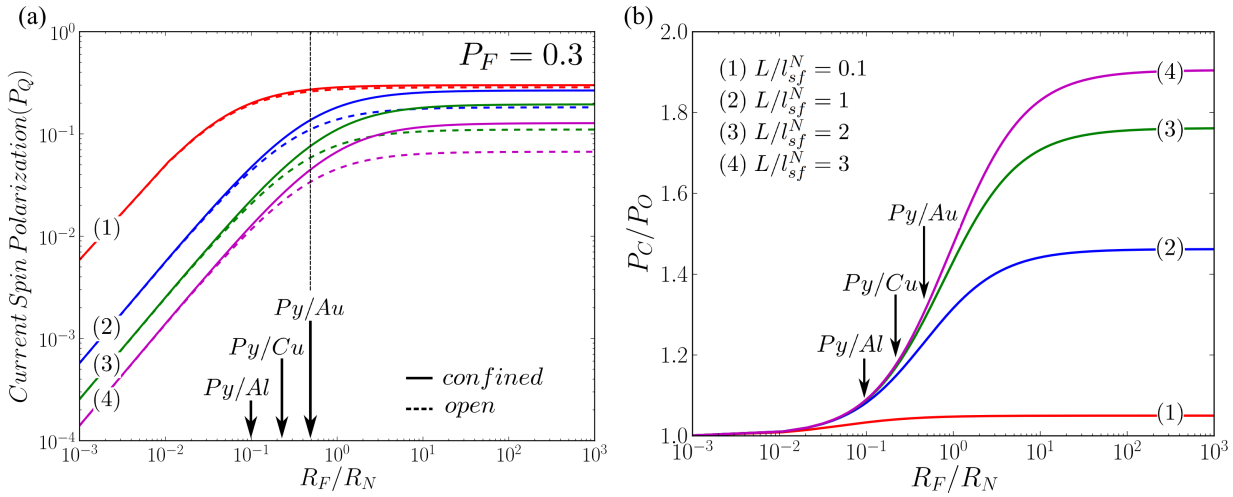

Figure 4.5: *(Color line) (a) Current spin-polarization ($\mathcal{P}^{\uparrow\uparrow}$) in the magnetic parallel state at point Q and (b) amplification of $\mathcal{P}^{\uparrow\uparrow}$ for confined systems vs R^*_F/R_N, for different L/l^N_{sf} ratios.*

situation for $L = 200 - 500\,nm > l^N_{sf} = 98\,nm$, and the confinement-induced increase of the spin signal (the calculated curves in *Fig. 4.3(b)*) comes at equal part from the two terms, $\mathcal{P}^{\uparrow\uparrow}$ and $\Delta\mu^{\uparrow\downarrow}$, of Eq. 4.5.

Note that the above discussion could be extended to cases with significant interface resistances (the tunnel junction, for example) between the electrodes and channel, by replacing the spin resistance R^*_F by the interface resistance R_T, when $R_T \gg R^*_F$, or by a combination of R_T and R^*_F.

By confinement of the spin relaxation inside the length L between $F1$ and $F2$, the MR of a LSV becomes close to that of the CPP-GMR in a magnetic trilayer [117]. Actually, with at least the same cross section A_N and A_F, the spin signal ΔR_C of the LSV is exactly the same as the ΔR of a CPP-GMR experiment of a trilayer, including a nonmagnetic layer of thickness L between two magnetic layers of thickness t_F, that is much larger than the spin diffusion length (this result and the correction factor for different A_N and A_F can be found in [82, 114]). The situation of CPP-GMR in a trilayer with ultra-thin magnetic layers (and thus negligible spin relaxation in these layers) could be found in a LSV by introducing tunnel barriers of resistance R_T between the lateral channel and the magnetic electrodes, to prevent the expansion of the spin accumulation into the electrodes and to confine completely the spin relaxation inside the length of the channel (this can be obtained for $R_T \gg R^*_F$). With this double confinement for large enough R_T and $L \ll l^N_{sf}$, the spin signal would approach the very large values obtained in CPP-GMR. The LSVs for which this situation could be found (with relative MR up to 72% and ΔR in the $M\Omega$ range) are LSVs composed of carbon nano-tubes between tunnel contacts with magnetic electrodes [118]. Similarly, LSVs with graphene, as a non-magnetic channel, have shown MR of 10% with ΔR in the $10\,M\Omega$ range [5].

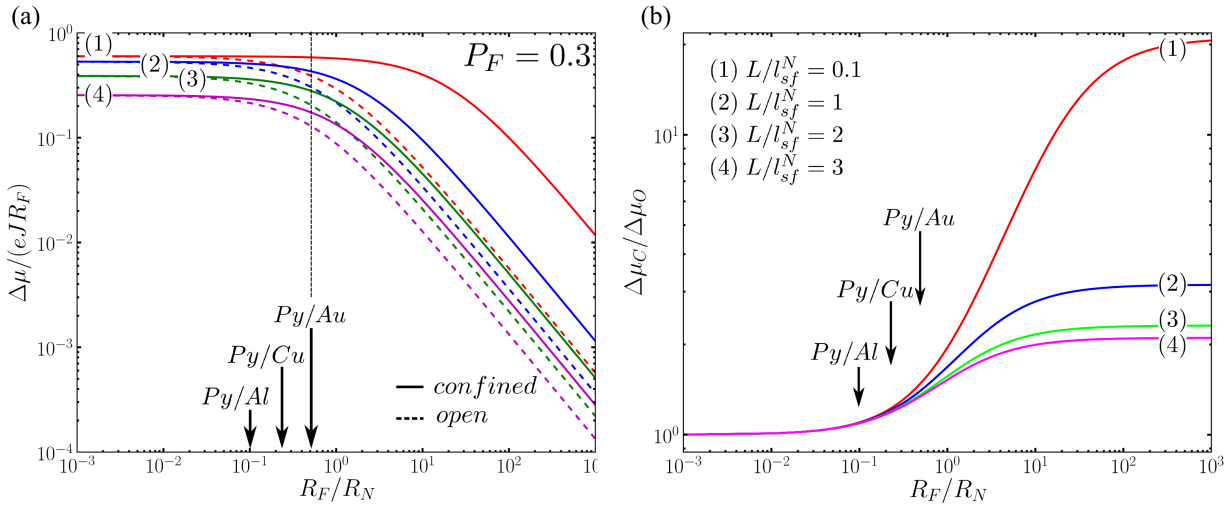

Figure 4.6: *(a) Spin accumulation $\Delta\mu^{\uparrow\downarrow}$ in the magnetic anti-parallel state at point Q and (b) amplification of $\Delta\mu^{\uparrow\downarrow}$ vs. R_F/R_N for different gap lengths. For all figures, the different values of L/l_{sf}^N are indicated in (b).*

4.2.1 Simulations of the lateral confinement

Figure 4.7(a) represents the numerical calculations using Eq. 4.1. Figure 4.7(b) represents the FEM simulations of the amplification factor as a function of the non-magnetic channel parameters l_{sf}^N and ρ_N. Both the numerical calculation and the FEM simulations were performed for the geometry corresponding to our experiments on Py/Au nano-structures : $L = 200\,nm$ $w_F = 50\,nm$, $t_F = 20\,nm$, $\rho_F = 11.8\,\mu\Omega.cm$, $w_N = 50\,nm$, $t_N = 70\,nm$.

For decreasing l_{sf}^N and resistivity of the non-magnetic channel, the amplification factor increases. Therefore, in this kind of material the lateral confinement plays an important role, since the spin signal can be increased over 100%. In contrast, in the case of Al and Cu based nano-structures, this effect is of the order of 30% (when taking $\rho_{Al,Cu} \sim 15\,\Omega.nm$ and $l_{sf}^{Al,Cu} \sim 600\,nm$), as the ratio R_F^*/R_N for these materials is smaller than 0.5 (case of Au).

If one considers the case of Au, where $\rho_{Au}^{77K} = 35\,\Omega.nm$ and $l_{sf}^{Au} = 100\,nm$, the corresponding amplification factors are of the order of 90% for numerical calculations and of the order of 70% for the FEM simulations. These results are in a good agreement with the experimental value of 100%.

By increasing the spin diffusion length up to $l_{sf}^N = 500 - 600\,nm$ and considering the case of Py/Al or Py/Cu ($R_N \gg R_F^*$), taking the resistivity $\rho_N = 35\,\Omega.nm$, one can find the amplification factor of 35%, which corresponds to the amplification factor A=1.3 (following the notation of *Fig. 4.4(b)*), when $R_F^*/R_N = 0.1$ in Fig. 4.4(b). This result proves also that there is a good agreement between the FEM simulations and theoretical description developed for this geometry and based on the transfer matrix approach.

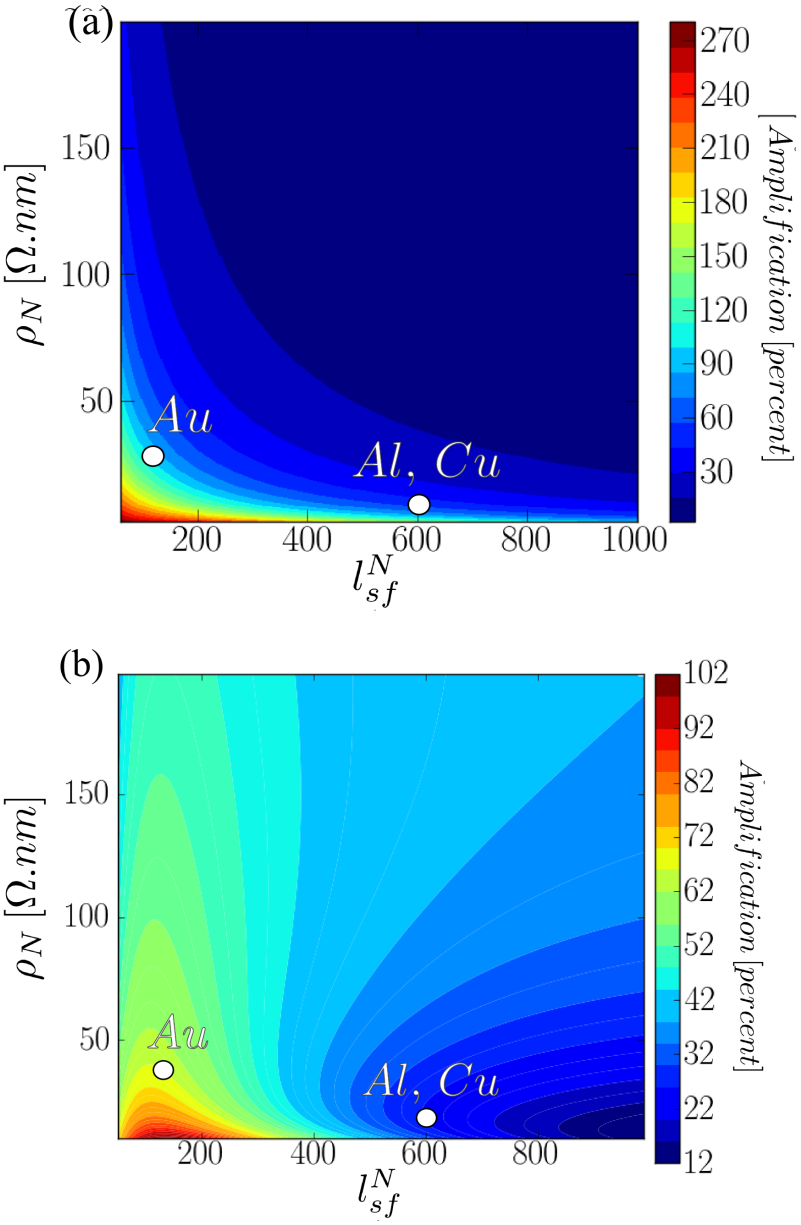

Figure 4.7: *(a) Numerical calculation and (b) FEM simulations of the amplification factor as a function of* l_{sf}^N *and* ρ_N*, where the following parameters were used:* $L = 200\,nm$*,* $w_F = 50\,nm$*,* $t_F = 20\,nm$*,* $\rho_F = 118\,\Omega.nm$*,* $w_N = 50\,nm$*,* $t_N = 70\,nm$*,* $P_F = 0.36$*. For the FEM simulations* ρ_N *was varied every* $1\,\Omega.nm$*, while* l_{sf}^N *every* $10\,nm$*, for numerical calculations these steps were* $0.2\,\Omega.nm$ *and* $1\,nm$ *respectively.*

4.3 Conclusions

The significant increase (about 100%) of the Magneto-Resistance of Py/Au lateral spin-valve, obtained by confining the Au channel to its minimum length inside the contact region, has been demonstrated. This enhancement of the spin signal is due to the reduction of the volume in which the spin accumulation relaxes. In general, the enhancement is related to both the enhancement of spin accumulation and the current spin polarization.

The theoretical description based on the transfer matrix approach was successfully applied for a study of the amplification effect. This showed that in the present case, the effect of the current spin polarization is more pronounced than the effect of the spin accumulation. These results pointed out that a stronger enhancement of the spin signal can be obtained, when magnetic tunnel junctions are inserted at the contacts to suppress the contributions of the spin relaxation, not only on the sides of the channel but also in the electrodes.

Moreover, the numerical calculations, based on the transfer matrix model, and the FEM simulations provided a powerful support in the study of the amplification factor for various materials. In the case of the presented Py/Au nano-structure, the value of the amplification factor was found to be in the range of $70 - 90\%$, which is in a good agreement with the experimental evaluation of 100%.

Different geometry and configuration were investigated, showing that for $R_F \ll R_N$ the relaxation process occurs mainly in the ferromagnet and not inside the channel, and therefore very little signal enhancement will be observed with the lateral confinement. Otherwise, when $R_F^* \gg R_N$ one needs to take into consideration the devices geometry with the amplification starting already when $R_F^*/R_N \simeq 0.5$. For $L \geq l_{sf}^N$ the amplification factor of the order of $A = 2$ should be expected, reaching up to $4l_{sf}/L$ in the case, when $L \ll l_{sf}^N$.

Chapter 5

Signal enhancement and spin precession in LSV with tunnel barriers

Lateral spin-valves with transparent contacts can be obtained by depositing directly the non-magnetic (N) wire on top of the ferro-magnetic (F) wires, but the resulting spin signal amplitude (ΔR) is relatively small [cf. *Chapter 2*]. In contrast, the insertion of a tunnel barrier or of a highly resistive contact at F/N interface leads to a great increase of the spins signal amplitude, as recently demonstrated experimentally by Fukuma *et al.* [108].

The insertion of a natural Al oxide at the interface between Py and Al results in a clear increase of the spin signals amplitudes. We will show in the following that we could achieve a value of $150\,m\Omega$ at $77\,K$ instead of $25\,m\Omega$ for transparent contacts [69]. The high spin signal amplitude comes from the fact that the main relaxation source for the spins, the ferro-magnetic electrodes, is disconnected from the non-magnetic channel. This represents the second type of confinement of the spin accumulation, complementary to the one presented in *Chapter 4*.

We show that it is also possible to carry out the non-local measurements by applying the external magnetic field not only along the ferro-magnetic wires, but also parallel to the N channel or out-of the samples plane. The out-of plane and in-plane spin precession in LSV can be then observed together with Hanle effect. These results can be fitted by the model developed by Fukuma [110], combined with the corrections proposed by Jedema [50]. This method allows the extraction of the key parameters of the LSV (l_{sf} and P_{eff}), using one sample instead of a batch, as done in the approach based on study of the gap dependence.

5.1 Samples and measurements

Spin-valves with naturally oxidized alumina barriers have been fabricated, where the active (central) part of the nano-structure is patterned entirely in one step, using the multi-angle evaporation technique [cf. *Chapter 2*]. It consists of two parallel permalloy (Py) wires connected by a non magnetic Al channel, with a natural aluminum oxide inserted at the interfaces between Py and Al [cf. *Fig. 5.1*]. First, the $20\,nm$ thick and $50\,nm$ wide Py electrodes are deposited on the Si substrate. Then a natural Al oxide is created by depositing $2\,nm$ of Al, followed by a $60\,s$

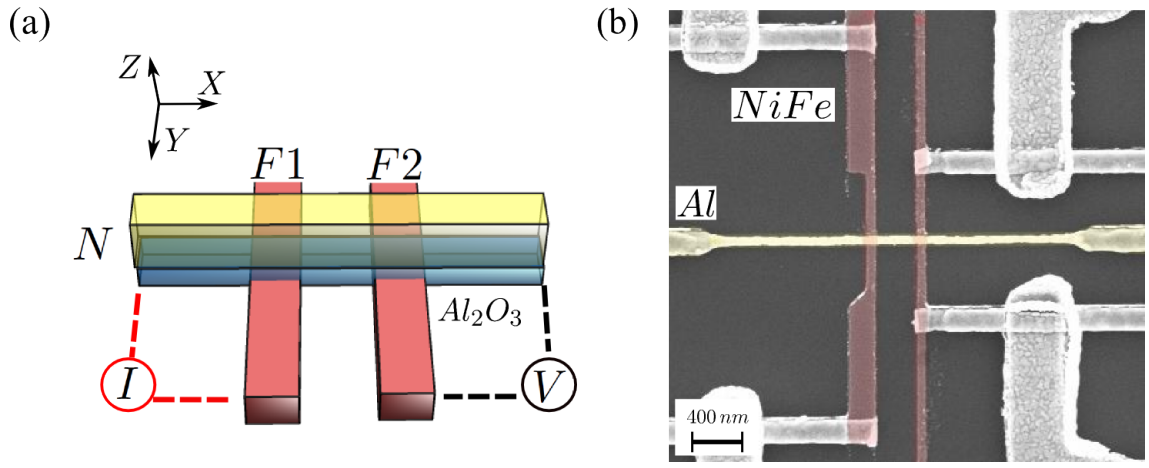

Figure 5.1: *(a) Schematic representation of the Non-Local probe configuration and (b) SEM image of the nano-structure consisting of two $NiFe$ ferro-magnetic electrodes connected by a non-magnetic Al channel with a thin layer of AlO_x.*

exposure to $10\,Torr$ of O_2. Finally, the $40\,nm$ thick and $50\,nm$ wide Al channel is deposited.

Figure 5.1 (a) represents the geometry of the above-mentioned device in the Non-Local probe configuration scheme, where red, yellow and blue color represents the F, N and alumina layers respectively. Figure 5.1(b) shows the SEM image of the fabricated nano-structure, with a multi-terminal connection to both interfaces.

Taking advantages of the four connections to each junction, the interface resistance was estimated using a pseudo four probes measurements [cf. *Chapter 3*] to be $R_b = 6\,k\Omega$ at both room temperature and $77\,K$. This suggests that, despite the small resistance-area product $RA = 15\,\Omega.\mu m^2$, the AlO_x layer behaves like a tunnel barrier. This value is smaller than what is usually reported for typical Al_2O_3 barriers, being $640\,\Omega.\mu m^2$ [36] or above, but it is still bigger than the MgO barrier ($0.2\,\Omega.\mu m^2$) of similar lateral structures [110].

5.2 Spin signal amplification

The spin signal amplification was evidenced for $Py/AlO_x/Al$ nano-device with the distance $L = 150\,nm$. The external magnetic field was swept along the ferro-magnet direction. Figure 5.2 (a) shows V/I measurements in the Non-Local probe configuration recorded at (a) $300\,K$ and (b) $77\,K$. The spin signal amplitude yields the value of $35\,m\Omega$ at $300\,K$ and $146\,m\Omega$ at $77\,K$. This has to be compared with $25\,m\Omega$, recorded at $77\,K$ in the case of similar Py/Al nano-structures with transparent interfaces [cf. *Chapter 2*].

This enhancement can be understood in view of the model developed in *Chapter 4*. The insertion of the high resistive AlO_x contacts avoids the spin relaxation in F. The analysis based on the ratio $R_F^*/R_N \ll 1$ has to be replaced by $R_b/R_N \gg 1$. In this case, the spin signal amplitude becomes proportional to R_N instead of R_F.

The non-local measurements were also performed in the two other directions of the magnetic field. In these cases, the application of the field induces the precession of injected spins in N,

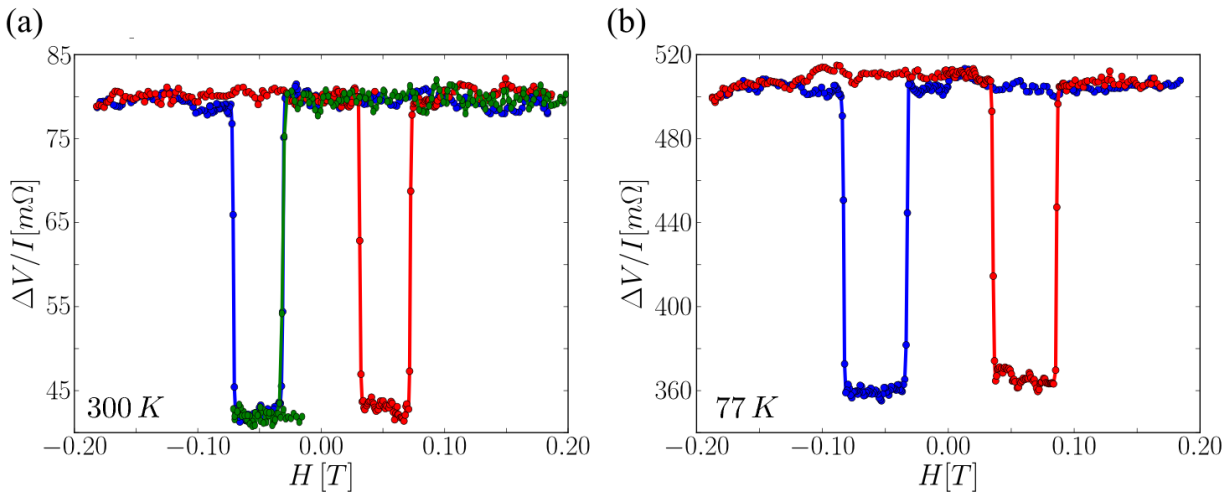

Figure 5.2: *The V/I measurements in Non-Local probe configuration recorded at (a) $300\,K$ and (b) $T = 77\,K$ for $Py/AlO_x/Al$ nano-device obtained by the multi-angle nano-fabrication method. The distance (center to center) between the ferro-electrodes is equal to $L = 150\,nm$. The spin signal amplitude yields $35\,m\Omega$ at $300\,K$ and $146\,m\Omega$ at $77\,K$. Red and blue curves correspond to positive and negative magnetic field sweep directions respectively. Green cycle stands for the minor hysteresis cycle.*

while diffusing, which results in a field-dependent oscillations of the spin signal. In the following, the use of the same experiment for studying of another physical effect, the so-called Hanle effect, will be presented. This is particularly suitable in the case of tunnel barriers, since it increases the electron dwell time or the time spent in the channel, thus allowing sizable oscillations to appear.

5.3 The Hanle effect

The spin precession offers a way to control the spin orientation in a ferromagnetic material without reversing its magnetization direction. It thus could be the basis of new spintronic devices (e.g. in the gate of a spin transistor using the Rashba effect or in a spin torque-based device to control the direction of the absorbed spin [77]).

When the magnetic field is applied along X or Z axis [cf. *Fig. 5.1(a)*], the spins injected in the non-magnetic channel precess around the applied field with the Larmor frequency given by [119, 110]:

$$\omega_L = g\mu_B H_{X,Z}/\hbar \tag{5.1}$$

where g is the Landé factor (for Al, $g \backsimeq 2$), μ_B is the Bohr magnetron and $\hbar$ is the reduced Planck constant.

Figure 5.3 shows simulations of the spin precession in a LSV for three cases. The first case is shown in the inset of figure 5.3(a), where the spins precess around an applied field with a constant amplitude of oscillation (no dispersion of spins orientation takes place). This is, however, not

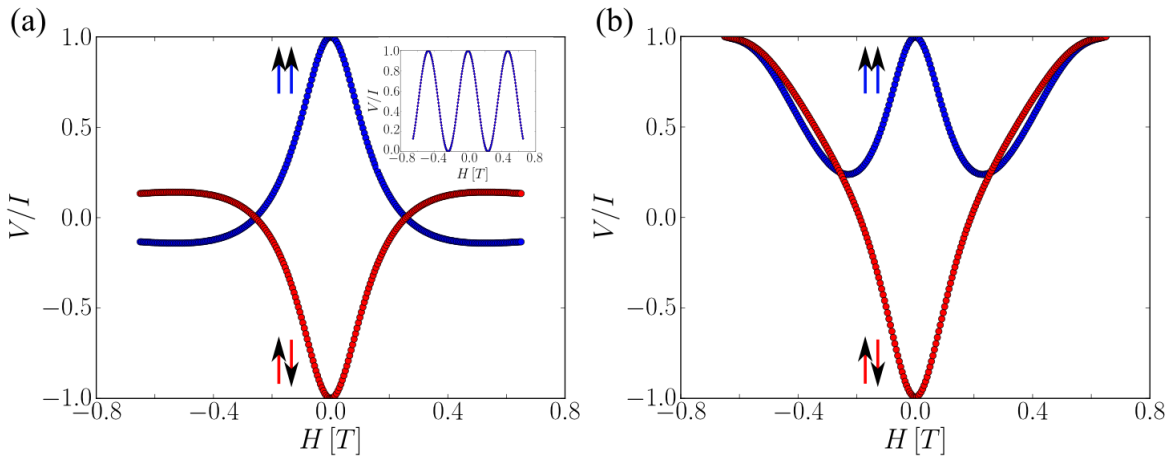

Figure 5.3: *Simulation results of the spin signal evolution due to the spin precession in LSV. (a) Stands for the angular dispersion of the detector due to the diffusive transport character. (b) Stands for the case of simulation taking into account the coherent rotation of the magnetization by the perpendicular field. Inset shows the oscillatory evolution without decoherence. Red and blue colors represent the anti-parallel and parallel starting configuration respectively.*

a real case, since the diffusive character of the electron transport in N induces a dispersion of times taken by the electrons to travel from the injector to the detector. It results in an angular dispersion of the spins orientations when arriving at the detector. As this dispersion enlarges with the precession frequency, the spin signal disappears for large applied fields: this phenomenon is known as the Hanle effect. This case is represented in figure 5.3(a). The third case, represented in figure 5.3(b), describes the situation, where not only the Hanle effect is taken into account, but also the fact that at high fields the magnetization direction of the ferro-magnetic electrodes is tilted out of the substrate plane with an angle θ (following Jedema *et al.* [48]). This aspect will be used in this chapter for the data analysis of the Hanle experiments.

In the following, LSV, having a natural oxide barrier (described above), will be used for studying the Hanle effect. In view of basic characterization of LSV, the Hanle effect is a powerful tool, since it allows the extraction of the spin diffusion length of the non-magnetic channel and the effective polarization in one single experiment.

The Hanle effect has been observed in semiconductors [120, 121, 122, 123] and in metallic based LSVs [119, 36]. Very recently, Fukuma *et al.* [110] observed these effects in a $Py/MgO/Ag$ LSV. In all these experiments the electrodes possess an in-plane magnetization, and the external magnetic field H is applied out-of-plane, i.e., perpendicularly to the layer (in the Z direction following notation of Fig. 5.1(a)). The spin current precesses consequently in the sample plane. Note that the Hanle effect appears because the magnetization of both the injector and the detector are orthogonal to the applied field. This non-collinearity is due to the shape anisotropy of the electrodes and is thus restricted to applied fields lower than the saturation fields.

Using very narrow ferro-magnetic electrodes, one can induce precession around an in-plane magnetic field parallel to the channel (e.g., in the X direction cf. *Fig. 5.1*). Both ferro-magnetic electrodes can be considered as a rectangular prism (50 nm wide, 2 μm long and 20 nm thick),

possessing the saturation magnetization $M_s = 650 \times 10^3\, A/m$. Theoretical calculations [124] of the demagnetizing factor for such geometry lead to the saturation fields of $H_Z^{sat} = 0.56\, T$ and $H_X^{sat} = 0.25\, T$ for the Z and X directions respectively. Thus with such geometry of the ferro-magnets it should be possible to observe the Hanle effect in both (X and Z) directions. When performing Hanle experiments, one uses the minor loops with an applied field parallel to the electrodes (along Y) to stabilize, at zero field, either the anti-parallel or the parallel magnetization state of the F electrodes [cf. *Fig. 5.2(a)*]. This magnetic state will be then used as a starting configuration for the Hanle measurement, for which the field is applied along the X or the Z directions [cf. *Fig. 5.1(a)*].

5.3.1 Magnetic characterization

The AMR measurements have been performed, followed by non-local measurements of the Hanle effect, for applied fields along X and Z axis. Figures 5.4(a-b) shows the AMR curves of the ferro-magnetic detector. The saturation fields can be estimated to $0.35\, T$ and $0.6\, T$ for X and Z respectively, which is in a good agreement with the theoretical expectations.

Figures 5.4(c-d) show the Hanle measurements for fields applied along X and Z. Already, for small fields, ΔR_{AMR} is being of the order of $10 - 20\%$ of its total amplitude, the magnetization is only slightly tilted. This corresponds to magnetic fields smaller than $0.1\, T$ along the X axis (c) and smaller than $0.2\, T$ along the Z axis (d). One can clearly observe the oscillation in the parallel magnetization. These oscillations are also clearly visible with the magnetic field applied along the X axis, which opens new possibilities for studying the effect of the field orientation on the spin diffusion. In this case, the spins precess out-of plane. The spin signal amplitudes for these measurements are $30\, m\Omega$ for X and $8\, m\Omega$ for Z direction. The differences in the spin signal amplitudes and in the background signal level are explained by an unexpected and undesirable electrical discharge that occurred between the two measurements. It results in a smaller polarization of the tunneling contacts.

5.3.2 Analysis methods

In order to fit the Hanle curves we can use the following equation taking into account the variation of the Z and X component of the magnetization with the applied field. The AMR resistance of the ferro-magnetic wire for an applied field $H_{X(Z)}$, along X(Z) is:

$$R(H_{X(Z)}, \theta) = R(H_{X(Z)}) cos^2\theta(H_{X(Z)}) + |R(H_{X(Z)} = 0)| sin^2\theta(H_{X(Z)}) \tag{5.2}$$

Where θ is the angle between the magnetization M of the Py nano-wires and the external magnetic field H. The angle value, $\theta(H)$, can be extracted from the fits of the AMR curves presented in figure 5.4(a-b), using the following relation:

$$R_{AMR}(H) = R_{min} + (R_0 - R_{min}) cos^2\theta(H) \tag{5.3}$$

Here, the Magnon Magneto-Resistance, which is responsible for the non-saturating behavior

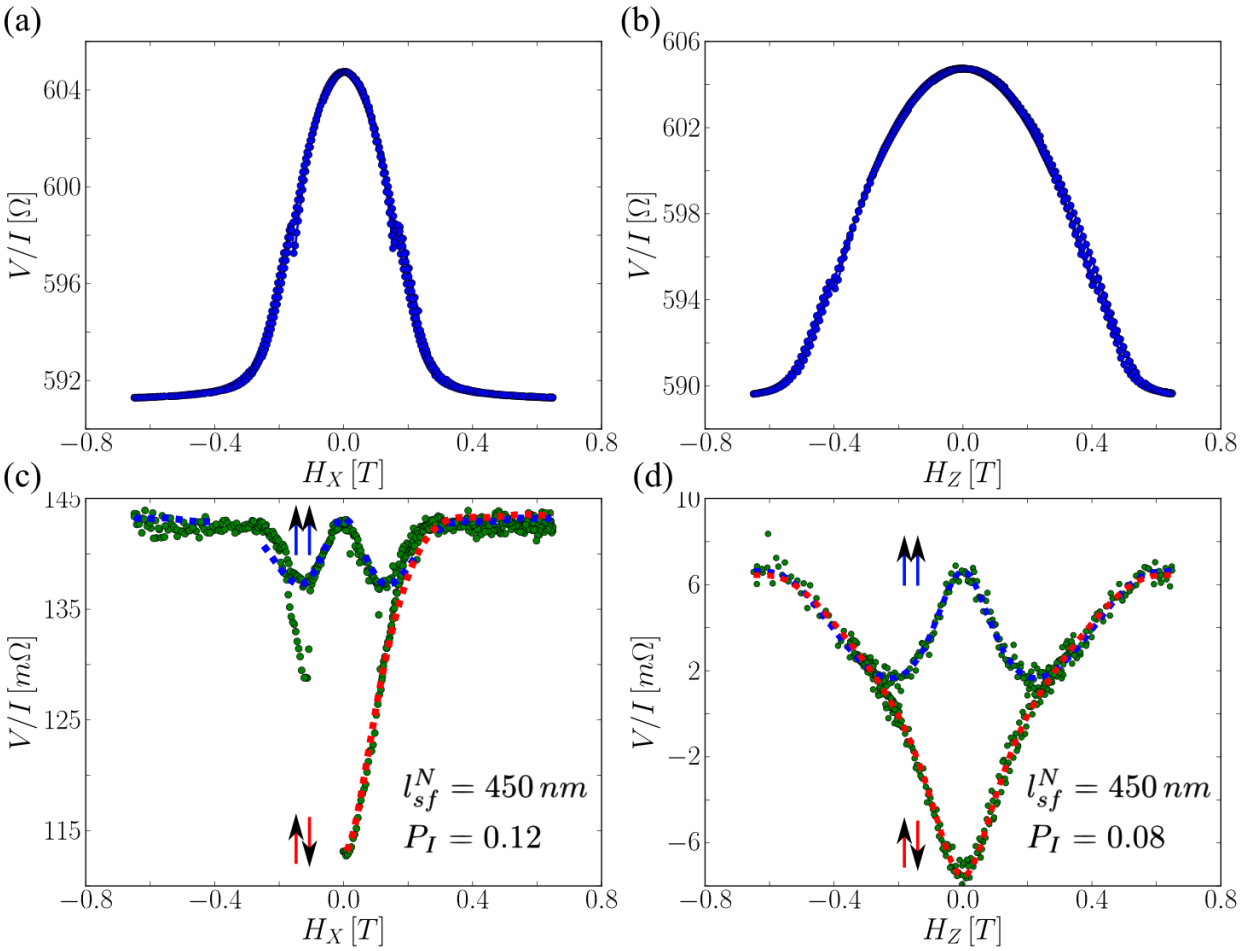

Figure 5.4: *(a-b) Anisotropic Magneto-Resistance curves of the Py nano-wires, obtained by sweeping the external magnetic field along the X (a) and Z (b) directions. (c-d) Experimental Hanle data-points (green dots) with the best fit (red and blue curves) using equation 5.2, corresponding to magnetic field swept along (a) X and (b) Z axis. Note that the symbols ⇈ and ↑↓ in (b) and (c) refer to the initial magnetic state.*

at high fields [88], is neglected in view of its small amplitude.

The $R(H_{X(Z)})$, for the magnetic field applied either along the X or the Z direction, is given by the model proposed by Fukuma *et al.* [110]:

$$R(H_{X(Z)}) = \pm \frac{4R_N^{\omega}[\frac{P_I}{1-P_I^2}\frac{R_b}{R_N^{\omega}} + \frac{P_F}{1-P_F^2}\frac{R_F}{R_N^{\omega}}]^2(\frac{Re(l_{sf}^{\omega}exp(-L/l_{sf}^{\omega}))}{Re(l_{sf}^{\omega})})}{[1 + \frac{2}{1-P_I^2}\frac{R_b}{R_N^{\omega}} + \frac{2}{1-P_F^2}\frac{R_F}{R_N^{\omega}}]^2 - (\frac{Re(l_{sf}^{\omega}exp(-L/l_{sf}^{\omega}))}{Re(l_{sf}^{\omega})})^2} \tag{5.4}$$

Where $l_{sf}^{\omega} = \frac{l_{sf}^N}{\sqrt{1+i\omega_L\tau_{sf}}}$, $R_F = \frac{\rho_F l_{sf}^F}{w_F w_N}$, $R_N = \frac{\rho_N l_{sf}^N}{t_N w_N}$. Here, l_{sf}^{ω} is the spin diffusion length in the presence of precession at the Larmour frequency ω_L, l_{sf}^N is the spin diffusion length of the Al channel, $\tau_{sf} = l_{sf(N)}^2/D_N$ is the spin relaxation time and D_N is the diffusion constant of aluminum. Then $R_N^{\omega} = R_N Re(l_{sf}^{\omega}/l_{sf}^N)$ is the spin resistance of the non-magnetic channel in presence of $H_{\perp}$, $R_{N(F)}$ are the spin resistances of Py and Al respectively, when $H_{\perp} = 0$, and R_b stands for the interface resistance, P_I and P_F are the interface and bulk spin polarization respectively.

The sample geometry is defined as follows: $L = 550\,nm$, $w_F = w_N = 50\,nm$, $t_N = 40\,nm$. At $77\,K$ the extracted resistivities are $\rho_{Py} = 119\,\Omega.nm$ and $\rho_{Al} = 15\,\Omega.nm$. The bulk polarization of the ferro-magnetic electrodes was taken to be $P_F = 0.77$ [14], the spin diffusion length of Py is $l_{sf}^{Py} = 5\,nm$ [68] and the diffusion constant for Al is $D_{Al} = 0.0043\,m^2/s$.

The fit results, as well as measured data-points, are displayed in the figure 5.4(c-d) for the two directions (X and Z). Note that these fits have been performed for two magnetization orientations, either parallel (blue) or anti-parallel (red). Results are displayed in figures 5.4(c-d), where the difference between the spin polarizations of the interface is explained by an undesirable electrical discharge, that occurred between the two measurements. Remarkably, the same l_{sf}^N value is obtained in both experiments.

5.3.3 Spin signals comparison

In order to compare the spin signals obtained with fields along the X, Y and Z directions of the magnetic field, another $Py/AlO_x/Al$ nano-structure with the same distance $L = 350\,nm$ was characterized. Figure 5.5(a-c) shows the results of non-local measurements for three directions of the external magnetic field. Data-points correspond to the green points, while the fits are represented by the blue and red curves for P and AP state respectively. The evaluated transport parameters are displayed in figure 5.5(b-c). Note that for all directions the spin signal amplitude of the order of $\Delta R_s = 14\,m\Omega$ remains unchanged. The l_{sf}^N value is in a good agreement with the value extracted from the gap dependence presented in *Chapter 3*. Nevertheless, the Al channel is thinner than in previous studies, and l_{sf}^N value is thus slightly decreased [36]. This is probably due to an increase of the surface scattering [32]. Interestingly, for the two in-plane and out-of plane spin precession the same parameters $l_{sf} = 450\,nm$ and $P_I = 0.073$ were extracted.

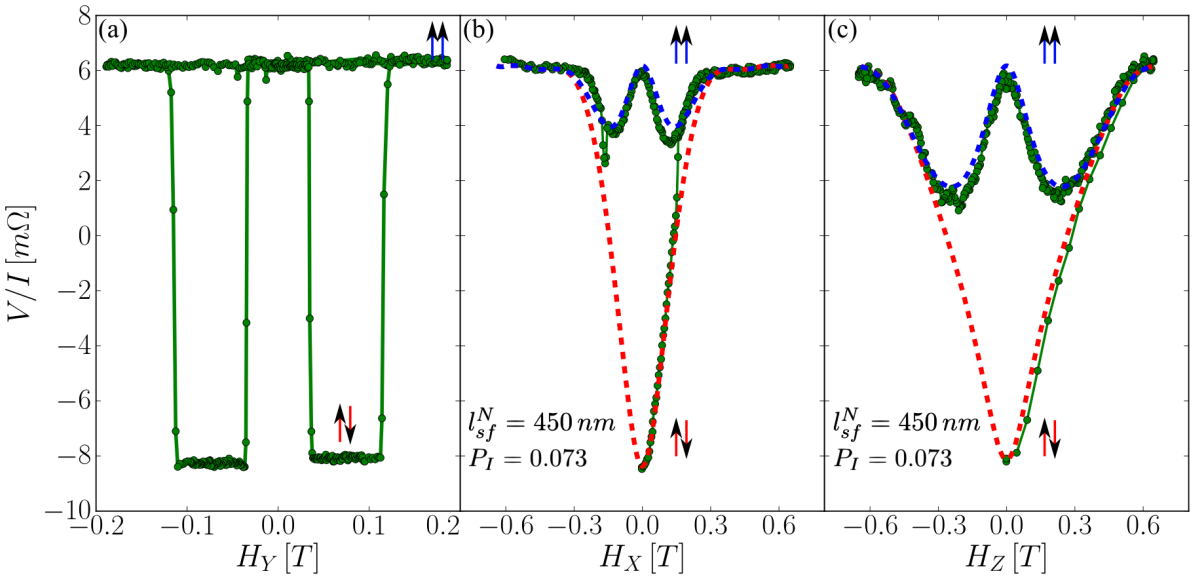

Figure 5.5: *Non-local measurements on LSV with $L = 350\,nm$: (a) typical measurements sweeping the external magnetic field along the F wires, (b) Hanle measurement with magnetic field swept along N channel (c) Hanle measurement with magnetic field swept out-of plane. Note that the spin signal amplitude remains unchanged and that the symbols ↑↑ and ↑↓ in (b) and (c) refer to the initial magnetic state.*

5.4 Conclusions

Amplification of the spin signal of the order of 500% was achieved using vertical confinement by AlO_x tunnel barriers, relatively to similar nano-structure with transparent interfaces. Spin signal amplitudes of $35\,m\Omega$ at $300\,K$ and $146\,m\Omega$ at $77\,K$ were recorded. Using this optimized nano-structure, the spin precession measurements were made by applying the external magnetic field in two directions (X and Z cf. *Fig. 5.5*). The fits of the Hanle effect with a spin precession model were carried out in order to extract the main material characteristic parameters (l_{sf}^N and P_I). This model was then improved by taking into account the magnetization variation at high magnetics fields. The fit results are in a very good agreement with the experimental data, showing thus the interest of this kind of technique for material characterization. Only one measurement is required for a complete analysis instead of multiple non-local ones for the gap dependence of the spin signal.

Moreover, Hanle measurements were performed for out-of plane and in-plane directions, leading to in-plane and out-of plane spin precession respectively. The latter geometry has never been reported. Taking advantages of a specific LSV geometry (narrow Py wires) we obtained similar results in this two directions. Comparison of the measurements for three directions of the magnetic field showed that the total amplitude of the spin signal remains unchanged whatever the direction of the applied field is.

Chapter 6

Spin Hall Effect

The spin Hall effect is a collection of phenomena resulting from spin-orbit coupling, in which an electrical current, flowing through a sample, can lead to spin transport in a perpendicular direction and to a spin accumulation at lateral boundaries. These effects, which do not require an applied magnetic field, nor a ferro magnetic material, can originate in a variety of intrinsic and extrinsic spin-orbit coupling mechanisms, and depend on the geometry, dimensions, impurity scattering and the band structure of the system, making of the analysis of these effects a diverse field of research. Many possible applications of this new spin current source would be forecasted, if a high yield of charge to spin current conversion could be achieved.

In this chapter the simple description of the spin Hall effect will be presented, underlying the importance of this effect. Some examples of applications will be presented within the description of the quest for new SHE materials with higher a spin-orbit interaction. Then the methods of characterization of the spin Hall effect will be described and used for the study of Pt and $Au_{1-x}W_x$ nano-wires ($x = [0.008 - 0.07]$). This will be done using spin pumping, and transport measurement in lateral nano-structures. At all stages, the finite Element Method simulations will be implemented in the analysis.

6.1 Spin Hall Effect

The SHE can be used to convert charge current into a pure spin current (a flow of spins with zero net charge flow) and vice versa. It originates from the spin-orbit interaction (SOI), which couples the spin of an electron to its orbital motion [24]. In a non-magnetic conductor, this interaction induces a pure spin current (opposite spin-up and spin-down currents) in the transverse direction to the flow of electrons and spin accumulations at the edges of the sample [cf. *Fig. 6.1(a)*]. This is the **Direct SHE** (**DSHE**). This spin accumulation can be then converted into a spin current, when the edges are connected to another material.

When considering a simple 2D model, where the charge current flows in the direction of the X axis of the non-magnetic materials with the SOI, the spin current along the Y axis is described as:

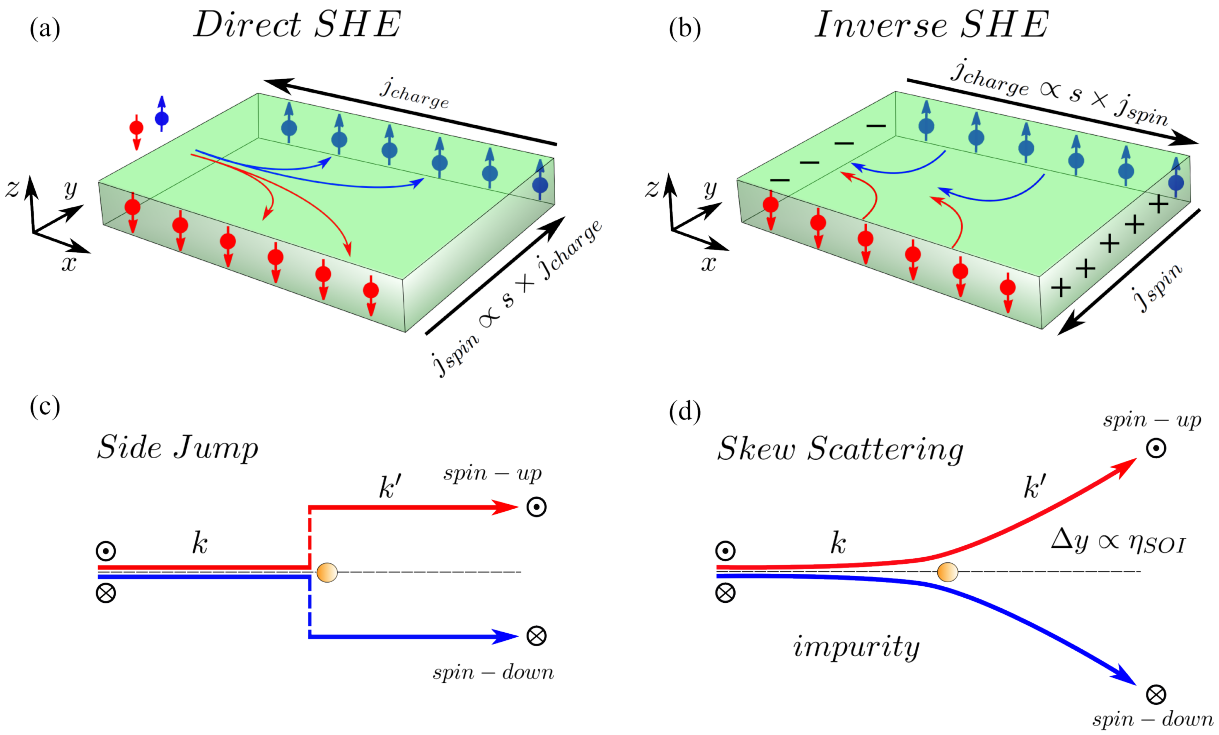

Figure 6.1: *(a) Direct SHE with the conversion of the charge to spin current according to the spin quantization axis z. (b) Reciprocal mechanism in Inverse SHE and conversion of spin to charge current according to the spin quantization axis s. Schematics of (c) the side jump and (d) the skew scattering microscopic origins of the SHE.*

$$j_y^{spin} = \frac{\sigma_{yy}}{2e}\frac{\partial}{\partial y}(\delta\mu_\uparrow - \delta\mu_\downarrow) + \frac{\sigma_{xy}}{\sigma_{xx}} j_x^{charge} \tag{6.1}$$

One can notice that beyond the part of the spin current, resulting from the spin accumulation ($\frac{\sigma_{yy}}{2e}\frac{\partial}{\partial y}(\delta\mu_\uparrow - \delta\mu_\downarrow)$), there is an additional transverse term due to the spin Hall effect ($\frac{\sigma_{xy}}{\sigma_{xx}} j_x^{charge}$).

The spin Hall effect is characterized by the ratio of the non-diagonal term of the resistivity tensor, ρ_{xy}, to the diagonal one ρ_{xx}, which is called the Spin Hall Angle (SHA) or the SHE angle:

$$\alpha_{SHE} = \frac{\rho_{xy}}{\rho_{xx}} \tag{6.2}$$

The spin Hall angle can be viewed as the conversion ratio of the charge current density into spin current density.

As shown in Fig. 6.1(b), there is also a reverse effect called **the Inverse SHE** (**ISHE**), in which a pure spin current can be converted into a charge current and into a charge accumulation by the reciprocal mechanism.

The possible origins of the SHE can be classified into two categories, **intrinsic** and **extrinsic**, depending on the predominant spin-orbit (SO) effects, either on the wave functions of the conduction band, or on the scattering potential of impurities or defects.

In the extrinsic SHE, the electrons are deflected by spin-orbit terms of the scattering potentials through the **skew scattering** and **side-jump mechanisms** 6.1(c-d). Those two extrinsic

microscopic origins of the SHE are also responsible for the anomalous Hall effect in ferromagnetic materials [125]. The resistivity ρ_{xy} of the SHE material is expected to vary as a function of the longitudinal resistivity, as follows [126]:

$$\rho_{xy} = a\rho_{xx} + b\rho_{xx}^2 \tag{6.3}$$

A linear variation indicates the skew scattering, while a quadratic behavior indicates the side jump contribution. The longitudinal resistivity can be changed by either temperature or the impurity concentration.

The skew scattering can be understood as a spin dependent asymmetric scattering probability of an electron on the impurity due to the effective spin-orbit coupling. As for the side jump mechanism, when the electron approaches an impurity, its velocity will be deflected in the transverse direction by the electric fields of the impurity (spin-up and spin-down electrons will experience different gradients of the electric field coming from the impurity).

On the other hand, **the intrinsic origin** is linked to the band structure, and the occurrence of band spin splitting by the spin orbit interaction at some high symmetry points near the Fermi level. Electrons experience an anomalous velocity perpendicular to the electric field, related to the Berry's phase curvature. It is worth noticing that the SHE is also expected to be strongly geometry dependent through the competing effects of spin accumulation and spin relaxation over the spin diffusion length, an essential scaling length for these phenomena.

6.2 Application

The spin Hall effect is an emerging route for spintronics, since it gives the possibility to generate and detect spin currents, crucial issues for future spintronics, without requirement for ferromagnetic materials and magnetic fields [cf. *Fig. 6.2*]. Due to this technological interest, the SHE has received a alot of attention and has been accompanied by an extensive theoretical debate [127].

Promising applications could be foreseen, if the yield of the conversion of charge into the spin current could be competitive to what can be obtained by using magnetic materials or F/N interfaces. Contrary to F/N interfaces, as a source of spin current, the spin accumulation and the spin current are produced in all the SHE material. This lowers the target conversion factor at which the SHE could be competitive to the conventional means. At the beginning of this thesis, the SHE had been studied only in pure metals or semiconductors, and even in these simple systems, its mechanism is still not clearly understood.

Fundamental questions about the origin of the spin Hall effect, which have been intensively debated in the last years, are currently being addressed with experiments. Measurements on such metals as Al, Au and Pt provide the opportunity to determine whether the mechanism, giving rise to the SHE, is the skew-scattering or the side jump. More recently, the use of this spin detection technique allowed the discovery of a new phenomenon, the spin Seebeck effect, where a spin voltage is generated from a temperature gradient in a metallic magnet [25]. The SHE was

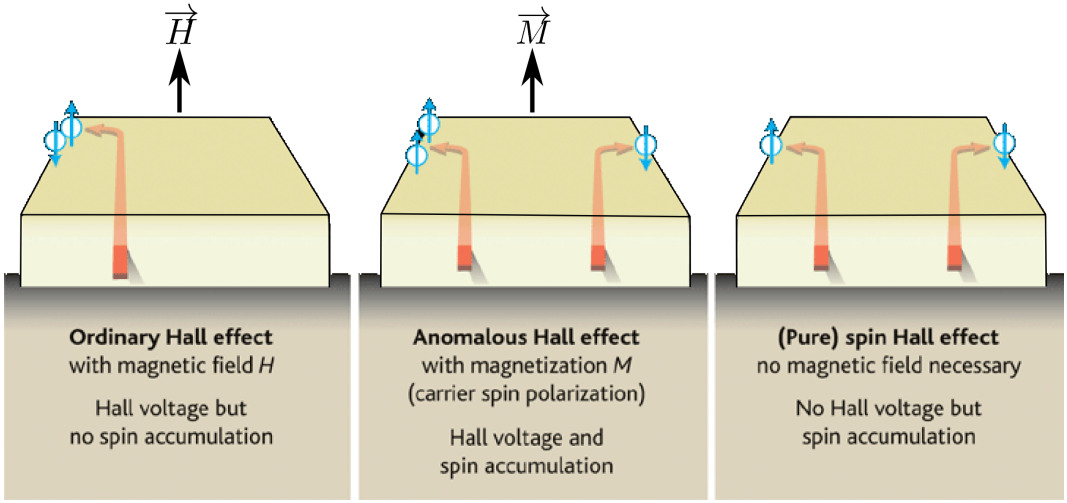

Figure 6.2: *Basic schematics for ordinary, anomalous and spin Hall effect. The spin Hall effect induces only spin accumulation without charge accumulation at the boundaries of the slab when a non polarized charge current flows into the material. Extracted from [128]*

very recently applied to experiments involving the spin-torque switching of ferro-magnets [29] or the spin-torque ferromagnetic resonance [30]. Also, spin current polarization control using the SHE and the stirring effect [129] and the spin Hall effect transistors, allowing detection directly along the gated semiconductor channel [31], were proposed.

The main challenges of today are: firstly a better understanding of the physics of the SHE, secondly, altogether with and beyond the situation of pure materials, the introduction of new concepts and materials that could lead to a large yield of the conversion from the charge to the spin current, and thirdly, development of the concept of new devices exploiting the specific advantage of the SHE for spintronics.

6.3 New materials

Up to now, the studies on the SHE have been focused on pure materials, semi-conductors or metals, with larger effects found in metals [32, 33]. Up to 2008 the largest value of the SHE angle α_{SHE} was for Pt ($< 10^{-2}$), and a surprising result was the announcement [37] of $\alpha_{SHE} \gg 0.11$ for Au, in which the SOI effects are expected to be much smaller than in Pt (there is no d character in Au). It was proposed that this large SHE could be due to an extrinsic contribution from Fe [130] or Pt impurities [131, 132]. Nevertheless, these results could never been reproduced and were subject to an intensive debate.

Fert *et al.* [34] showed almost 30 years ago that the resonant scattering of electrons on states of (heavy) non-magnetic impurities split by the spin-orbit interaction in copper can induce large SHEs, with Hall angles that can exceed 2.5×10^{-2} [cf. *Fig. 6.3*]. The experimental results were obtained in Cu doped with $5d$ impurities as Ta or Ir, having a strong spin-orbit splitting between the 3/2 and 5/2 $5d$ levels. In the absence of nanostructures for spin injection, the SHE of the non-magnetic alloys was revealed by spin-polarizing the current with very diluted Mn

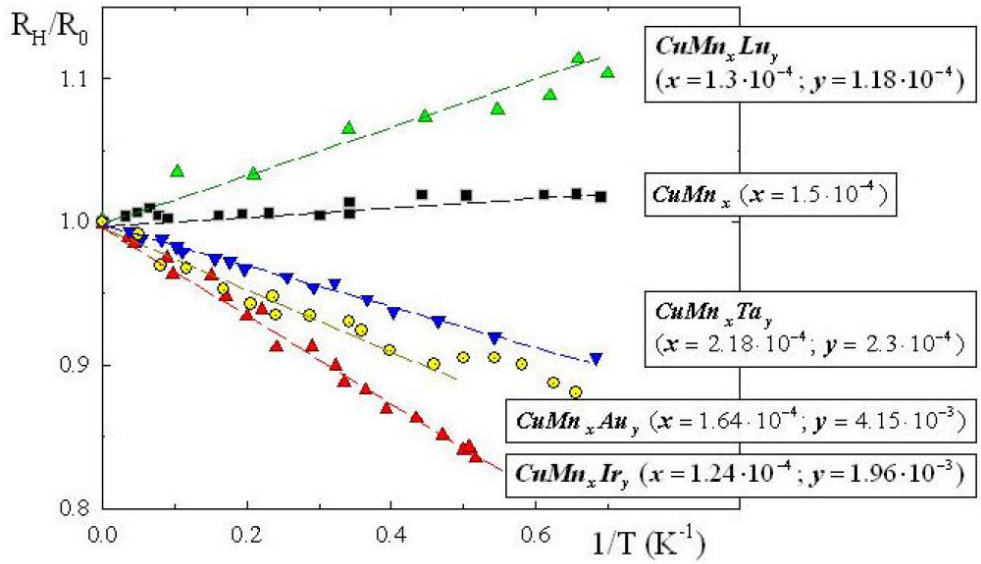

Figure 6.3: *Initial Hall coefficient versus* T^{-1} *for* $CuMn_xT_y$ *alloys (T=Lu, Ta, Au and Ir). The SHE of the CuIr, CuLu, CuTa and CuAu alloys induces a contribution to the Hall constant* $\propto T^{-1}$*, as the current spin polarization is proportional to the susceptibility of the paramagnetic Mn. The Hall angle for CuIr exceeds* 2.5%*. Note the change of sign between Lu and Ir. Extracted from [34].*

(0.05%) impurities polarized by a magnetic field (the Mn impurities themselves do not induce any significant Hall effect, as shown by the results with Mn only). These experiments were interpreted by the resonant skew scattering on $5d$ levels split by the SO.

Recently, experiments with nano-structures, where Cu based materials doped with Ir impurities were used, have shown that spin Hall angles of the order of $\alpha_{CuIr} \sim 2\%$ can be achieved, at $10\,K$ [35]. [1] In this study, the spin Hall angle was found to be invariant with the temperature and the impurity concentration, what indicates dominant skew scattering mechanism. The spin diffusion length for CuIr was estimated to be in the range of $5 - 12\,nm$, inversely proportional to the Ir concentration, where for pure Cu it was reported to be approximatively $l_{sf}^{Cu} \sim 1300\,nm$ [76].

Also, the estimation of the spin diffusion length, has been recently confirmed by *ab-initio* calculations [55]. Moreover, other alloys, with even shorter l_{sf}, were pointed out, as potential candidate materials for higher spin Hall angles. Figure 6.4, shows a summary of the results for Cu and Au based host materials. The ratio of the spin relaxation time versus the momentum relaxation time is displayed as a function of various impurities. These theoretical results show that, in respect to short l_{sf}, the SHE much larger than already observed, can be obtained by doping simple metals with impurities of large spin-orbit coupling. Nevertheless, the SHE will depend on the position of split level respect to E_F, to induce efficient resonant scattering.

Another ab-initio calculations [133] where performed for Au host materials revealing new

[1] Note that, for spin Hall angle calculation, the shunting effect [cf. *Section 6.5.3*], related with the current lines distribution (described in details further), was not fully taken into account.

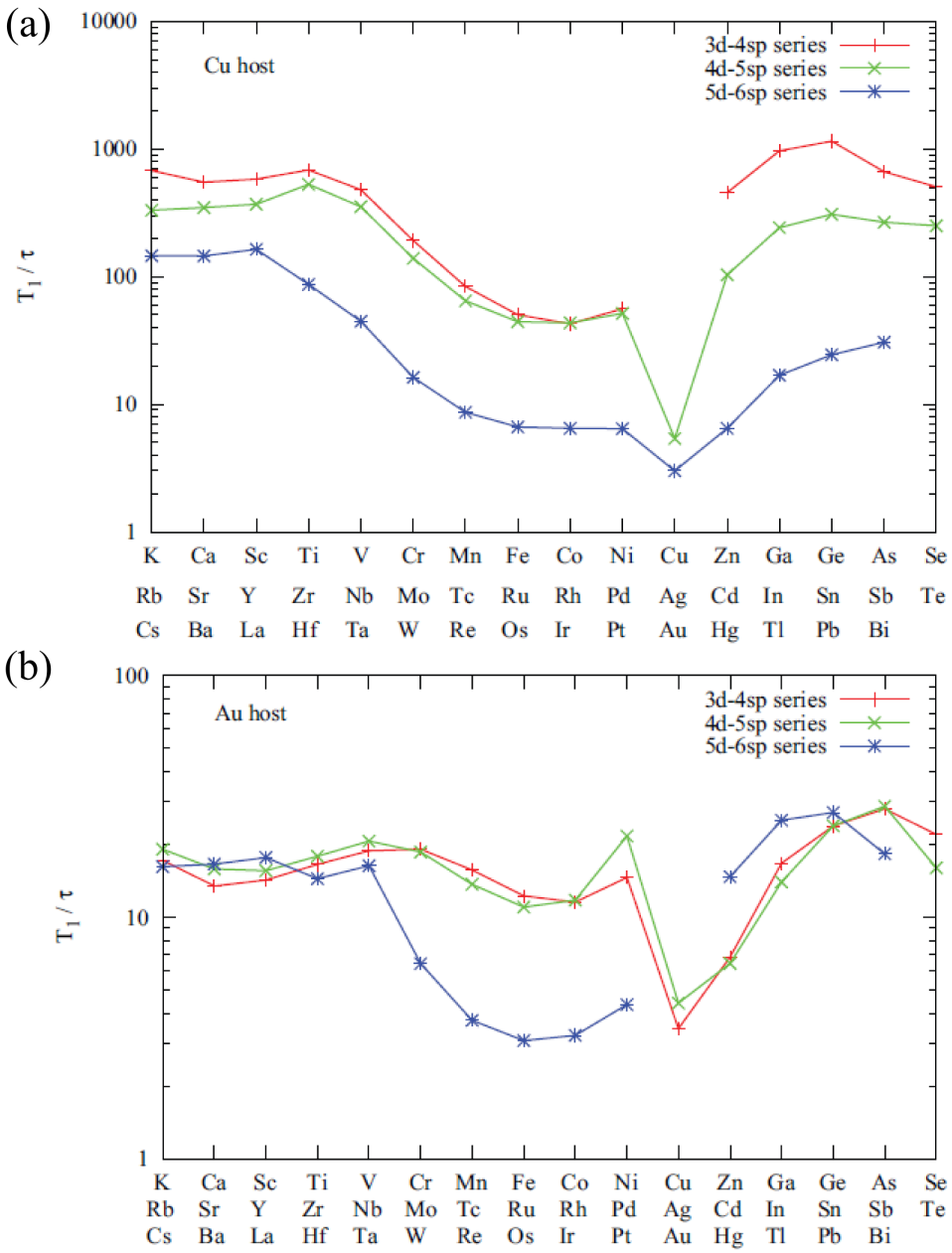

Figure 6.4: *Ratio of the spin relaxation time versus the momentum relaxation time T_1/τ for (a) Cu and (b) Au host. Extracted from [55].*

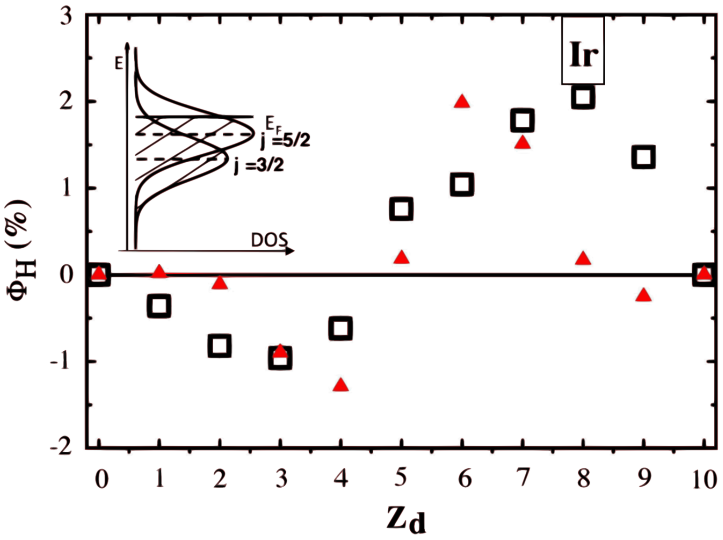

Figure 6.5: *Skew scattering (squares) and side-jump (triangles) contributions to the spin Hall angle as a function of the number of d electrons, Zd, for 5d impurities in Cu. Zd increases from 1 for Lu to 9 for Pt. The side-jump contribution is calculated for an impurity concentration of* 2%. *Inset: Density of states (DOS) of a 5d virtual bound state with S-O splitting between* $j = 3/2$ *and* $j = 5/2$ *states. Extracted from [56].*

candidate alloys exhibiting high spin Hall conductivity. The contribution of both extrinsic SHE mechanisms were compared. Also, the formulation describing analytically the side jump and the skew scattering contributions of Cu alloys was calculated as a function of number of the d electrons [56]. In these analyses the SHA changes sign, while filling the 5d level of the impurity, as shown in *Fig. 6.5*.

In the same context, in the frame of this thesis, new alloy materials were developed. They are based on the Au host doped with W impurities, in the range of concentration of $0.84 - 7\%$. The choice was guided by Prof. A. Fert, and C. Deranlot who developed and prepared the AuW alloys. The concentration of the W was determined by means of the Particle Induced X-ray Emission (PIXE). The resistivity induced by the W impurities $\rho_{AuW} - \rho_{Au}$ as a function of the W concentration in Au host, represented in figure 6.6, was found to increase linearly with the concentration. The base resistivity of pure Au material was estimated to be $\rho_{Au} = 35\,\Omega.nm$ at $300\,K$.

As presented in 6.4, for this alloy, one could expect the spin diffusion length to be $l_{sf} \leq 10\,nm$. Comparing to experimental results of CuIr [35], it is interesting to test even a higher spin-orbit interaction, and therefore a higher spin Hall angle, what could be indicated by a smaller spin diffusion length. Also, with materials like Au, problems related to oxidation, can be omitted, thus making easier the nano-fabrication processes.

One should also point out that the situation of resonant scattering on localized levels is not limited to impurities. Also, giant spin-orbit splittings have been recently found in interfaces states between Bi or Pb with Ag [134, 135], so that such interfaces or interface alloys are also promising candidates to obtain large SHE effects.

In the following, the evaluation of the SHE in AuW alloys with different W concentration will

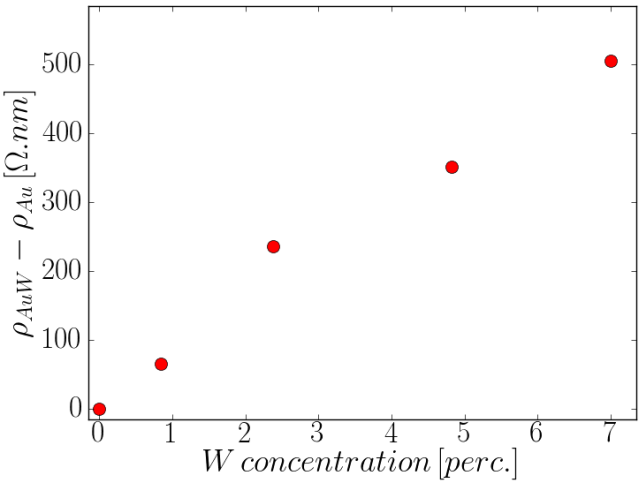

Figure 6.6: *The resistivity induced by the W impurities $\rho_{AuW} - \rho_{Au}$ as a function of W concentration in Au host, estimated for $T = 300\,K$.*

be presented in the actual state of the experiments. For calibration purposes, these experiments will be conducted, first, with Pt nano-wires. The results of the spin pumping experiments, providing a relatively fast method of Spin Hall angle estimation *via* the ISHE, will be shown for both materials. Then the transport measurements analysis will be performed.

6.3.1 Spin pumping experiments

The spin pumping experiments have recently attracted much attention, since they are now an alternative and fast way of the characterization of the spin Hall angle of a material *via* the inverse spin Hall effect [38, 39, 41, 40]. In this method, a ferro-magnetic/non-magnetic bilayer is used. Oscillations of the magnetization of the ferro-magnetic material are induces by the ferro-magnetic resonance, in the range of the GHz-frequencies. These oscillations are associated with a change of the longitudinal component of the magnetization that is transfered to the electronic bath. This creates a vertical spin current in the non-magnetic metal. The propagation of the spin currents within this material induces a detectable voltage, *via* the inverse spin Hall effect. A more detailed description of these experiments can be find in *Appendix C*.

Figure 6.7 represents the experimental results for Pt and $AuW_{7\%}$ bi-layers. Evaluated parameters are summarized in the following table, where red and blue colors stand for parallel and anti-parallel orientation of the field:

material	$V_{sym}\,[\mu V]$	$V_{assym}\,[\mu V]$	$V_{sym}\,[\mu V]$	$V_{assym}\,[\mu V]$	$V_{ISHE}\,[\mu V/G^2]$
	anti − parallel		*parallel*		
$Py(10\,nm)/Pt(20\,nm)$	50.5	−36.1	−52.5	35.4	30.7
$Py(10\,nm)/AuW_{7\%}(20\,nm)$	61.2	−93.5	−57.5	93.0	24.79

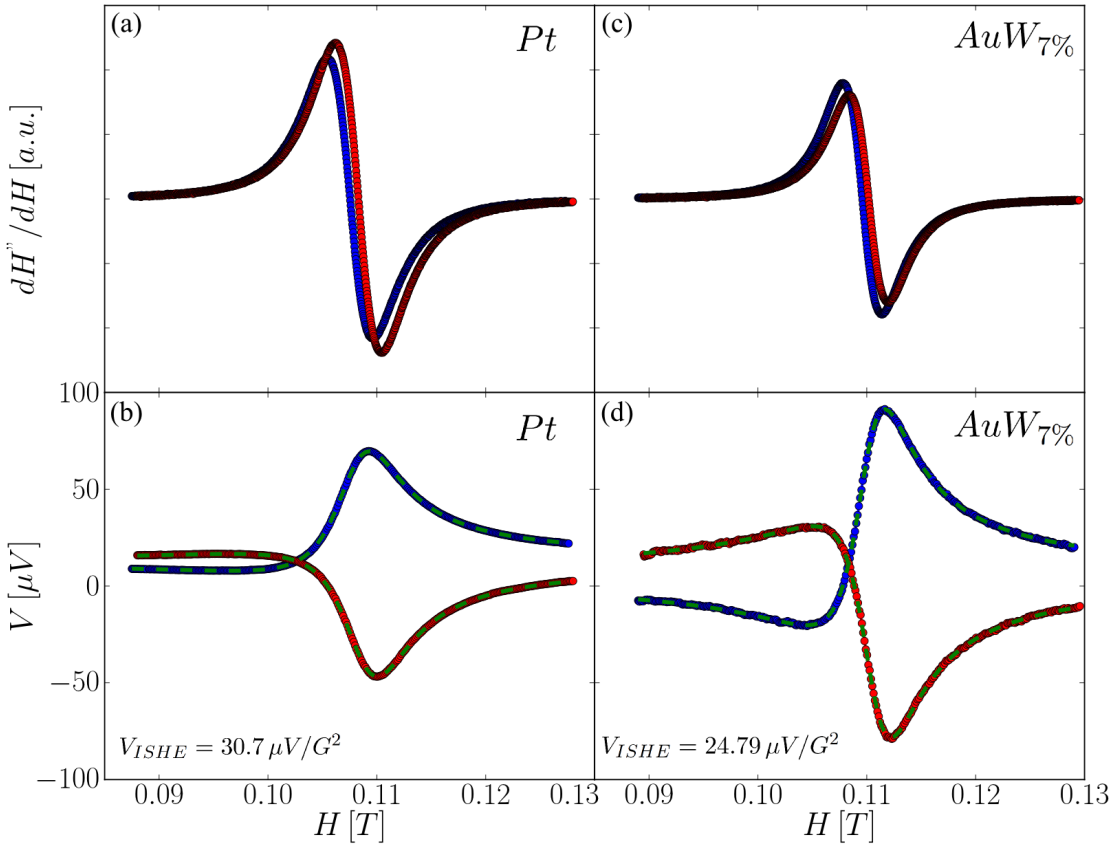

Figure 6.7: *Spin pumping results corresponding to the FMR spectra and voltage measured simultaneously for (a-b) Py/Pt, and (c-d) Py/$AuW_{7\%}$ bi-layers. The red and blue curves stands for the parallel and anti-parallel case, respectively. The green dashed curve represents the fits according to Eq. C.1. Insets displays the inverse spin Hall voltage V_{ISHE}.*

The symmetric and asymmetric voltages change signs with respect to the parallel and anti-parallel configuration, but similar absolute values have been found for both bi-layers. The deduced V_{ISHE} is smaller for $AuW_{7\%}$ than for Pt. Also, the sign of the V_{ISHE} is the same for both samples.

The spin diffusion length, necessary for the SHA estimation, can be only evaluated by the study of the thickness variation of the SHE material. However, this requires several samples preparation and becomes difficult for materials with very short spin diffusion lengths [44]. Complementary technique is thus required. Therefore, the spin Hall angle can be represented as a function of the spin diffusion length [cf. *Appendix A*], as showed in figure 6.8.

Despite a higher curve for Pt than for $AuW_{7\%}$, one needs to know their spin diffusion lengths before coming to a conclusion on their spin Hall angles.

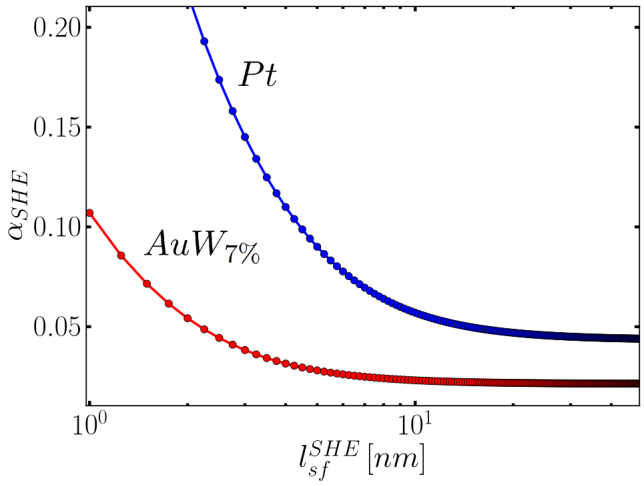

Figure 6.8: *Spin Hall angle α_{SHE} estimations as a function of the spin diffusion length l_{sf}^{SHE}, for Pt (blue) and $AuW_{7\%}$ (red) bi-layers, based on the spin pumping experiments.*

6.4 Spin diffusion length measurements

Another experimental technique, allowing the characterization of the spin Hall effect is the use of transport measurements in lateral spin-valves with the integrated SHE material. In this case, all parameters necessary for the SHA analysis can be extracted from a single sample-set. Moreover, the non-local spin current detection in the LSV without spurious current effects, has been proven to be well adapted for studies of spin related effects, what can be expected in SHE experiments.

The developed electrical detection scheme, proposed by Takahashi and Maekawa [71], was successfully applied to aluminum by Valenzuela *et al.* [36]. However, this method is not suitable for materials with a nanometer scale spin diffusion length, due to a strong spin-orbit interaction. Here, in order to determinate explicitly the spin Hall angles, a lateral spin-valve (LSV) with a SHE nano-wire insertion in between two ferro-magnetic electrodes is used (cf. *Fig. 6.9*), similarly to the geometry used by Vila *et al.* [33].

The patterning of very small LSV structures is important not only for the l_{sf} estimation but also for SHE studies. The SHE depends upon the balance between the spin accumulation induced by the SHE and the counterbalancing effect of spin relaxation that occurs at the scale of the spin diffusion length [33]. For a given current, the overall spin Hall effect is therefore reduced when the conduction channel size exceeds the spin diffusion length. A material with strong spin-orbit interaction, suitable for a large spin Hall effect, is also expected to have a short spin diffusion length measurements in materials with large SHE necessarily require structures of very small size, of the order of the spin diffusion length. By inserting the SHE wire in between the injector and detector of a LSV, the spin-to-charge conversion through the SHE takes place within the thickness of the SHE material, thus compatible with material with small l_{sf} and thin films.

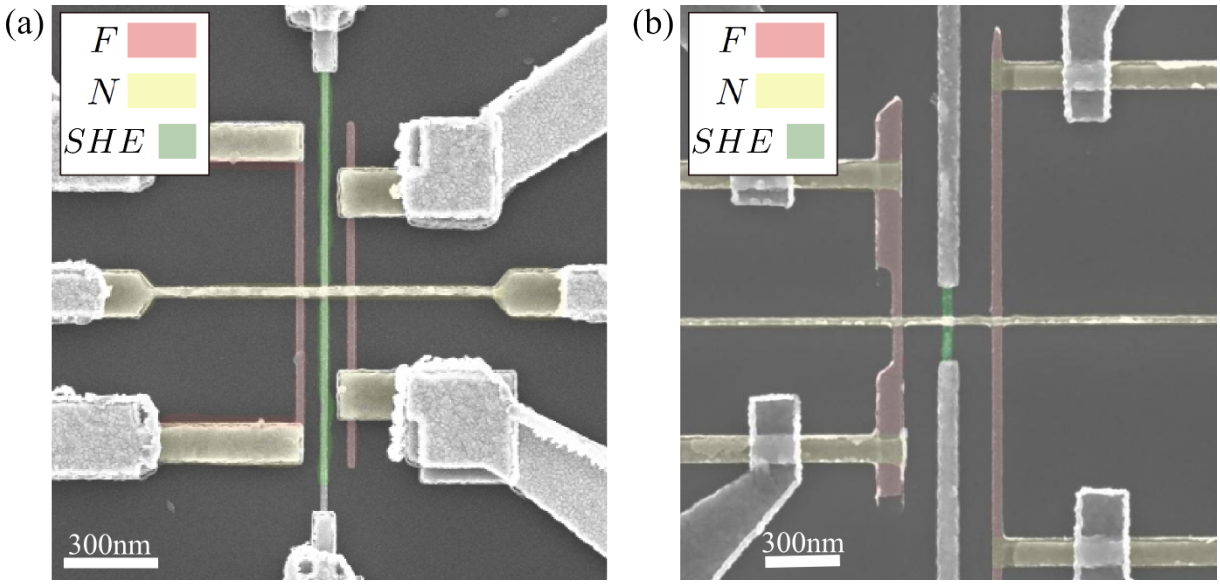

Figure 6.9: *SEM images of lateral spin-valve with the SHE nano-wire inserted in-between the two ferromagnetic wires, made by using (a) the multi-level nanofabrication, and (b) the multi-angle evaporation technique, where the SHE material was cleaned before the deposition of the active part of the LSV.*

6.4.1 Methods and devices

The insertion of the material for the SHE, shaped into a nanowire, in between the two ferromagnetic electrodes of a LSV allows the conversion of charge to spin currents within the thickness of the SHE material. With this approach materials with small spin diffusion length can be characterized [83]. Figure 6.9 represents SEM images of typical nano-devices fabricated using (a) the multi-level and (b) the multi-angle method. The red color stands for ferromagnetic, yellow for non-magnetic and green for the SHE material. First, the middle wire is deposited on the Si substrate, followed by the nano-fabrication of the standard spin-valve by one of the above-mentioned techniques (the multi-level or the multi-angle). In between these two steps, the middle wire surface is cleaned using ion-milling, similarly to the multi-level technique [cf. *Chapter 2*.

Non-local measurements are performed for two types of nano-structures: with and without middle wire inserted in between the ferro-magnetic electrodes. This is done in order to evaluate, using 1D models of spin diffusion, the spin resistance and then the spin diffusion length of the inserted material. These experiments are also known as the spin-sink effect, since spin currents, flowing in the non-magnetic channel, are partially absorbed by the central wire, and they have been used for estimation of the l_{sf} of various materials [83].

Figure 6.10(a-b) shows the Finite Element Method simulations (FEM) of the LSV geometry, with a nano-wire inserted in between two ferro-magnetic electrodes. The charge current represented by the arrows in Fig. 6.10(a) is injected through the right ferro-magnetic electrode (F) and drained-out on the right side of the non-magnetic channel (N). Thus the spin accumulation in N occurs, which is represented in Fig. 6.10(a). This spin accumulation is displayed using the iso-surface landscape (in the logarithmic scale). At the point of the current injection, the spin

accumulation reaches its maximum, decaying quasi-exponentially when propagating from the interface. Figure 6.10(b) shows the spin current distribution (in logarithmic scale), represented by the arrows, for the spin sink experiment. The spin accumulation is partially absorbed by the middle wire, which leads to a decrease of the spin signal amplitude in the Non-Local probe configuration, when measuring the voltage drop at the second (left) F/N interface.

These experiments allow the experimental evaluation of the spin diffusion length of the studied material. While the resistivity of the inserted material ρ_{SHE} can be directly measured (cross geometry nano-structure or 4 probes measurement), the spin diffusion length needs to be extracted from the absorption experiment by using 1D model. For the general case of the LSV, the ratio of the spin signal amplitude with the middle wire to the spin signal amplitude without this nano-wire, can be defined, as showed by Kimura *et al.* [83], by:

$$\eta = \frac{\Delta R_{with}}{\Delta R_{without}}$$

$$= \frac{R_{SHE}[\frac{R_F}{R_N}(2+\frac{R_F}{R_N})cosh(L/l_{sf}^N)+(2+2\frac{R_F}{R_N}+\frac{R_F^2}{R_N^2})sinh(L/l_{sf}^N)]}{R_N[-2(1+\frac{R_F}{R_N})+(2+\frac{R_F}{R_N}(1+\frac{R_{SHE}}{R_N})(2+\frac{R_F}{R_N}))cosh(L/l_{sf}^N)+(2\frac{R_{SHE}}{R_N}+\frac{R_F}{R_N}(1+\frac{R_{SHE}}{R_N})(2+\frac{R_F}{R_N}))sinh(L/l_{sf}^N)]} \tag{6.4}$$

Where the spin resistance of the inserted nano-wire is defined as:

$$R_{SHE} = \frac{\rho_{SHE}\, l_{sf}^{SHE}}{t_{SHE}\, w_{SHE} tanh(t_{SHE}/l_{sf}^{SHE})} \tag{6.5}$$

This allows the extraction of the l_{sf}^{SHE} of the nano-wire, since all other parameters are known (cf. *Chapter 3*). This method will be applied in the following to the Pt and to AuW nano-wires.

6.4.2 Spin diffusion length evaluation for Pt and AuW

Lateral Spin-Valves with the inserted **Pt nano-wire** were fabricated by using the multi-level approach [cf. *Fig. 6.9(a)*]. Table 6.1 summarizes the parameters of the lateral spin-valve. The resistivities and the material characteristic parameters $l_{sf}^{Cu} = 560\,nm$ and $P_{eff.} = 0.36$, have been estimated for $77\,K$. Note that all the geometrical parameters of the nano-structures, as well as the material characteristic parameters, were extracted using the methods presented in *Chapter 3*, and some reference samples were fabricated in the same batch (samples without the middle SHE wire).

material	*Py*	*Cu*	*Pt*
$w\,[nm]$	50	100	50
$t\,[nm]$	20	70	15
$\rho\,[\Omega.nm]$	118	25	138.5

Table 6.1: *Parameters describing the LSV with the inserted Pt nano-wire for* $T = 77\,K$.

Measurements of a clear spin signal, in the Non-Local configuration, were recorded at $77\,K$. Figure 6.11 shows the experimental curves, with (red) and without (blue) the inserted Pt nano-

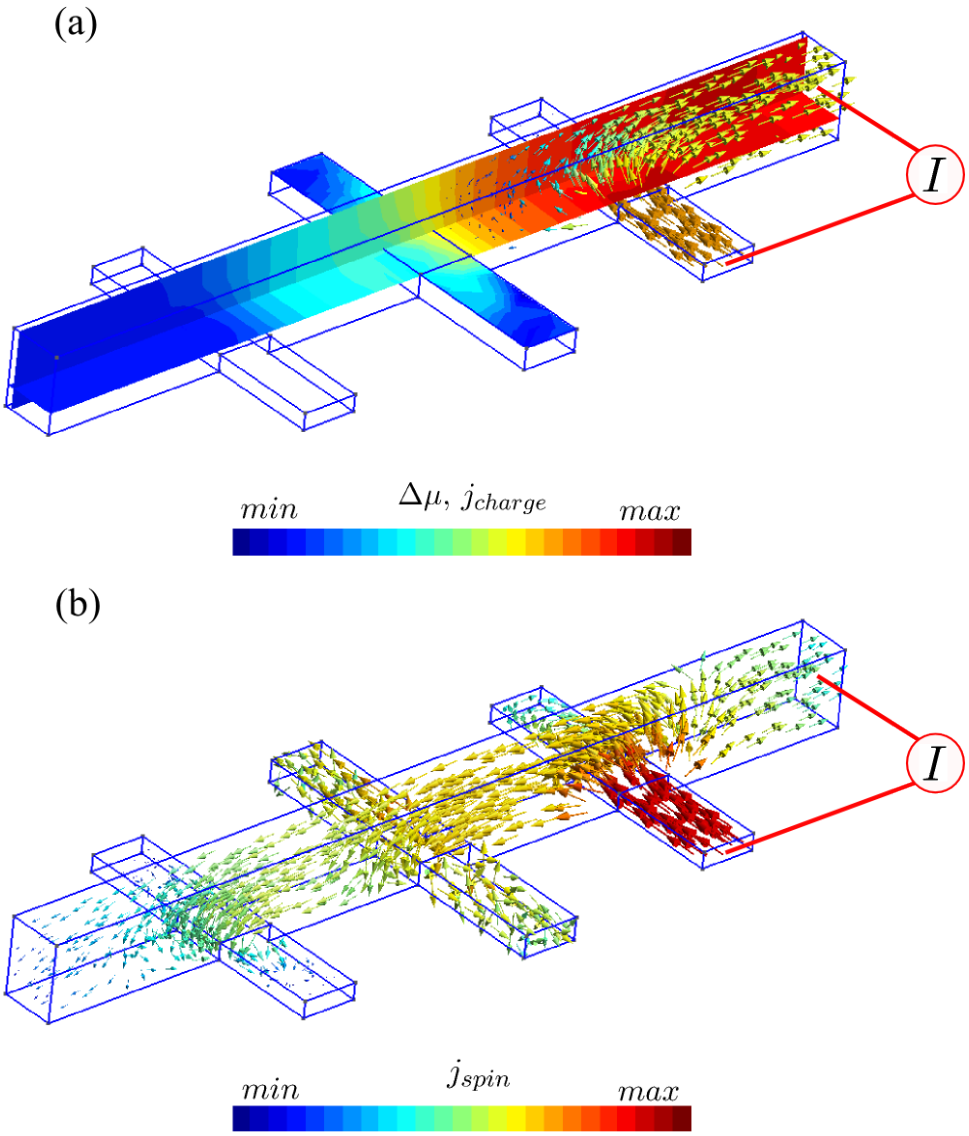

Figure 6.10: *FEM simulations of the LSV nano-structure with a nano-wire inserted in between two ferromagnetic electrodes. (a) The charge current is injected from the right side of the nano-structure and is represented by the arrows standing for the charge current density j_{charge}. The spin accumulation ($\Delta\mu$) distribution is displayed using iso-surface representation in the logarithmic scale. (b) Spin current distribution represented by the arrows (in the log scale) reflects the spin current density j_{spin}. One can notice that the spin current is absorbed (approximatively 50%) into the inserted nano-wire, leading to a decrease of the spin signal amplitude measured in the non-local spin-valve experiment.*

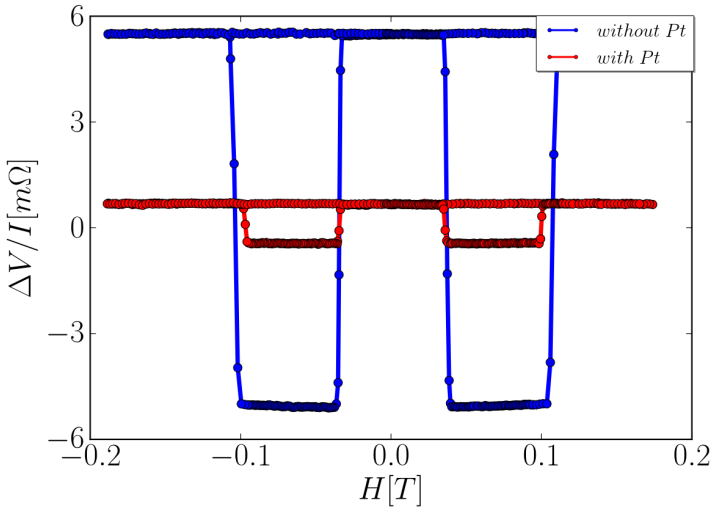

Figure 6.11: *V/I measurements recorded at 77 K for nano-structures (a) without ($\Delta R_{NL}^{without} = 10.63\,m\Omega$) and with ($\Delta R_{NL}^{with} = 1.2\,m\Omega$) the Pt nano-wire inserted between the two ferro-magnetic electrodes, distance $L = 400\,nm$.*

wire, evidencing the spin sink effect by Pt. Results of the analysis with the above-describes method, are summarized in the table:

material	$\Delta R_{with}\,[m\Omega]$	$\Delta R_{without}\,[m\Omega]$	η	*absorption*	$R_{Pt}\,[\Omega]$	$l_{sf}^{Pt}\,[nm]$
Pt	1.2	10.63	0.11	89%	0.12	4.5

The value of $l_{sf}^{Pt} = 4.5\,nm$ is found, which is in a good agreement with the review of the results on Pt [136].

Similar nano-structures, as in the case of Pt, were fabricated for **Au doped with** 0.84 % **of W**, using the multi-angle nano-fabrication method. In this approach, the AuW nano-wires were deposited using the sputtering method. The parameters of the nano-structures are summarized in the table:

material	*Py*	*Al*	$AuW_{0.84\%}$
$w\,[nm]$	50	50	50
$t\,[nm]$	15	60	20
$\rho\,[\Omega.nm]$	118	33	99.7

Here, the lateral nano-devices are characterized by $l_{sf}^{Al} = 548\,nm$ and $P_{eff} = 0.36$, for the temperature of $77\,K$. The clear spin signals were recorded for both nano-structures, with and without AuW nano-wire, at $77\,K$ [cf. *Figure 6.12*]. The distance separating the two ferro-magnetic electrodes for these devices is $L = 300\,nm$. A surprisingly high absorption of the spin signal was observed. The summary of the experimental data analysis is presented in the table:

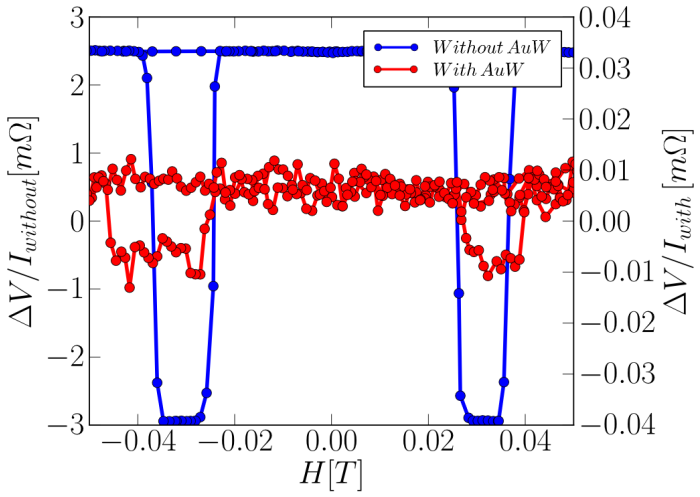

Figure 6.12: *V/I signal recorded at $T = 77K$ for Non-Local (NL) probe configuration: (a) with and (b) without AuW nano-wire inserted in between the ferromagnets (F). Part of the spin current is absorbed by the middle wire, causing a decrease of the spin signal amplitude in the NL configuration ($\Delta R^{without}_{AuW\,0.84\%} = 5.47\,m\Omega$ with and $\Delta R^{with}_{AuW\,0.84\%} = 0.02\,m\Omega$ with the inserted wire). Here separations are $L = 300\,nm$ and $L_{AuW} = 150\,nm$. When comparing both amplitudes one can find the higher absorption factor of almost 98%.*

material	$\Delta R_{with}\,[m\Omega]$	$\Delta R_{without}\,[m\Omega]$	η	*absorption*	$R_{Pt}\,[\Omega]$	$l^{Pt}_{sf}\,[nm]$
AuW 0.84%	0.02	5.47	0.037	98%	0.065	1.65

For the Au samples with higher W **concentration of** 4.82% the same geometry and the nano-fabrication method were used, as for the lower concentration. Summary of these parameters is presented in the table:

material	*Py*	*Al*	$AuW_{4.8\%}$
$w\,[nm]$	50	50	50
$t\,[nm]$	15	60	20
$\rho\,[\Omega.nm]$	118	32	386.1

Estimated characteristic spin transport parameters at $77\,K$ are $l^{Al}_{sf} = 560\,nm$, $P_{eff} = 0.36$. Figure 6.13 shows the spin signal amplitudes as a function of temperature, measured for the nano-devices with (red) and without (blue) the inserted middle nano-wires, for $L = 700\,nm$. The summary of the parameters used in the evaluation of $l^{AuW\,4.8\%}_{sf}$ is presented in the following table:

material	$\Delta R_{with}\,[m\Omega]$	$\Delta R_{without}\,[m\Omega]$	η	*absorption*	$R_{Pt}\,[\Omega]$	$l^{Pt}_{sf}\,[nm]$
AuW 4.8%	0.29	1.90	0.127	88%	0.522	3.38

Assuming that the absorption of the spin signal is constant with the concentration, as it was demonstrated for CuIr [35], and that the results for the higher concentration have more physical meaning that for the lower one, one could give another estimation of $l^{AuW\,0.84\%}_{sf}$. As

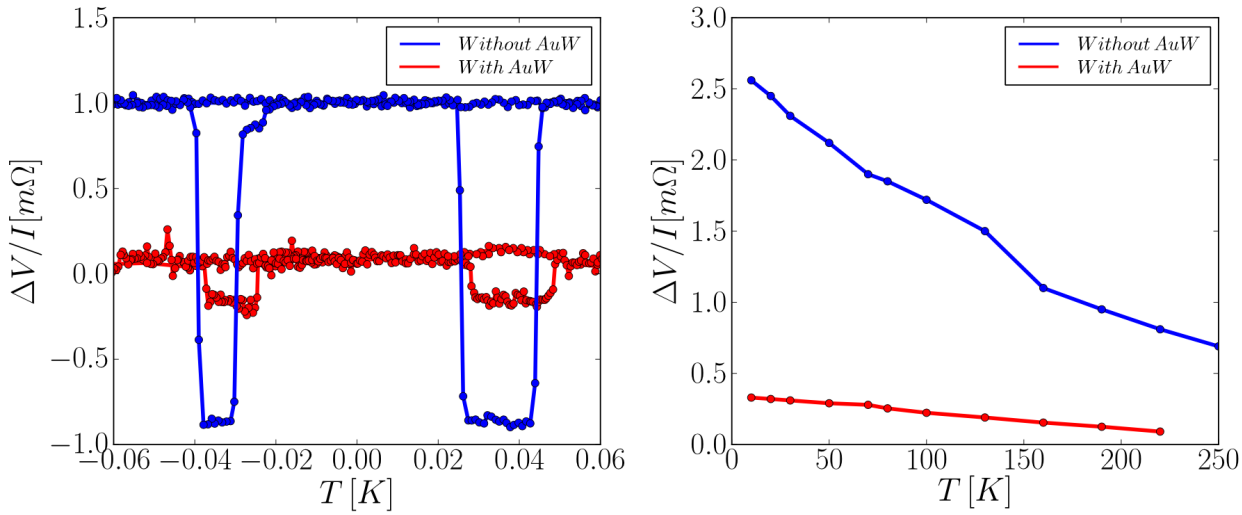

Figure 6.13: *(a) V/I measurements, recorded at $77\,K$, for $L = 700\,nm$. The red and blue curves stand for the nano-device with and without spin absorption by inserted AuW nano-wire, in between the ferro-magnetic electrodes, respectively. The spin signal amplitudes are found to be $\Delta R^{without}_{AuW\,4.82\%} = 1.90\,m\Omega$ without and $\Delta R^{with}_{AuW\,4.82\%} = 0.29\,m\Omega$ with wire insertion. (b) The spin signal amplitude variation, as a function of temperature for the nano-structure with (red) and without (blue) inserted AuW wire. Absorption does not change with temperature and can be described by the ratio $\eta = 0.127$.*

ρ_{SHE} and l^{SHE}_{sf} should evolve in opposite ways, the ρl_{sf} product can be supposed constant. In this case, the ratio $\eta = 0.127$ would give the spin resistance $R_{AuW\,0.84\%} = 0.255\,\Omega$, leading to $l^{AuW\,0.84\%}_{sf} = 6.37\,nm$, which has **more physical meaning** for such low W concentration. An unexpectedly high absorption value could come from a sample-to-sample variation or from a nano-device damaged during the experiment.

Table 6.2 summarizes the results of the spin diffusion length calculations for th above-presented materials.

	η	$\rho_{SHE}\,[\Omega.nm]$	$R_{SHE}\,[\Omega]$	l^{SHE}_{sf}
Pt	0.110	138.5	0.120	4.57
AuW 0.84%	0.036	99.7	0.065	1.67
	0.127		0.255	6.37
AuW 4.82%	0.127	386.1	0.522	3.38

Table 6.2: *Summary of the results of the spin diffusion length from the spin current absorption experiments.*

6.5 Spin Hall effect measurements

Several experimental schemes have been initially proposed for the electronic detection of the SHE [137, 138, 139, 140], including the use of ferro-magnetic electrodes to determine the spin accumulation at the edges of the sample. However, the difficulty of the sample fabrication and the

presence of spin related phenomena, such as Anisotropic Magneto-Resistance or the anomalous Hall effect in the F electrode, could mask or even mimic the SHE signal.

The experimental detection concept of the spin Hall effect was introduced by Hirsch[141], where the spin current is generated and detected *via* the SHE. This was almost 30 years after the original theoretical work from Dyakonov and Perel [24]. Zhang suggested that the edge spin accumulation produced by SHE could be detected electrically by using an attached ferromagnetic probe [142]. It took several years to demonstrate the viability of this method. Nevertheless, in a broader context, the idea of connecting SHE materials with ferromagnets for injection and detection of spins in non-magnetic systems has fueled numerous important studies of spin Hall devices.

6.5.1 Methods

In the direct spin Hall effect, by connecting the SHE material with the N material of the LSV [cf. *Fig. 6.14 (a)*], the out-of-equilibrium spin accumulation, induced by the SHE, is transferred from the SHE/N interface to the N/F interface by the flow of a spin current in the N material. In the inverse SHE, sketched in Figure 6.14 (b), the spin accumulation is created in the non-magnetic channel, using the F/N interface, and is further transfered to the N/SHE interface. Figure 6.14 (c-d) represents the electro-chemical potential landscape in the non-magnetic channel for (c) the direct SHE and (d) the inverse SHE. The blue and red curves stand for the majority and minority spin population respectively, while the green curve represents the average electro-chemical potential.

Since the longitudinal charge current J_c is converted into a transverse spin current J_s according to the direction $\overrightarrow{J_s} \propto \overrightarrow{S} \times \overrightarrow{J_c}$, for spin S (case of the DSHE), the external magnetic field is swept along the N channel. Then with the non-local resistance measurement we probe electrically the spin accumulation at the F/NM interface. The device geometry has been designed in the way to maximize the above-presented vectorial product (spins should be parallel to N) and thus the output signal.

In order to quantify the spin signals, coming from the SHE experiments, first, the amount of the spin current, absorbed by the inserted wire, is calculated by using the following equation [35, 143]:

$$\begin{aligned} \frac{I_s}{I_c} &= \frac{\int_0^{t_{SHE}} I_s(z)dz}{t_{SHE} I_c} = \frac{l_{sf}^{SHE}}{t_{SHE}} \frac{(1-exp(-t_{SHE}/l_{sf}^{SHE}))^2}{1-exp(-2t_{SHE}/l_{sf}^{SHE})} \frac{I_s(z=0)}{I_c} \\ &\approx \frac{l_{sf}^{SHE}}{t_{SHE}} \frac{(1-exp(-t_{SHE}/l_{sf}^{SHE}))^2}{1-exp(-2t_{SHE}/l_{sf}^{SHE})} \frac{2P_F R_F sinh(L/2l_{sf}^N)}{[R_N(cosh(L/l_{sf}^N)-1)+2R_F(exp(L/l_{sf}^N)-1)]+2R_{SHE}sinh(L/2l_{sf}^N)} \end{aligned} \tag{6.6}$$

Knowing this ratio one can calculate the SHE conductivity:

$$\sigma_{SHE} = w_{SHE}\sigma_{material}^2 (\frac{I_c}{I_s}) \Delta R_{SHE} \tag{6.7}$$

Finally, in order to calculate the spin Hall angle, we compare both the spin Hall (non-diagonal)

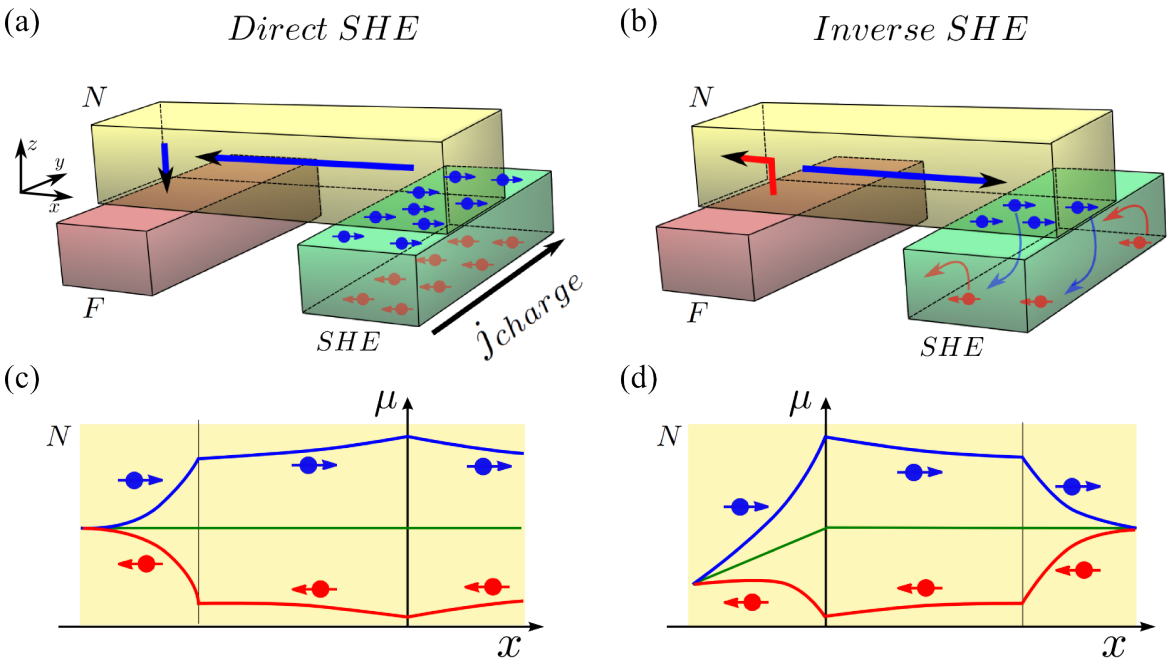

Figure 6.14: *(a-b) Schematic representation of the hybrid nano-structure with the ferromagnetic (red) and nonmagnetic-SHE (green) nanowires connected by a non-magnetic channel (yellow) with the macroscopic charge/spin current conversion details. (a) Direct SHE experiment with the charge current flowing in the SHE wire; the spin accumulation is electrically detected at the F/N interface. (b) Inverse SHE experiment: the spin current generated at the F/N interface is absorbed and converted to charge accumulation within the thickness of the SHE wire. (c-d) Electrochemical landscape for up and down spins induced by the SHE in the non-magnetic channel (N) for (c) direct SHE where the induced spin accumulation is transfered from the SHE/N interface to the F/N interface. (d) Inverse SHE with the induced spin accumulation, transfered from the F/N interface to the SHE/N interface. In all cases, the external magnetic field must be parallel to the N channel.*

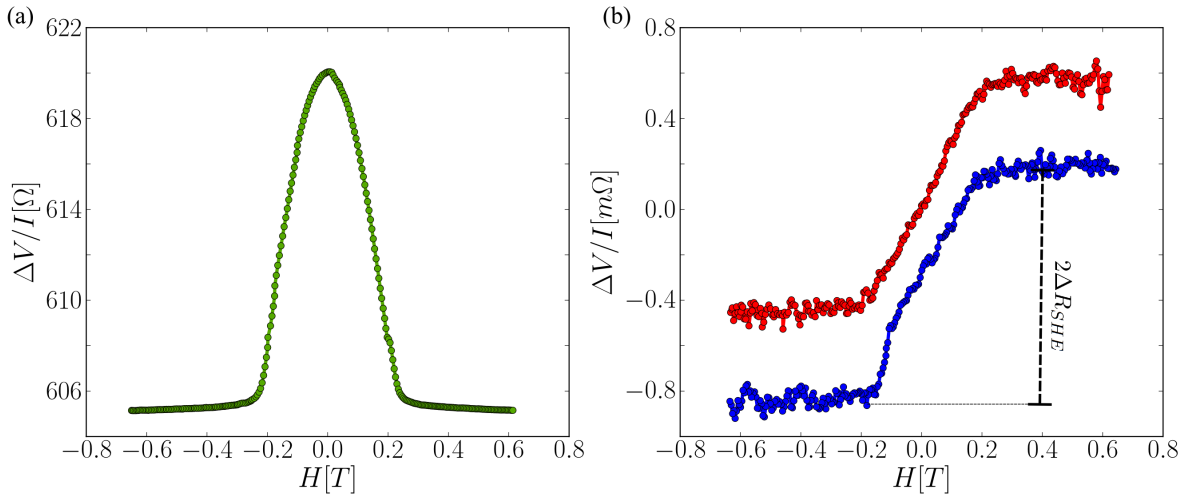

Figure 6.15: *(a) AMR measurements with the magnetic field applied along the non-magnetic channel. (b) Direct and Inverse SHE obtained with Pt nano-wire.*

and the inserted wire (diagonal) conductivities, as follows:

$$\alpha_{SHE} = \frac{\sigma_{SHE}}{\sigma_{material}} \tag{6.8}$$

To convert this ratio into terms of resistivities, one uses the following relation:

$$\rho_{SHE} = \frac{\sigma_{SHE}}{\sigma^2_{material}} \tag{6.9}$$

6.5.2 Results for Pt and AuW

In the following measurements, similar nano-structures were used as presented in *Section 6.4.2* with the nano-wire inserted in between the two ferro-magnetic electrodes. In these experiments the external magnetic field is applied along the non-magnetic channel. The spin signal exhibits a linear increase and gets saturated above the saturation field of the ferro-magnetic material F (acts as a spin injector in ISHE and as a spin detector in DSHE configurations), reflecting the hard axis. This is separately confirmed by the Anisotropic Magneto-Resistance measurement, as presented in Fig. 6.15(a), where the saturation fields are found to be $0.25\,T$. Clear spin signals were recorded at $77\,K$, for both the DSHE and ISHE configurations, with the spin Hall effect amplitude yielding $\Delta R^{Pt}_{SHE} = 0.55\,m\Omega$ [cf. F*ig. 6.15(b)*], for the inserted **Pt nano-wire**. This confirms the Onsager-Casimir reciprocal relations $\rho_{yx} = -\rho_{xy}$, stating that the amplitudes of the signals, recorded in both types of configurations are the same. This also highlights the reciprocal conversion of the spin to the charge and of the charge to the spin.

The amount of the spin current generated from the ferro-magnetic injector and absorbed by the inserted nano-wire, can be calculated by using equation 6.6. In the case of the nano-structures with inserted Pt wire, this ratio is found to be $I_s/I_c \simeq 20 \times 10^{-3}$, which leads to the spin Hall resistivity of $\rho_{SHE} \simeq 1.31\,\Omega.nm$. When knowing the resistivity of the Pt wire $\rho_{Pt} = 138.51\,\Omega.nm$,

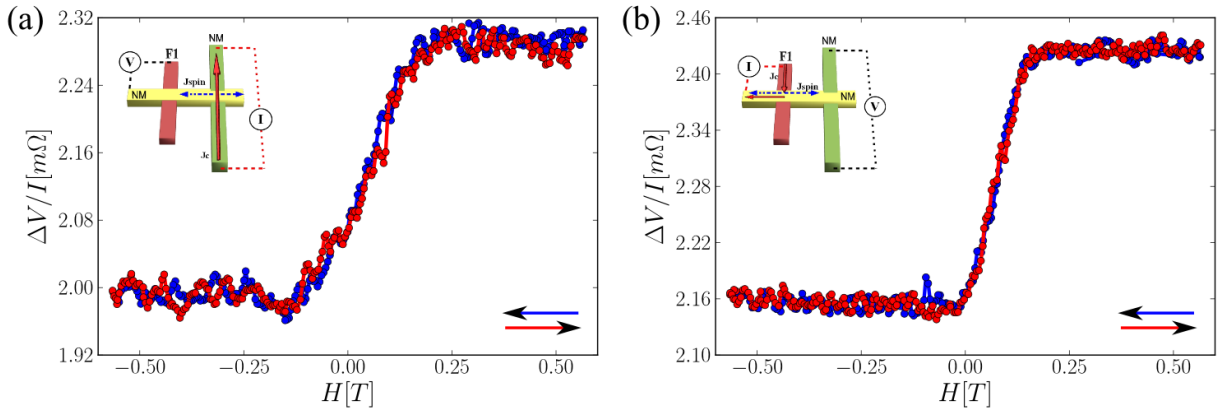

Figure 6.16: *Measurements of: (left) direct and (right) inverse SHE recorded at T=77K for* $L_{AuW} = 250nm$, $L = 500nm$.

the spin Hall angle can be estimated, by using equation 6.8, to be $\alpha_{Pt} \simeq 0.01$. This means that only 1% of the charge current is converted into the spin current.

When comparing these results with the literature, one can find similar values of the spin Hall angle coming from the transport measurements in similar LSV nano-structures. This is, however, not the case of the spin Hall angles estimated by the spin pumping experiments, where the SHA values are much higher. Table 6.3 summarizes the results of the spin Hall effect estimation in Platinum [136]. The difference can be explained by the so-called shunting effect, which will be described in the next section of this chapter.

In the case of the nano-structures with inserted AuW 0.84% nano-wires, the amplitude of the spin signal was found to be $\Delta R_{SHE}^{AuW\,0.84\%} = 0.15\,m\Omega$, for both the DSHE and ISHE configurations, with $L = 500\,nm$ [cf. *Fig. 6.16*]. Comparing to Pt nano-wires, the signal has **the same sign,** for the same probe configuration. This means that the SHA is positive.

The amount of the spin current absorbed by AuW nano-wire is found to be $I_s/I_c \simeq 4.35 \times 10^{-3}$. The spin Hall and the AuW nano-wire resistivities are $\rho_{SHE} \simeq 1.64\,\Omega.nm$ and $\rho_{AuW\,0.84\%} \simeq 99.8\,\Omega.nm$ respectively. This leads to a spin Hall angle of $\alpha_{AuW\,0.84\%} \simeq 0.017$.

When using values, calculated for the higher spin diffusion length, coming from the assumption of constant absorption (taken from higher AuW concentration) [cf. *Sec. 6.4.2*], one can find: $I_s/I_c \simeq 12.05 \times 10^{-3}$ and $\rho_{SHE} \simeq 0.57\,\Omega.nm$. This gives the spin Hall angle of $\alpha_{AuW\,0.84\%} \simeq 0.006$, what means that only 0.6% of the charge current could be converted into the spin current. In this case, the SHA is smaller than the one for Pt, what is consistent with the results from the spin pumping experiments, for such a low W concentration.

The charge current direction variation was also studied experimentally. In the ISHE configuration the spin signal changes the sign to the opposite one, as it can be seen in figure 6.17(a). This change does not influence the spin signal amplitude contrary to the variation of the angle with the magnetic field. When this angle is changed, from 0 degrees, which corresponds to the case of the magnetic field applied along the non-magnetic channel, to 90 degrees, where the

method	$\sigma_{SHE}[\hbar/2e](\Omega.m)^{-1}$	$\sigma_{Pt}[(\Omega.m)^{-1}]$	$l_{sf}^{Pt}[nm]$	α_{SHE}	$T[K]$	*ref.*
transport	2.4×10^4	6.4×10^6		0.0037	$300K$	[32]
transport	1.7×10^5	8.1×10^6		0.021	$10K$	[35]
FMR	5.1×10^5	6.4×10^6	7	0.08	$300K$	[144]
FMR	$> 2.4 \times 10^5$		1.4 ± 0.3	$> 0.05 \pm 0.007$	$300K$	[40]
FMR	$1.6 \times 10^4 \rightarrow 3.1 \times 10^4$	2.4×10^6	10	$0.0067 \rightarrow 0.013 \pm 0.002^{shunting}$	$300K$	[39, 42]
		24×10^6	14 ± 6		$4.2K$	[145]
FMR	9.7×10^4	2.42×10^6	3.7 ± 0.2	$0.08 \pm 0.01/2_{definition}$	$300K$	[26]
FMR	8×10^4	2.0×10^6	10	0.04	$300K$	[38]
FMR	$3.4 \pm 0.3 \times 10^5$	5×10^6	1.4 ± 0.3	0.068 ± 0.005	$300K$	[30]

Table 6.3: *Table summarizing the estimations of the Spin Hall angle for Pt.*

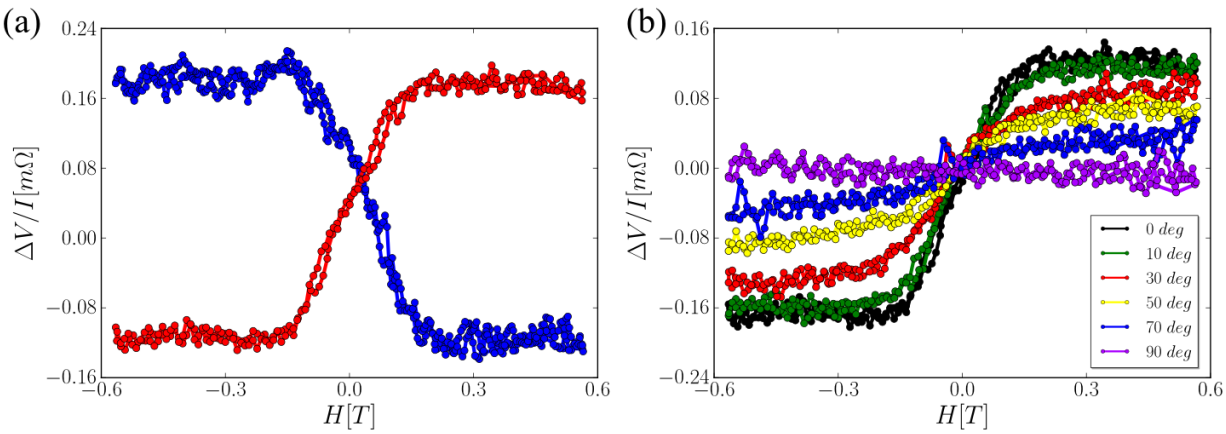

Figure 6.17: (a) *Current direction effect on ISHE measurements at T=77K. (b) Angular dependence of the ISHE. While changing the angle between AuW nano-wire and the external magnetic field the amplitude of the SHE changes, vanishing when the angle approaches 90 degrees.*

magnetic field is applied along the ferro-magnetic electrodes, the spin signal amplitude decreases down to zero. This is represented in the figure 6.17(b), and this reflects directly the quantity of spins injected into the non-magnetic channel, having their orientation aligned with the channel axis and this confirms the vectorial product $\overrightarrow{J_c} \propto \overrightarrow{s} \times \overrightarrow{J_s}$ relation.

Table 6.4 summarizes the results of the spin Hall angle estimation for Pt and AuW samples.

material	$\sigma_{SHE}\,[\Omega.nm]^{-1}$	$\rho_{SHE}\,[\Omega.nm]$	$\sigma_{material}\,[\Omega.nm]^{-1}$	$\rho_{material}\,[\Omega.nm]$	I_s/I_c	α
Pt	7633.6×10^{-4}	1.31	72.2×10^{-4}	138.5	20×10^{-3}	0.010
AuW 0.84%	6097.6×10^{-4}	1.64	100.2×10^{-4}	99.8	4.35×10^{-3}	0.017
	17543.9×10^{-4}	0.57	100.2×10^{-4}	99.8	12.05×10^{-3}	0.006

Table 6.4: *Summary of the parameters used for the spin Hall angle evaluation for Pt and AuW.*

In the above-presented method, the spin Hall angles are significantly reduced compared to those extracted by using the spin pumping method [136]. This problem was already pointed out by Motora *et al.* [143]. They suggested that this difference is related to the shunting effect and proposed an experimental device for the extraction of a correction factor, using 1D model.

In this thesis, the Finite Element Method simulations have been used for more exact estimation of the Spin Hall angles, since the shunting effect is naturally taken into account in the process.

6.5.3 Shunting effect

The shunting effect [cf. *Fig. 6.18*] is related to the current lines deviation at the interface of two materials, caused by the differences in their conductivities. Therefore, at the SHE/N interface, in the DSHE configuration, the charge current flowing through adjacent SHE material will preferably shunt through N. The spin accumulation created at the SHE/N interface is thus

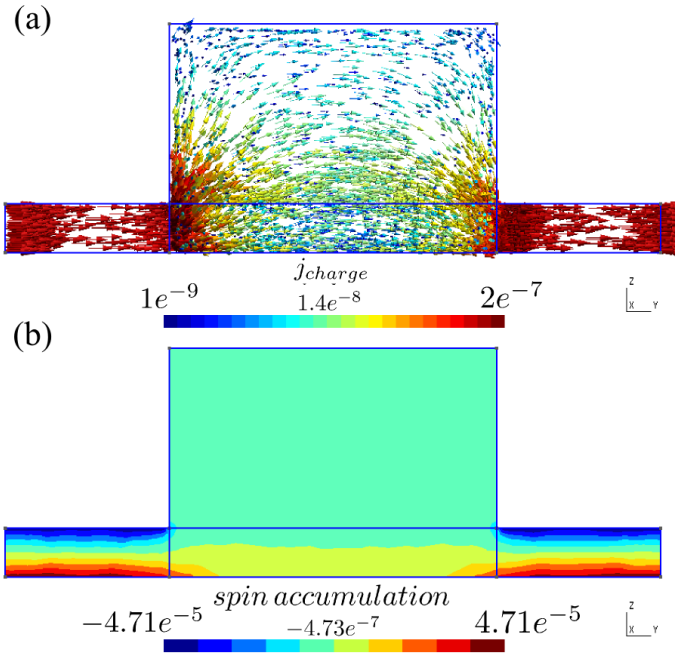

Figure 6.18: *FEM calculations of the shunting effect in LSV device with inserted Pt nano-wire. (a) Charge current distribution and (b) spin accumulation for Pt(bottom)/Cu(top) interface.*

smaller than the one at the surface of the SHE material. This leads to the under-estimation of the spin Hall angles, since the effective spin accumulation used for the charge/spin conversion is much smaller.

The Finite Element Method simulations can be carried out, in order to evaluate the real SHA of a given material inserted into a LSV nano-structure. The shunting effect in this kind of simulations is taken into account.

At the moment, the quantitative estimation is not yet conclusive, but basically a decrease of injection efficiency by a ratio of 10-15 is expected. In the limit case, where the current will be conducted in parallel, by the SHE and the N material, this ratio is $\frac{\rho_N t_{SHE}}{\rho_{SHE} t_N}$. For Pt and Cu, this ratio is calculated to be approximatively $\sim 1/20$, whereas for $AuW_{0.48\%}/Al$ it is only $\sim 1/9$.

6.6 Conclusions

The basic theory describing the spin Hall effect has been presented, as well as its possible applications. The main motivations in the quest of finding new candidate materials, exhibiting strong spin-orbit interaction, were described. Fabrication of lateral nano-structures with the inserted SHE materials was successfully achieved. Moreover, we showed that the spin current and the spin accumulation distributions can be calculated using the Finite Element Method for systems fabricated with the multi-level and the multi-angle approach. This provided a powerful tool for transport analyses in these systems.

Complementary methods used in order to evaluate the spin Hall effect were presented and applied for the case of Pt and AuW materials. Thus extracted spin diffusion lengths and the spin

Hall angles could be compared. For lower concentration of W in Au small l_{sf} values were found. Alternative estimations of the spin diffusion length for lower concentration in AuW samples, were given, assuming the constant independent on the concentration spin current absorption. This assumptions were based on recent experiments with CuIr alloys [35]. In this case, the spin diffusion length is found to be smaller for the higher concentration as one would expect.

The spin Hall angles extracted from the non-local SHE experiments exhibited the same sign for Pt and AuW. Also, the spin Hall angle estimation for Pt nano-wires was found to be in agreement with literature. For the case of low concentration AuW, the SHA was evaluated for both calculated spin diffusion lengths. A lower spin Hall angle was found compared to Pt for the case of longer spin diffusion length.

The complete analysis of the Spin Hall effect variation with concentration in AuW sample, was not yet possible in the actual state of the experiment, since its complexity requires more time. However, presented preliminary results give already very exciting perspective for the end of this thesis.

Summary and conclusions

A better understanding of the physical origins of the spin Hall effect, altogether with and beyond the situation of pure SHE materials, new concepts and materials are necessary for future development of a SHE based spintronics. In this context, this thesis describes a development of techniques, tools and analysis methods aimed at studying the spin Hall effect in diluted alloys. This work targets to address these fundamental questions experimentally. For this purpose, the electrical spin injection through the ferromagnetic/non-magnetic interface in the lateral spin-valves with an integrated SHE material, shaped into the nano-wire, has been developed and explored.

The major achievements of this work are as follows:

1. Technologies allowing the nano-fabrication of lateral spin-valves, based on NiFe ferromagnetic electrodes and Al, Cu or Au non-magnetic channel, have been successfully developed. A new technique of nano-fabrication using the multi-angle approach for ultra-clean F/N interfaces has been exploited, and the standard multi-level techniques have been optimized.

2. Electrical detection of the spin signals in non-local spin-valve measurements was achieved for Py/Al, Py/Cu and Py/Au nano-devices, proving state-of-the-art spin injection efficiency and very reliable spin current detection. Also, methods and tools allowing the parameter characterization of the samples were developed.

3. Two routes leading to the enhancement of the spin signal amplitudes in LSVs, were demonstrated experimentally and described theoretically, in the case of the lateral and vertical confinements.

4. Successful fabrication of hybrid lateral nano-devices, with insertion of SHE wires in between the two ferro-magnetic electrodes, was achieved with the multi-level and multi-angle methods, and for various materials (Al, Cu, Au, Pt).

5. Electrical detection of spin Hall effect in the lateral spin-valves and by spin pumping experiments has been achieved, together with the development of analysis methods and tools, and applied for Pt and Au doped with W impurities.

During this PhD thesis in experimental physics, I was also able to preform nano-fabrication, magneto-transport characterizations, and modeling in the field of spintronics.

I actively participated in the whole nano-fabrication procedures, looking for the reproducibility of the devices properties. This involves tests of different chemical approaches, insolation times, realignment methods, base-doses tests, resists tests, and this for various materials independently. In this context, I was formed to use various equipment, e-beam evaporator, ion-milling, optical lithography, SEM, AFM, EDX, including the JEOL 100keV e-beam nano-writer. Also, I became a member of the e-beam JEOL nano-writer user group of PTA, what allowed me to use the e-beam independently. I took advantage of my clean-room experience to fabricat samples for other studies not all mentioned in this manuscript (wires for study of the Magnon Magneto-Resistance, spin-torque study in LSV with Py rings, graphene-based and FePt/Al lateral spin-valves, injection of the spin current through a domain wall in LSVs)

Also, I participated to the development of two low-noise measurements setups dedicated to transport measurements, where one of them is equipped with a cryostat, allowing the study of temperature dependence. In this context, I fabricated measurement cables, connections, samples canes, samples holders, anti-vibration system; I made optimizations and all the software development. Moreover, using this characterization branches I performed the transport measurements and the data analysis for all samples.

My participation to the study of SHE in AuW alloys consists in fabrication of the lateral nano-structures and in the transport measurements. The alloys were developed and prepared by C. Deranlot at the Unite Mixte CNRS/Thales. In order to be consistent in these analyses, I presented also results obtained from the spin pumping technique. Although most experiments were performed and analyzed by Carlos Rojas-Sanchez in our laboratory, I provided complementary material parameters extracted by means of transport measurements, in parallel to these experiments.

The theoretical models presented in this thesis were taken from the literature or developed by collaborators (A. Fert, J.M, George, H.Jaffres) for the studied systems. My contribution was mainly related to the numerical and analytical application and to the use of the above-mentioned models. Moreover, I developed the measurement software together with data analysis and data treatment programs. This was made using different languages (Labview, Python or Java) and provided basic, flexible and fast tools. Also, I developed simulations using Finite Element Method (based on a code developed by A. Marty), allowing the study of the spin accumulation and the spin current distribution in the lateral nano-structures for various geometries.

Perspectives

The perspectives on this work can be categorized in three aspects related to technological development, and the study of LSV samples.

From the technological point of view, the developed nano-fabrication techniques and recipes valuable for various materials form a basis of knowledge for future experiments. The ultra-clean interfaces fabrication methods could be applied to experiments in which efficient spin injection and detection are required. This involves the spin-torque experiments to depin a domain wall or to switch the magnetization of a nano-particle. Also, low-noise transport measurement branches, developed during this thesis, brought important characterization tools for the laboratory, and proved to be useful for the study of spin-related phenomena. Further development can be foreseen with the goal of, for example, thermal spin injection and detection at higher frequencies.

Many interesting development and application can be based on the presented work with regards to lateral spin-valves, also with integrated additional nano-wires. First of all, this work is an experimental precursor in the view of studying new SHE materials based on diluted alloys. Along with summarized analysis methods and models, this work provides a basic startup for the future. Moreover, the usage of the SHE materials with high spin Hall angles, as a source of spin currents, can be imagined, allowing study or even later-on control of the domain wall pinning and depinning or switching of the magnetization. Presented methods of confinement of the spin accumulation in LSVs, either laterally or vertically, can lead to the increase of the amplitudes of measured signals in nowadays devices, and can be considered a guide for the experimental realization of optimum geometries and structures with various materials, including semiconductors and graphene.

As far as it concerns the development of simulations of the spin accumulation and spin currents distribution using the Finite Element Method, it gives a very important analysis tool. Importance of this kind of simulations was recently underlined, especially for study of spin Hall effect in lateral structures, by the shunting effect or more generally, when assumptions valid for the 1D approach do not hold anymore. This effect plays an important role in evaluation of the spin Hall angles, especially in the lateral nano-devices. Moreover, its open-source code can be easily adapted to various geometries and different problems.

Some of possible perspectives are already under investigation, for instance, some preliminary results on the switching of the magnetization or domain wall effects in the non-local geometries.

Appendix A

Simulations by Finite Element Method

These simulations are performed using two open source programs: GMSH [146], a three-dimensional finite element mesh generator, and GetDP the finite element method (FEM) solver [147, 148]. First, the 3D geometry of the system need to be defined, by indication of the points coordinates, interfaces, and physical volumes. Next the 1D, 2D and 3D mesh generation is done, with highly enough tetrahedrons density at the sharp angles. Then the basic core of the solver is defined, using weak form formulation of studied problem.

A.1 Methods

A collinear approach is used, which is equivalent for example to the case of two opposite magnetization orientations along a chosen axis. In this formulation we chose a current density j to represent a flow of spins, otherwise it would represents the electric density current, and the sign of above equations would have to be changed.

The FEM calculation are based upon the transport equations, where the current of carrier with up (down) spin is derived from the electro-chemical potentials $\mu_{\uparrow(\downarrow)}$, with different conductivities $\sigma_\uparrow$ and $\sigma_\downarrow$.

Then the current densities can be expressed in the following form

$$\begin{aligned} \overrightarrow{j_\uparrow} &= \sigma_\uparrow \overrightarrow{\nabla} u_\uparrow = \sigma \tfrac{1+P}{2} \overrightarrow{\nabla} u_\uparrow \\ \overrightarrow{j_\downarrow} &= \sigma_\downarrow \overrightarrow{\nabla} u_\downarrow = \sigma \tfrac{1-P}{2} \overrightarrow{\nabla} u_\downarrow \end{aligned} \tag{A.1}$$

where σ is defined as $\sigma = \sigma_\uparrow + \sigma_\downarrow$, representing the total conductivity, and P is the current polarization. The charge current conservation imposes that

$$div(\overrightarrow{j_\uparrow} + \overrightarrow{j_\downarrow}) = 0 \tag{A.2}$$

This charge conservation can be merged with a spin relaxation proportional to the spin accumulation in the following form:

$$div\left(\overrightarrow{j_\uparrow}\right) = -div\left(\overrightarrow{j_\downarrow}\right) = \alpha\left(u_\uparrow - u_\downarrow\right) = \frac{1-P^2}{4\rho l_{sf}^2}\left(u_\uparrow - u_\downarrow\right) \tag{A.3}$$

where $\rho = 1/\sigma = 1/(\sigma_\uparrow + \sigma_\downarrow)$ is the global resistivity and l_{sf} is the spin diffusion length.

By combining equations A.1 with A.3, one recovers the well known equation [13]:

$$\triangle(u_\uparrow - u_\downarrow) = \frac{u_\uparrow - u_\downarrow}{l_{sf}^2} \tag{A.4}$$

For transparent interfaces, the continuity conditions on the interfaces are imposed (continuity of the electro-chemical potential), together with the normal current densities on terminal faces (current source is set). This means that, when the current I is injected on a face of area A (total injected current must be 0). The material connected to the terminal is assumed to be long enough, to have vanishing spin accumulation on the terminal side. One thus assumes the same polarization on terminal faces, than in the bulk material:

$$j_{\uparrow surf} = \frac{1+P}{2}\frac{I}{A} \tag{A.5}$$

$$j_{\downarrow surf} = \frac{1-P}{2}\frac{I}{A} \tag{A.6}$$

In the case of a F/N interface, the electro-chemical potentials are discontinuous at the interface, and bi-valued on the surfaces. Therefore, one has to define different electro-chemical potentials for each simulated material. Moreover, the interface resistance need to be introduced in order to, express the interface current densities $j_{\uparrow surf}$ and $j_{\downarrow surf}$. In this approach the interface spin-flip effects are neglected. On one side of F/N interface, one can define the currents the flowing out of the side denoted (1):

$$\begin{aligned} j_{\uparrow surf}(1) &= \tfrac{u_\uparrow(1)-u_\uparrow(2)}{2R^* A_b(1-\gamma)} \\ j_{\downarrow surf}(1) &= \tfrac{u_\downarrow(1)-u_\downarrow(2)}{2R^* A_b(1+\gamma)} \end{aligned} \tag{A.7}$$

where $u_{\uparrow(\downarrow)}(1)$ and $u_{\uparrow(\downarrow)}(2)$ are the electro-chemical potentials on both sides of the interface. Since the two spin channels are independent, spins are conserved when crossing the interface : $j_{\uparrow(\downarrow)surf}(1) = -j_{\uparrow(\downarrow)surf}(2)$. By inverting sides (1) and (2) we see that this relation is consistent with Eq. A.7. Note that this formulation is valid in the case of the non-magnetic metal independently on the geometry. However, for the magnetic metal it is only valid when the surface on which the electro-chemical potential is probed, is much further from the interface, than the spin diffusion length of the material. On the other words, one supposes that at this point both electro-chemical potential, representing each spin populations are equal.

The spin dependent transport can be then defined in terms of the charge (j_c) and spin (j_s) currents, with the mean and the difference of the electro-chemical potential

$$\begin{aligned}\overrightarrow{j_c} &= \overrightarrow{j_\uparrow} + \overrightarrow{j_\downarrow} = \sigma\overrightarrow{\nabla}\left(\tfrac{u_\uparrow+u_\downarrow}{2}\right) + P\sigma\overrightarrow{\nabla}\left(\tfrac{u_\uparrow-u_\downarrow}{2}\right)\\ \overrightarrow{j_s} &= \overrightarrow{j_\uparrow} - \overrightarrow{j_\downarrow} = \sigma\overrightarrow{\nabla}\left(\tfrac{u_\uparrow+u_\downarrow}{2}\right) + P\sigma\overrightarrow{\nabla}\left(\tfrac{u_\uparrow+u_\downarrow}{2}\right)\end{aligned} \tag{A.8}$$

Appendix B

Nano-fabrication methods

The nano-fabrication process consists of five basic repetitive steps, represented in figure B.1.

First, a resist is deposited on the substrate surface. Different approaches can be used with single or multi-layered resit. Then using electron-beam lithography the desired pattern is exposed in the resist (step two). This shortens the molecular chains of the polymer, what allows the removal of the exposed parts by means of a chemical development. This process describes the step three in the case of the positive resist, like PMMA. In the following, the metallic material is evaporated on the sample, using e-beam evaporator. Note that two paths are indicated (with and without etching), since when connecting different materials ion-milling is required for surface cleaning in between. In the next step, the lift-off process is required to remove the remaining resist and the evaporated material deposited on top of it. What finally results in shaped nano-wires. These steps are repeated depending on how many different materials are required. Note that when using shadow or multi-angle evaporation techniques, several materials can be evaporated in the same cycle.

B.1 Procedures and equipment

The fabrication of the samples have been performed at the Plateforme Technologique Amont (PTA) in Grenoble.

The resist have been deposited on the Si or SiO2 substrate and spin-coated with either 2500 or 4000 rpm, with acceleration of 2000 rpm/s^2. This was followed by samples baking in order to remove the solvent. The baking times depends on used resist. For most commonly used PMMA, samples were baked at 180 degrees Celsius around 5 minutes.

B.1.1 Electron-beam lithography

The electron-beam lithography has been made using Jeol 6300FS e-beam nano-writer, working at acceleration voltage of $100\,keV$. Two modes were exploited using: high speed, EOS3 (4th lens, with beam step size of $1\,nm$ and field size of $500\,\mu m$) and high resolution EOS6 (5th lens, with beam step size of $0.125\,nm$ and field size of $62.5\,\mu m$). Different current values were used depending of the pattern surface: 1, 5, 30, $60\,nA$. Where the lowest current were used

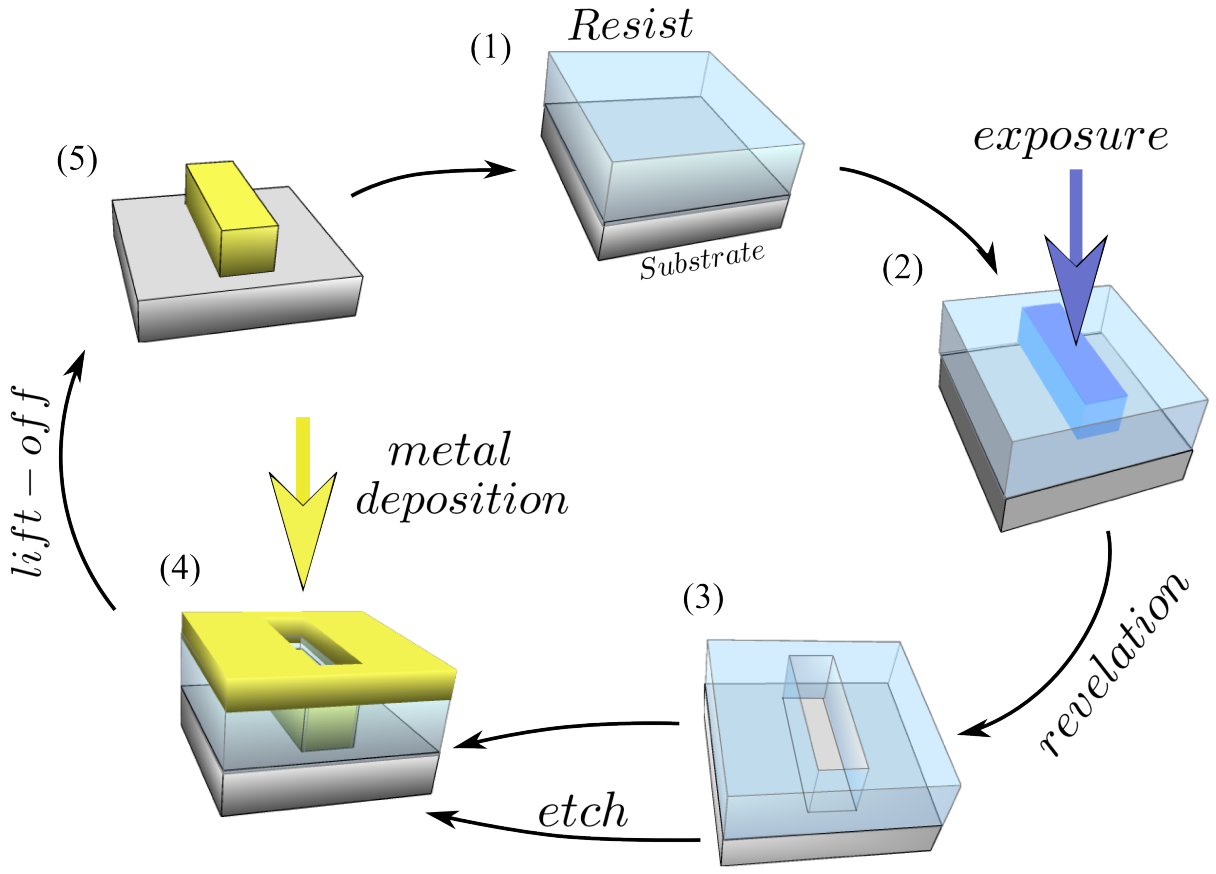

Figure B.1: *Schematic representation of the nano-fabrication procedure cycle, consisting of (1) resist deposition on the Si substrate. (2) e-beam lithography exposure of the desired pattern, (3) revelation of the resist, (4) material evaporation, and (5) the lift-off process.*

for high resolution (nano-wires exposure), while the highest one for microscopic electrodes or realignment marks. This out-of standard usage, current values, overcoming $20\,nA$, were employed in order to decrease the patterning time of the electrodes and the realignment marks. This gave reproducible results with good realignment of the patterns. Afterwards, this process was replaced by patterning the electrodes and marks by means of the optical lithography (UV and DUV), with the resolution of $1\,\mu m$, as good overlay alignment could nevertheless be obtained.

Basic calibration of the machine consists of the alignment of the column, similarly to the scanning electron microscope. In this step, the electron beam has been aligned along the column axis (aperture and optical lenses). Then two internal electron marks have been used for calibration of the beam deflection and focus. The marks are placed on the sample holder, which is moved for the calibration of the deflection, within the exposition field range, while the position of the holder being controlled precisely by laser interferometry. The deflection is calibrated this way, with typical error $<4\,nm/250\,\mu m$

The pattern design were made using *Klayout* software [149] in the form of *GDSII* file, further converted into Jeol proprietary format. Shot modulation by data-type number has been used allowing fine control of the dose. The base dose value depending on used type of the resist and the revelation method, were evaluated for each component of the pattern separately. We have used single resist approach for the multi-angle technique and also bi-resist approaches were developed for lift-off of sputtering deposition. In the latter one, the designed pattern was surrounded by the additional exposition area irradiated at lower dose. This allowed creation of the undercuts in the more sensitive bottom resist layer, allowing lift-of process of the sputtered materials.

The realignment marks, which includes the global marks and the chip marks, were patterned either by means of optical or e-beam lithography. Both were made of $80-100\,nm$ thick gold. Four global marks were used, placed at the extremity of samples array. These cross shaped structures are $3\,\mu m$ wide and $1000\,\mu m$ long. They allow the change from the e-beam referencing axis to the one of the sample (shift, and angle correction). For each device three L shaped, $3\,\mu m$ wide and $25\,\mu m$ long, chip marks were used for fine shift correction.

B.1.2 Resist revelation

- **Standard revelation procedure** consists in usage of $MIBK:IPA(1:3)$ resist developer. Usual times depends on used geometry, for nano-wires of $w=50\,nm$, usual time of $30-35\,s$ was used. For larger geometries, like electrodes or realignment marks, this time was longer, reaching $40-45\,s$. Afterwards samples was put into iso-propanol.

- **Jeol development procedure** consists in usage of, first $MIBK:IPA(1:1)$ developer during $60\,s$, then $MIBK:IPA(89:11)$ during $15\,s$. At the end, the sample is put into iso-propanol. This technique allows usage of much smaller exposure doses of about 1/5 of the standard ones used with standard development techniques. Nevertheless, the PMMA appeared to be more sensitive to ion-milling with this process.

B.1.3 Metal evaporation

Metal evaporation have been made using e-beam evaporator, equipped with 8 targets, the ion-milling and oxidation line. Deposition rate has been controlled using the quartz oscillator within the range of $0.1 - 1\,nm/s$. The base pressure in the deposition chamber was around $1 - 2 \times 10^{-8}\,mbar$.

Targeted techniques required advanced usage of the machine, and allowed the development of the multi-angle evaporation in a full automatic mode. Instead of using planetary stage rotation, we used negatives and positives angles of the stage inclination, what allowed automatization of the processes. This aspect is important in this technique since double side evaporation was necessary in order to avoid formation of the nano-gaps.

B.1.3.1 Ion-milling

The Ar plasma etching have been used with the acceleration voltages in the range of $250 - 600V$. Position of the sample on the stage was optimized and fixed, in order to achieve reproductive results and constant etch rate. Rotation of the stage was used to precisely control the sample position for etching or evaporation.

In the multi-angle method etching was performed with the 20 degrees angle to the samples plane (imposed by the machine construction), along the non-magnetic channel. Otherwise, in the multi-level approach an angle adapter has been used allowing etching perpendicular to the samples plane.

B.1.3.2 The hard mask approach

In order to evaluate procedure allowing precise control of the etch time the Energy Dispersive X-ray spectroscopy has been used. In this approach the hard masks protections have been deposited in the nano-structures, typically Al, thus allowing to establish the same ion-milling rates. This technique was useful for the nano-structures dedicated for SHE experiments, as for example for Pt nano-wires etch rated are significantly higher than for Al.

Figure B.2 represents the EDX spectra of a $Ni\,(5\,nm)/Au\,(10\,nm)/Al\,(10\,nm)$ multilayer deposited on the SiO_2 substrate. Mentioned layers were deposited in presented order (starting with Ni). This structure was realized so as to calibrate the ion-mealing time of Al capping layer deposited on top of Au layer. The evolution of the Al peak (corresponding to the energy of $1.5\,keV$), as a function of etch time, is represented in the inset of the figure, where the blue line is a reference measurement performed before and red curve after etch. One can notice that the number of counts for the Al peak decreases with increasing etching time, thus allowing extraction of average time needed for a complete removal of the capping layer. For this structure, time needed to remove the Al hard mask by ion-milling with voltage acceleration of $250V$ is approximatively equal to $125\,s$.

Note that usually for quantitative analysis of the elements higher voltage are used (typically $10\,keV$) in order to obtain well separated K peaks for each elements without any overlaps. However, built-in analysis methods within the machine allow to subtract the background and

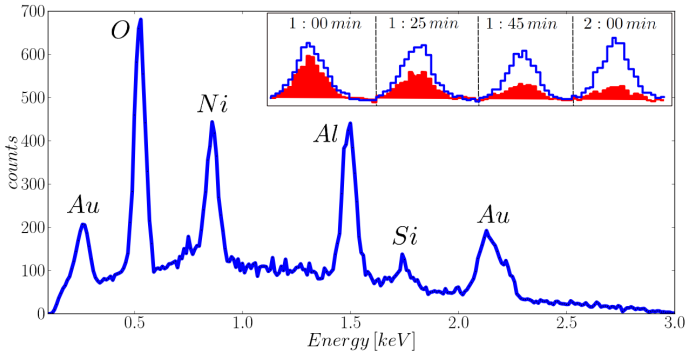

Figure B.2: *The energy dispersive X-ray spectroscopy (EDX) spectra of the Si/Ni/Au/Al multi-layer elaborated for the ion-milling time calibration of a capping Al layer. Counts variation as a function of the etch time is represented in the inset, where blue curve stands for the reference measurement performed before each etch and the red curve for the one made after etching.*

perform lower energy spectra analysis. In above mentioned studies we used energy down to $3\,keV$ where the probing depth is limited in this case to $30 - 50\,nm$, making this configuration very sensible to the surface of the nano-structure.

B.1.4 Lift-off process

The lift-off process has been realized in two approaches. In the first one (longer), sample is put into the cold acetone, on ellipsoidal glass with the "face-down" and left over the night. In the second one, acetone is heated up to 50 degrees Celsius what allows fast lift-off process (around 20 minutes), where sample is put "face-up". For both cases, the ultra-sound are applied afterwards.

B.1.5 Recipes

The most used recipes for the nano-fabrication can be classified in the following table B.1:

resist	$PMMA\,2\%$	$PMMA\,4\%$	$PMMA\,2/4\%(2:1)$	$PMMA\,2/4\%(3:1)$	$PMMA\,4\%/MMA$	$ZEP520A$
spin coating $[rpm/min.]$	4000	4000(2500)	2500	2500	4000	4000
resist heigh $[nm]$		280(320)	120	150	370	120
etch rate $[nm/min.]$	40 (600V)	40 (250V)				
		$45-50$ (400V)	$50-55$ (400V)			
		8 (600V, *rotation*)	$60-70$ (250V)			
dose $[\mu C.cm^{-2}]$	1400	410	410	1500	420	$800-1000$
motif	*nano − wires*	*nano − wires*	*nano − wires*		*electrodes*	*electrodes*
revelation	*standard*	*Jeol standard*	*Jeol standard*	*Jeol*	*Jeol*	

Table B.1: *Summary of the test results of various resists.*

Appendix C

Spin Pumping methods

The used bilayers geometry corresponds to Py width of $w_F = 1.5\,mm$, and the thicknesses $t_F = 10\,nm$ and $t_N = 20\,nm$. We measure simultaneously the Ferro-magnetic resonance (FMR) spectra and the transverse voltage generated *via* the inverse spin Hall effect voltage. From the FMR we can determinate the peak-to-peak linewidth ΔH_{pp} and the resonance field H_{res}.

C.1 Methods

First, from the angular dependence of the resonance field we evaluate parallel and perpendicular external magnetic field configuration with respect to the ferromagnetic electrode. Note that the samples placement is also evaluated using study of the amplitude of FMR spectra and voltage in the way to maximize both values. In FMR experiments we measure the first derivative of the absorption, that can be described using following equation:

$$dX^{"}(H) = -A\frac{\Delta H^2(H-H_r)}{((H-H_r)^2+\Delta H^2)^2}$$

Where A is the amplitude of the FMR spectrum, H_r is the resonance field, ΔH is the linewidth (full width at half maximum). From the FMR study we determinate the effective saturation of the magnetization M_{eff}, g the Landé factor, and the damping constant α of the ferro-magnetic layer.

Using $\sim 9.4\,GHz$ excitation frequencies, the resonant magnetization precession in the ferro-magnetic layer (F), pumps spins to the non-magnetic layer and the corresponding spin current generates an electric field in the non-magnetic material (N) due to ISHE: $E_{ISHE} \propto j_s \times \sigma_{polar}$ where j_s is the spin current density perpendicular to the F/N interface and σ_{polar} is the spin polarization vector. This electric field is converted into a voltage V_{ISHE} between both ends of the NM channel. Consequently there is an enhancement of the peak-to-peak linewidth in F/N bilayers, $\Delta H_{pp}^{F/N}$ with respect to single F layers ΔH_{pp}^{F}. The real part of the mixing conductance $g_r^{\uparrow\downarrow}$, is given by:

$$g_r^{\uparrow\downarrow} = \frac{2\sqrt{3}\pi M_s \gamma t_F}{g\mu_B\omega}(\Delta H_{ppF/N} - \Delta H_{ppF}) = \frac{2\sqrt{3}\pi M_s t_F}{\hbar\omega}(\Delta H_{ppF/N} - \Delta H_{ppF})$$

The spin current density at the interface j_s^0, when H is applied parallel to the film is given by:

$$j_s^0 = \frac{g_r^{\uparrow\downarrow}\gamma\hbar h_{rf}^2}{8\pi\alpha^2}\left[\frac{4\pi M_s\gamma+\sqrt{(4\pi M_s\gamma)^2+2\omega^2}}{(4\pi M_s\gamma)^2+2\omega^2}\right]$$

where h_{rf} is the magnetic field strength of the microwave excitation (of the sample into the resonance cavity). The h_{rf} on the sample is calculated by measuring the Q factor of the resonance cavity ($Q = f/\Delta f$, where Δf is the width at half maximum of the frequency), when the sample is placed into the cavity. In order to measure Δf we use a second cavity in series with the first one.

The voltage V_{ISHE} due to the inverse spin Hall effect is always symmetrical around the resonance field and its amplitude is given by:

$$V_{ISHE} = \frac{w_F\alpha_{SHE}l_{sf}^N}{t_N\sigma_N+t_F\sigma_F}tanh(\frac{t_N}{2l_{sf}^N})(\frac{2e}{\hbar})j_s^0$$

where w_F is the width of the F layer, $t_{F(N)}$ is the thickness of the F (N) layer. The l_{sf}^N and σ_N are the spin diffusion length and the conductivity of the N layer, respectively. Where σ_F is the conductivity of F material.

The voltage V that we measure simultaneously in the SP-FMR experience on a F/N bi-layer might have one symmetric $V_s = V_{ISHE} + V_{s(AMR)}$, and one antisymmetric contribution $V_{assym(AMR)}$, also we will take into account an offset contribution to the signal V_{offset}. We then use the following equation to describe the observed voltage:

$$V(H) = V_{offset} + V_s\frac{\Delta H^2}{(H-H_r)^2+\Delta H^2} + V_{assym(AMR)}\frac{-\Delta H(H-H_r)}{(H-H_r)^2+\Delta H^2} \tag{C.1}$$

Typical geometries and experiments results are represented in figure C.1 for Py and Py/Pt samples. Note that for each bi-layer sample the reference sample is fabricated, which contains only the ferro-magnetic layer. This is done so as to extract the AMR contribution of the ferro-magnetic layer from the measured voltage $V(H)$ and the FMR linewidth ΔH_{ppF}.

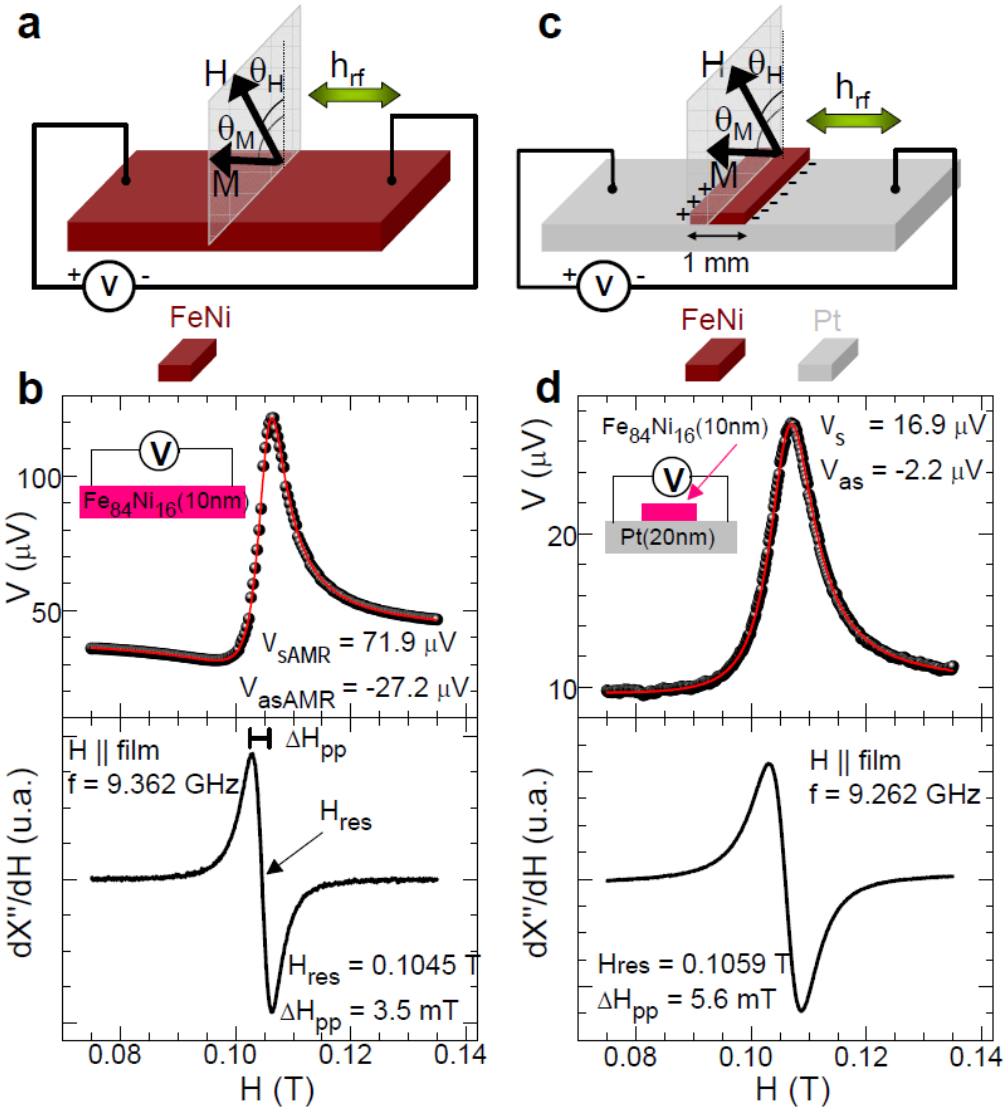

Figure C.1: *Sketch of the sample in the resonance cavity, with the electrical contacts on evaporated (a) FeNi(10nm) and (b) Pt(20nm)/FeNi(10nm) films, along with the polar angles definitions. Their respectively resonance spectrum (bottom) and electromotive force V are shown in (b) and (d). The red lines are fits of the V curves using Eq. C.1*

Bibliography

[1] Fert A.b c Van Dau F.N.b c Chappert, C.a b. The emergence of spin electronics in data storage. *Nature Materials*, 6(11):813–823, 2007. 1

[2] S. A. Wolf, D. D. Awschalom, R. A. Buhrman, J. M. Daughton, S. von Molnar, M. L. Roukes, A. Y. Chtchelkanova, and D. M. Treger. Spintronics: A spin-based electronics vision for the future. *Science*, 294(5546):1488–1495, 2001. 1

[3] S. D. Bader. Opportunities in nanomagnetism. *Rev. Mod. Phys.*, 78:1–15, Jan 2006. 1

[4] Flatte M.E.b Awschalom, D.D.a. Challenges for semiconductor spintronics. *Nature Physics*, 3(3):153–159, 2007. 1

[5] Martin M.-B. Deranlot C. Servet B. Xavier S. Mattana R. Sprinkle M. Berger C. De Heer W.A. Petroff F. Anane A. Seneor P. Fert A Dlubak, B. Highly efficient spin transport in epitaxial graphene on sic. *Nature Physics*, 2012. 1, 66

[6] M. N. Baibich, J. M. Broto, A. Fert, F. Nguyen Van Dau, F. Petroff, P. Etienne, G. Creuzet, A. Friederich, and J. Chazelas. Giant magnetoresistance of (001)fe/(001)cr magnetic superlattices. *Phys. Rev. Lett.*, 61:2472–2475, Nov 1988. 1, 8

[7] G. Binasch, P. Grünberg, F. Saurenbach, and W. Zinn. Enhanced magnetoresistance in layered magnetic structures with antiferromagnetic interlayer exchange. *Phys. Rev. B*, 39:4828–4830, Mar 1989. 1, 8

[8] Albert Fert. Nobel lecture: Origin, development, and future of spintronics. *Rev. Mod. Phys.*, 80:1517–1530, Dec 2008. 1, 3, 8

[9] B. Dieny, V. S. Speriosu, S. S. P. Parkin, B. A. Gurney, D. R. Wilhoit, and D. Mauri. Giant magnetoresistive in soft ferromagnetic multilayers. *Phys. Rev. B*, 43:1297–1300, Jan 1991. 1

[10] M. Julliere. Tunneling between ferromagnetic films. *Physics Letters A*, 54(3):225–226, 1975. 1

[11] T. Miyazaki and N. Tezuka. Giant magnetic tunneling effect in fe/al2o3/fe junction. *Journal of Magnetism and Magnetic Materials*, 139(3):L231–L234, 1995. 1

[12] J. S. Moodera, Lisa R. Kinder, Terrilyn M. Wong, and R. Meservey. Large magnetoresistance at room temperature in ferromagnetic thin film tunnel junctions. *Phys. Rev. Lett.*, 74:3273–3276, Apr 1995. 1

[13] T. Valet and A. Fert. Theory of the perpendicular magnetoresistance in magnetic multilayers. *Phys. Rev. B*, 48(10):7099–7113, Sep 1993. 1, 8, 15, 18, 45, 53, 54, 63, 108

[14] S. Takahashi and S. Maekawa. Spin injection and detection in magnetic nanostructures. *Phys. Rev. B*, 67:052409, Feb 2003. 1, 10, 18, 33, 45, 77

[15] Y. M. Lee, J. Hayakawa, S. Ikeda, F. Matsukura, and H. Ohno. Effect of electrode composition on the tunnel magnetoresistance of pseudo-spin-valve magnetic tunnel junction with a mgo tunnel barrier. *Applied Physics Letters*, 90(21):212507, 2007. 1

[16] S. Ikeda, J. Hayakawa, Y. Ashizawa, Y. M. Lee, K. Miura, H. Hasegawa, M. Tsunoda, F. Matsukura, and H. Ohno. Tunnel magnetoresistance of 604diffusion in cofeb/mgo/cofeb pseudo-spin-valves annealed at high temperature. *Applied Physics Letters*, 93(8):082508, 2008. 1

[17] E. I. Rashba. Theory of electrical spin injection: Tunnel contacts as a solution of the conductivity mismatch problem. *Phys. Rev. B*, 62:R16267–R16270, Dec 2000. 1, 65

[18] J.C. Slonczewski. Current-driven excitation of magnetic multilayers. *Journal of Magnetism and Magnetic Materials*, 159(1-2):L1–L7, 1996. 2

[19] L. Berger. Emission of spin waves by a magnetic multilayer traversed by a current. *Phys. Rev. B*, 54:9353–9358, Oct 1996. 2

[20] Pakala M.-Panchula A. Ding Y. Apalkov D. Wang L.-C. Chen E. Huai Y. Diao, Z. Spin-transfer switching in mgo-based magnetic tunnel junctions (invited). *Journal of Applied Physics*, 99(8), 2006. 2

[21] Stuart S. P. Parkin, Masamitsu Hayashi, and Luc Thomas. Magnetic domain-wall racetrack memory. *Science*, 320(5873):190–194, 2008. 2

[22] Malinowski G.-Klaui M. Boulle, O. Current-induced domain wall motion in nanoscale ferromagnetic elements. *Materials Science and Engineering R: Reports*, 72(9):159–187, 2011. 2

[23] Cros V.-Grollier J. Pereira L.G. Deranlot C. Petroff F.-Faini G. Barnas J. Fert A. Boulle, O. Shaped angular dependence of the spin-transfer torque and microwave generation without magnetic field. *Nature Physics*, 3(7):492–497, 2007. 2

[24] M.I. Dyakonov and V.I. Perel. Current-induced spin orientation of electrons in semiconductors. *Physics Letters A*, 35(6):459 – 460, 1971. 2, 11, 79, 95

[25] Takahashi S.-Harii K. Ieda J.b c Koshibae W.d Ando-K.a Maekawa S.b c Saitoh E.a e Uchida, K. Observation of the spin seebeck effect. *Nature*, 455(7214):778–781, 2008. 2, 81

[26] A. Azevedo, L. H. Vilela-Leao, R. L. Rodriguez-Suarez, A. F. Lacerda Santos, and S. M. Rezende. Spin pumping and anisotropic magnetoresistance voltages in magnetic bilayers: Theory and experiment. *Phys. Rev. B*, 83:144402, Apr 2011. 2, 3, 99

[27] Nagaosa N.-Zhang S.-C. Murakami, S. Dissipationless quantum spin current at room temperature. *Science*, 301(5638):1348–1351, 2003. 2

[28] Jairo Sinova, Dimitrie Culcer, Q. Niu, N. A. Sinitsyn, T. Jungwirth, and A. H. MacDonald. Universal intrinsic spin hall effect. *Phys. Rev. Lett.*, 92:126603, Mar 2004. 2

[29] Pai C.-F. Li-Y. Tseng H.W. Ralph D.C. Buhrman-R.A. Liu, L. Spin-torque switching with the giant spin hall effect of tantalum. *Science*, 336(6081):555–558, 2012. 2, 82

[30] Moriyama T.-Ralph D.C.-Buhrman R.A. Liu, L. Spin-torque ferromagnetic resonance induced by the spin hall effect. *Physical Review Letters*, 106(3), 2011. 2, 82, 99

[31] Park B.-G. Irvine-A.C. Zarbo L.P. Rozkotova E. Nemec-P. Novak V. Sinova J. Jungwirth T. Wunderlich, J. Spin hall effect transistor. *Science*, 330(6012):1801–1804, 2010. 2, 82

[32] T. Kimura, Y. Otani, T. Sato, S. Takahashi, and S. Maekawa. Room-temperature reversible spin hall effect. *Phys Rev Lett*, 98(15):156601, 2007. 2, 3, 77, 82, 99

[33] Laurent Vila, Takashi Kimura, and YoshiChika Otani. Evolution of the spin hall effect in pt nanowires: Size and temperature effects. *Phys. Rev. Lett.*, 99:226604, Nov 2007. 2, 3, 82, 88

[34] A. Fert, A. Friederich, and A. Hamzic. Hall effect in dilute magnetic alloys. *Journal of Magnetism and Magnetic Materials*, 24(3):231 – 257, 1981. 2, 82, 83

[35] Morota M.-Wei D.H.-Deranlot C. Basletic M. Hamzic A.-Fert A. Otani Y. Niimi, Y. Extrinsic spin hall effect induced by iridium impurities in copper. *Physical Review Letters*, 106(12), 2011. 3, 83, 85, 93, 95, 99, 102

[36] Tinkham M. Valenzuela, S.O. Direct electronic measurement of the spin hall effect. *Nature*, 442(7099):176–179, 2006. 3, 26, 72, 74, 77, 88

[37] Hasegawa Y.-Mitani S.-Takahashi S. Imamura H. Maekawa S.-Nitta J. Takanashi K. Seki, T. Giant spin hall effect in perpendicularly spin-polarized fept/au devices. *Nature Materials*, 7(2):125–129, 2008. 3, 29, 82

[38] K. Ando, S. Takahashi, J. Ieda, Y. Kajiwara, H. Nakayama, T. Yoshino, K. Harii, Y. Fujikawa, M. Matsuo, S. Maekawa, and E. Saitoh. Inverse spin-hall effect induced by spin pumping in metallic system. *Journal of Applied Physics*, 109(10):103913, 2011. 3, 86, 99

[39] O. Mosendz, V. Vlaminck, J. E. Pearson, F. Y. Fradin, G. E. W. Bauer, S. D. Bader, and A. Hoffmann. Detection and quantification of inverse spin hall effect from spin pumping in permalloy/normal metal bilayers. *Phys. Rev. B*, 82:214403, Dec 2010. 3, 86, 99

[40] Luqiao Liu, Takahiro Moriyama, D. C. Ralph, and R. A. Buhrman. Spin-torque ferromagnetic resonance induced by the spin hall effect. *Phys. Rev. Lett.*, 106:036601, Jan 2011. 3, 86, 99

[41] H. Nakayama, K. Ando, K. Harii, T. Yoshino, R. Takahashi, Y. Kajiwara, K. Uchida, Y. Fujikawa, and E. Saitoh. Geometry dependence on inverse spin hall effect induced by spin pumping in ni81fe19/pt films. *Phys. Rev. B*, 85:144408, Apr 2012. 3, 86

[42] O. Mosendz, J. E. Pearson, F. Y. Fradin, G. E. W. Bauer, S. D. Bader, and A. Hoffmann. Quantifying spin hall angles from spin pumping: Experiments and theory. *Phys. Rev. Lett.*, 104:046601, Jan 2010. 3, 99

[43] E. Saitoh, M. Ueda, H. Miyajima, and G. Tatara. Conversion of spin current into charge current at room temperature: Inverse spin-hall effect. *Applied Physics Letters*, 88(18):182509, 2006. 3

[44] Z. Feng, J. Hu, L. Sun, B. You, D. Wu, J. Du, W. Zhang, A. Hu, Y. Yang, D. M. Tang, B. S. Zhang, and H. F. Ding. Spin hall angle quantification from spin pumping and microwave photoresistance. *Phys. Rev. B*, 85:214423, Jun 2012. 3, 87

[45] Hoffmann A.-Jiang J.S.-Pearson J.E. Bader S.D. Ji, Y. Non-local spin injection in lateral spin valves. *Journal of Physics D: Applied Physics*, 40(5):1280–1284, 2007. 3, 25, 32, 53

[46] Mark Johnson and R. H. Silsbee. Interfacial charge-spin coupling: Injection and detection of spin magnetization in metals. *Phys. Rev. Lett.*, 55:1790–1793, Oct 1985. 3, 16, 26

[47] Mark Johnson and R. H. Silsbee. Coupling of electronic charge and spin at a ferromagnetic-paramagnetic metal interface. *Phys. Rev. B*, 37:5312–5325, Apr 1988. 3, 16, 26

[48] F.J. Jedema, H.B. Heersche, A.T. Filip, J.J.A. Baselmans, and B.J. van Wees. Electrical detection of spin precession in a metallic mesoscopic spin valve. *Nature*, 416(6882):713–6, 2002. 3, 25, 26, 32, 53, 74

[49] Arne Brataas, Yu. V. Nazarov, and Gerrit E. W. Bauer. Finite-element theory of transport in ferromagnet–normal metal systems. *Phys. Rev. Lett.*, 84:2481–2484, Mar 2000. 3

[50] Frisco Jacobus Jedema. *Electrical Spin Injection in Metallic Mesoscopic Spin Valves*. PhD thesis, Rijksuniversiteit Groningen, 2002. 3, 9, 10, 11, 26, 33, 45, 71

[51] T. Kimura, J. Hamrle, Y. Otani, K. Tsukagoshi, and Y. Aoyagi. Spin-dependent boundary resistance in the lateral spin-valve structure. *Applied Physics Letters*, 85(16):3501–3503, 2004. 3

[52] Hoffmann A.-Pearson J.E.-Bader S.D. Ji, Y. Enhanced spin injection polarization in co/cu/co nonlocal lateral spin valves. *Applied Physics Letters*, 88(5):1–3, 2006. 3

[53] M. V. Costache, M. Zaffalon, and B. J. van Wees. Spin accumulation probed in multiterminal lateral all-metallic devices. *Phys. Rev. B*, 74:012412, Jul 2006. 3, 22, 26, 33

[54] S. Y. Garzon. *Spin injection and detection in copper spin valve structures.* PhD thesis, University of Maryland (College Park, Md.), 2005. 3, 11, 12, 22

[55] Swantje Heers. *Effect of spin-orbit scattering on transport properties of low-dimensional dilute alloys.* PhD thesis, Der Fakultat fur Mathematik, Informatik und Naturwissenschaen der RWTH Aachen University,Hamburg, Deutschland, 2011. 4, 83, 84

[56] Albert Fert and Peter M. Levy. Spin hall effect induced by resonant scattering on impurities in metals. *Phys. Rev. Lett.*, 106:157208, Apr 2011. 4, 85

[57] N. F. Mott. The electrical conductivity of transition metals. *Proceedings of the Royal Society of London. Series A - Mathematical and Physical Sciences*, 153(880):699–717, 1936. 8

[58] K. H. J. Buschow E. P. Wohlfarth. *Ferromagnetic materials: a handbook on the properties of magnetically ordered substances.* North-Holland Pub. Co., 1990. 8

[59] P. C. van Son, H. van Kempen, and P. Wyder. Boundary resistance of the ferromagnetic-nonferromagnetic metal interface. *Phys. Rev. Lett.*, 58:2271–2273, May 1987. 8, 13

[60] Peter A. Grünberg. Nobel lecture: From spin waves to giant magnetoresistance and beyond. *Rev. Mod. Phys.*, 80:1531–1540, Dec 2008. 8

[61] Siegmann Hans Christoph Stohr, Joachim. *Magnetism, From Fundamentals to Nanoscale Dynamics.* Springer Series in Solid-State Sciences, Vol. 152. Springer, 2006. 8, 9

[62] Marius Vasile Costache. *High Frequency Spin Dynamics in Hybrid Metallic Devices.* PhD thesis, Rijksuniversiteit Groningen, 2007. 9, 10, 11, 32

[63] R. J. Elliott. Theory of the effect of spin-orbit coupling on magnetic resonance in some semiconductors. *Phys. Rev.*, 96:266–279, Oct 1954. 11

[64] Y. Yafet. *Solid State Physics*, volume 14. New York: Academic, 1963. 11

[65] Igor Zutic, Jaroslav Fabian, and S. Das Sarma. Spintronics: Fundamentals and applications. *Rev. Mod. Phys.*, 76:323–410, Apr 2004. 11

[66] W. Kolbe. Spin relaxation time of conduction electrons in bulk sodium metal. *Phys. Rev. B*, 3:320–323, Jan 1971. 11

[67] Korenivski V. Poli N. Haviland D.B. Urech, M. Direct demonstration of decoupling of spin and charge currents in nanostructures. *Nano Letters*, 6(4):871–874, 2006. 15

[68] Jack Bass and William P Pratt Jr. Spin-diffusion lengths in metals and alloys, and spin-flipping at metal/metal interfaces: an experimentalist's critical review. *Journal of Physics: Condensed Matter*, 19(18):183201, 2007. 19, 22, 32, 43, 60, 77

[69] Piotr Łączkowski, Laurent Vila, Sara Ferry, Alain Marty, Jean-Marie George, Henri Jaffrès, Albert Fert, Takashi Kimura, Tao Yang, YoshiChika Otani, and Jean-Philippe Attané. Spin signal in metallic lateral spin valves made by a multiple angle evaporation technique. *Applied Physics Express*, 4(6):063007, 2011. 21, 46, 60, 71

[70] Maekawa S. Takahashi, S. Spin current in metals and superconductors. *Journal of the Physical Society of Japan*, 77(3), 2008. 21

[71] S. Takahashi and S. Maekawa. Spin injection and transport in magnetic nanostructures. *Physica C: Superconductivity*, 437(0):309, 2006. 22, 45, 88

[72] F. J. Jedema, M. S. Nijboer, A. T. Filip, and B. J. van Wees. Spin injection and spin accumulation in all-metal mesoscopic spin valves. *Phys. Rev. B*, 67(8):085319, Feb 2003. 22

[73] Otani Y. Kimura, T. Spin transport in lateral ferromagnetic/nonmagnetic hybrid structures. *Journal of Physics Condensed Matter*, 19(16), 2007. 22

[74] J. Hamrle, T. Kimura, Y. Otani, K. Tsukagoshi, and Y. Aoyagi. Current distribution inside py/cu lateral spin-valve devices. *Phys. Rev. B*, 71:094402, Mar 2005. 23, 25, 32, 47, 63

[75] Chang J. Eom J. Koo H. Han S.-H. Kim-G. Ku, J.H. Inhomogeneous spin accumulation in py/au/py spin valve. *Physica Status Solidi (B) Basic Research*, 244(12):4530–4533, 2007. 25

[76] T. Kimura, T. Sato, and Y. Otani. Temperature evolution of spin relaxation in a nife/cu lateral spin valve. *Phys. Rev. Lett.*, 100:066602, Feb 2008. 25, 83

[77] Kimura T. Otani Y. Yang, T. Giant spin-accumulation signal and pure spin-current-induced reversible magnetization switching. *Nature Physics*, 4(11):851–854, 2008. 25, 26, 30, 31, 73

[78] S. Yakata, Y. Ando, and T. Kimura. Optimization of interface condition for efficient spin injection in permalloy/cu lateral spin valve. In *TENCON 2010 - 2010 IEEE Region 10 Conference*, pages 126 –128, nov. 2010. 26

[79] J.A. Caballero, C.E. Moreau, Jr. Pratt, W.P., and N.O. Birge. Magnetoresistance of a planar spin valve with single-domain ferromagnetic probes. *Magnetics, IEEE Transactions on*, 37(4):2111, jul 2001. 26

[80] Schreiber D.K. Liu Y. Pearson J.E. Bader S.D.-Petford-Long-A.K. Hoffmann A. Mihajlovic, G. Enhanced spin signals due to native oxide formation in ni80 fe20/ag lateral spin valves. *Applied Physics Letters*, 97(11), 2010. 26, 27

[81] Alexandru Vlad, Sorin Melinte, Maria Matefi-Tempfli, Luc Piraux, and Stefan Matefi-Tempfli. Statistical nanopatterning: Vertical nanowire architectures: Statistical processing

of porous templates towards discrete nanochannel integration (small 18/2010). *Small*, 6(18):n/a–n/a, 2010. 26

[82] H. Jaffres, J.-M. George, and A. Fert. Spin transport in multiterminal devices: Large spin signals in devices with confined geometry. *Phys. Rev. B*, 82(14):140408, Oct 2010. 31, 54, 55, 59, 63, 64, 66

[83] T. Kimura, J. Hamrle, and Y. Otani. Estimation of spin-diffusion length from the magnitude of spin-current absorption: Multiterminal ferromagnetic/nonferromagnetic hybrid structures. *Phys. Rev. B*, 72:014461, Jul 2005. 32, 89, 90

[84] G. Bridoux, M. V. Costache, J. Van de Vondel, I. Neumann, and S. O. Valenzuela. Enhanced spin signal in nonlocal devices based on a ferromagnetic cofeal alloy. *Applied Physics Letters*, 99(10):102107, 2011. 33

[85] M.J. Donahue and D.G. Porter. Oommf user's guide, version 1.0. Technical Report NISTIR 6376, National Institute of Standards and Technology, Gaithersburg, Sept 1999. 34

[86] K. Shigeto, T. Shinjo, and T. Ono. Injection of a magnetic domain wall into a submicron magnetic wire. *Applied Physics Letters*, 75(18):2815 –2817, nov 1999. 34

[87] Potter R.I. McGuire, T.R. Anisotropic magnetoresistance in ferromagnetic 3d alloys. *IEEE Transactions on Magnetics*, MAG-11(4):1018–1038, 1975. 34

[88] V. D. Nguyen, L. Vila, P. Laczkowski, A. Marty, T. Faivre, and J. P. Attané. Detection of domain-wall position and magnetization reversal in nanostructures using the magnon contribution to the resistivity. *Phys. Rev. Lett.*, 107:136605, Sep 2011. 35, 37, 77

[89] V. D. Nguyen, C. Naylor, L. Vila, A. Marty, P. Laczkowski, C. Beigne, L. Notin, Z. Ishaque, and J. P. Attane. Magnon magnetoresistance of nife nanowires: Size dependence and domain wall detection. *Applied Physics Letters*, 99(26):262504, 2011. 37

[90] Guido van Rossum. Python library reference. CWI Report CS-R9524, 1995. 37

[91] John D. Hunter. Matplotlib: A 2d graphics environment. *Computing In Science & Engineering*, 9(3):90–95, May-Jun 2007. 37

[92] L. J. van der Pauw. A method of measuring specific resistivity and Hall effect of discs of arbitrary shape. *Philips Res.Rep*, 13(1), 1958. 40

[93] J Bass and W.P Pratt Jr. Current-perpendicular (cpp) magnetoresistance in magnetic metallic multilayers. *Journal of Magnetism and Magnetic Materials*, 200:274, 1999. 43, 55

[94] http://www.python.org/. 49

[95] Eric Jones, Travis Oliphant, Pearu Peterson, et al. SciPy: Open source scientific tools for Python, 2001–. 49

[96] T. Haillard R. Acharyya R. Loloee-W. P. Pratt Jr. J. Bass J. Zhang M. A. Crimp A. Sharma, N. Theodoropoulou. Current-perpendicular-to-plane magnetoresistance of ferromagnetic f/al interfaces (f=py, co, fe, and co91fe9) and structural studies of co/al and py/al. *Phys. Rev. B*, 77:224438, 2008. 50, 56

[97] N. Theodoropoulou, A. Sharma, R. Loloee, W. P. Pratt, J. Bass, A. Fert, and H. Jaffres. Interface specific-resistance and scattering asymmetry of permalloy/al. *Journal of Applied Physics*, 99(8):08G502 –08G502–3, apr 2006. 50, 56

[98] N. Theodoropoulou, A. Sharma, T. Haillard, R. Loloee, W.P. Pratt, J. Bass, J. Zhang, and M.A. Crimp. Specific resistance, scattering asymmetry, and some thermal instability, of co/al, fe/al, and co 91fe9 /al interfaces. *Magnetics, IEEE Transactions on*, 43(6):2860, june 2007. 50, 56

[99] J. Fabian and S. Das Sarma. Spin relaxation of conduction electrons in polyvalent metals: Theory and a realistic calculation. *Phys. Rev. Lett.*, 81:5624–5627, Dec 1998. 51

[100] J. Fabian and S. Das Sarma. Spin relaxation of conduction electrons. volume 17, pages 1708–1715. AVS, 1999. 51

[101] Daniel Lubzens and Sheldon Schultz. Observation of an anomalous frequency dependence of the conduction-electron spin resonance in al. *Phys. Rev. Lett.*, 36:1104–1106, May 1976. 51

[102] R. H. Silsbee and Fran çois Beuneu. Model calculation of the frequency and temperature dependence of the electron-spin-resonance linewidth of aluminum. *Phys. Rev. B*, 27:2682–2692, Mar 1983. 51

[103] T. Kimura, T. Sato, and Y. Otani. Temperature evolution of spin relaxation in a nife/cu lateral spin valve. *Phys Rev Lett*, 100(6):066602, 2008. 51

[104] Chang J. Kim H. Eom J. Ku, J.-H. Effective spin injection in au film from permalloy. *Applied Physics Letters*, 88(17), 2006. 53, 60, 62

[105] Otani Y. Hamrle J. Kimura, T. Switching magnetization of a nanoscale ferromagnetic particle using nonlocal spin injection. *Physical Review Letters*, 96(3), 2006. 53

[106] F. Beuneu and P. Monod. The elliott relation in pure metals. *Phys. Rev. B*, 18:2422, Sep 1978. 54

[107] Anton A. Starikov, Paul J. Kelly, Arne Brataas, Yaroslav Tserkovnyak, and Gerrit E. W. Bauer. Unified first-principles study of gilbert damping, spin-flip diffusion, and resistivity in transition metal alloys. *Phys. Rev. Lett.*, 105(23):236601, Dec 2010. 56

[108] Y. Fukuma, L. Wang, H. Idzuchi, and Y. Otani. Enhanced spin accumulation obtained by inserting low-resistance mgo interface in metallic lateral spin valves. *Applied Physics Letters*, 97(1):012507, 2010. 59, 71

[109] Taro Wakamura, Kohei Ohnishi, Yasuhiro Niimi, and YoshiChika Otani. Large spin accumulation with long spin diffusion length in cu/mgo/permalloy lateral spin valves. *Applied Physics Express*, 4(6):063002, 2011. 59

[110] Wang L. Idzuchi H. Takahashi S. Maekawa S.-Otani Y. Fukuma, Y. Giant enhancement of spin accumulation and long-distance spin precession in metallic lateral spin valves. *Nature Materials*, 10(7):527–531, 2011. 59, 71, 72, 73, 74, 77

[111] P. Laczkowski, L. Vila, V.-D. Nguyen, A. Marty, J.-P. Attané, H. Jaffrès, J.-M. George, and A. Fert. Enhancement of the spin signal in permalloy/gold multiterminal nanodevices by lateral confinement. *Phys. Rev. B*, 85:220404, Jun 2012. 59, 63

[112] Janghae Ku, Joonyeon Chang, Suk-Hee Han, Jae Geun Ha, and Jonghwa Eom. Spin injection in nife/au/nife spin valves. *Journal of Magnetism and Magnetic Materials*, 304(1):e273 – e275, 2006. 60

[113] Maekawa S. Takahashi, S. Spin current, spin accumulation and spin hall effect. *Science and Technology of Advanced Materials*, 9(1), 2008. 63

[114] A. Fert and H. Jaffres. Conditions for efficient spin injection from a ferromagnetic metal into a semiconductor. *Phys. Rev. B*, 64:184420, Oct 2001. 65, 66

[115] G. Schmidt, D. Ferrand, L. W. Molenkamp, A. T. Filip, and B. J. van Wees. Fundamental obstacle for electrical spin injection from a ferromagnetic metal into a diffusive semiconductor. *Phys. Rev. B*, 62:R4790–R4793, Aug 2000. 65

[116] D. L. Smith and R. N. Silver. Electrical spin injection into semiconductors. *Phys. Rev. B*, 64:045323, Jul 2001. 65

[117] Pratt Jr. W.P. Bass, J. Spin-diffusion lengths in metals and alloys, and spin-flipping at metal/metal interfaces: An experimentalist's critical review. *Journal of Physics Condensed Matter*, 19(18), 2007. 66

[118] Valeria Ferrari Gavin Burnell-Jose P. Valdes-Herrera Benjamin D. Simons Peter B. Littlewood Emilio Artacho Albert Fert Luis E. Hueso, Jose M. Pruneda and Neil D. Mathur. Transformation of spin information into large electrical signals using carbon nanotubes. *Nature*, 445:410–413, 2007. 66

[119] F. J. Jedema, M. V. Costache, H. B. Heersche, J. J. A. Baselmans, and B. J. van Wees. Electrical detection of spin accumulation and spin precession at room temperature in metallic spin valves. *Applied Physics Letters*, 81(27):5162–5164, 2002. 73, 74

[120] Adelmann C. Crooker S.A. Garlid E.S. Zhang J.-Reddy K.S.M. Flexner-S.D. PalmstrÃžm C.J. Crowell P.A. Lou, X. Electrical detection of spin transport in lateral ferromagnet-semiconductor devices. *Nature Physics*, 3(3):197–202, 2007. 74

[121] Hyun Cheol Koo, Jae Hyun Kwon, Jonghwa Eom, Joonyeon Chang, Suk Hee Han, and Mark Johnson. Control of spin precession in a spin-injected field effect transistor. *Science*, 325(5947):1515–1518, 2009. 74

[122] Awo-Affouda C. Hanbicki A.T. Li C.H. Thompson P.E. Jonker-B.T. van't Erve, O.M.J. Information processing with pure spin currents in silicon: Spin injection, extraction, manipulation, and detection. *IEEE Transactions on Electron Devices*, 56(10):2343–2347, 2009. 74

[123] T. Sasaki, T. Oikawa, T. Suzuki, M. Shiraishi, Y. Suzuki, and K. Noguchi. Temperature dependence of spin diffusion length in silicon by hanle-type spin precession. *Applied Physics Letters*, 96(12):122101, 2010. 74

[124] A. Aharoni. Demagnetizing factors for rectangular ferromagnetic prisms. *Journal of Applied Physics*, 83(6):3432–3434, 1998. 75

[125] T. Miyasato, N. Abe, T. Fujii, A. Asamitsu, S. Onoda, Y. Onose, N. Nagaosa, and Y. Tokura. Crossover behavior of the anomalous hall effect and anomalous nernst effect in itinerant ferromagnets. *Phys. Rev. Lett.*, 99:086602, Aug 2007. 81

[126] Naoto Nagaosa, Jairo Sinova, Shigeki Onoda, A. H. MacDonald, and N. P. Ong. Anomalous hall effect. *Rev. Mod. Phys.*, 82:1539–1592, May 2010. 81

[127] E. I. Rashba H.A. Engel and B. I. Halperin. *Handbook of Magnetism and Advanced Magnetic Materials*, volume 5. John Wiley and Sons, 2007. 81

[128] Junichiro Inoue and Hideo Ohno. Taking the hall effect for a spin. *Science*, 309(5743):2004–2005, 2005. 82

[129] Yu. V. Pershin, N. A. Sinitsyn, A. Kogan, A. Saxena, and D. L. Smith. Spin polarization control by electric stirring: Proposal for a spintronic device. *Applied Physics Letters*, 95(2):022114, 2009. 82

[130] Guang-Yu Guo, Sadamichi Maekawa, and Naoto Nagaosa. Enhanced spin hall effect by resonant skew scattering in the orbital-dependent kondo effect. *Phys. Rev. Lett.*, 102:036401, Jan 2009. 82

[131] Sugai I. Ziman T. Guo G.Y. Nagaosa N. Seki T. Takanashi-K. Maekawa S. Gu, B. Surface-assisted spin hall effect in au films with pt impurities. *Physical Review Letters*, 105(21), 2010. cited By (since 1996) 2. 82

[132] Ziman T. Guo G.-Y. Nagaosa N. Maekawa S. Gu, B. Giant spin hall effect of au films with pt impurities: Surface-assisted skew scattering. *Journal of Applied Physics*, 109(7), 2011. 82

[133] Stephan Lowitzer, Martin Gradhand, Diemo Ködderitzsch, Dmitry V. Fedorov, Ingrid Mertig, and Hubert Ebert. Extrinsic and intrinsic contributions to the spin hall effect of alloys. *Phys. Rev. Lett.*, 106:056601, Feb 2011. 83

[134] Christian R. Ast, Jürgen Henk, Arthur Ernst, Luca Moreschini, Mihaela C. Falub, Daniela Pacilé, Patrick Bruno, Klaus Kern, and Marco Grioni. Giant spin splitting through surface alloying. *Phys. Rev. Lett.*, 98:186807, May 2007. 85

[135] T. Hirahara, T. Komorida, A. Sato, G. Bihlmayer, E. V. Chulkov, K. He, I. Matsuda, and S. Hasegawa. Manipulating quantum-well states by surface alloying: Pb on ultrathin ag films. *Phys. Rev. B*, 78:035408, Jul 2008. 85

[136] L. Liu, R.A. Buhrman, and D.C. Ralph. Review and analysis of measurements of the spin hall effect in platinum. *ArXiv e-prints*, November 2011. 92, 98, 100

[137] Shufeng Zhang. Spin hall effect in the presence of spin diffusion. *Phys. Rev. Lett.*, 85:393–396, Jul 2000. 94

[138] E. M. Hankiewicz, Jian Li, Tomas Jungwirth, Qian Niu, Shun-Qing Shen, and Jairo Sinova. Charge hall effect driven by spin-dependent chemical potential gradients and onsager relations in mesoscopic systems. *Phys. Rev. B*, 72:155305, Oct 2005. 94

[139] R. V. Shchelushkin and Arne Brataas. Spin hall effects in diffusive normal metals. *Phys. Rev. B*, 71:045123, Jan 2005. 94

[140] İ. Adagideli, G. E. W. Bauer, and B. I. Halperin. Detection of current-induced spins by ferromagnetic contacts. *Phys. Rev. Lett.*, 97:256601, Dec 2006. 94

[141] J. E. Hirsch. Spin hall effect. *Phys. Rev. Lett.*, 83:1834–1837, Aug 1999. 95

[142] Shufeng Zhang. Spin hall effect in the presence of spin diffusion. *Phys. Rev. Lett.*, 85:393–396, Jul 2000. 95

[143] M. Morota, Y. Niimi, K. Ohnishi, D. H. Wei, T. Tanaka, H. Kontani, T. Kimura, and Y. Otani. Indication of intrinsic spin hall effect in 4*d* and 5*d* transition metals. *Phys. Rev. B*, 83:174405, May 2011. 95, 100

[144] K. Ando, S. Takahashi, K. Harii, K. Sasage, J. Ieda, S. Maekawa, and E. Saitoh. Electric manipulation of spin relaxation using the spin hall effect. *Phys. Rev. Lett.*, 101:036601, Jul 2008. 99

[145] H. Kurt, R. Loloee, K. Eid, Jr. W. P. Pratt, and J. Bass. Spin-memory loss at 4.2 k in sputtered pd and pt and at pd/cu and pt/cu interfaces. *Applied Physics Letters*, 81(25):4787–4789, 2002. 99

[146] Christophe Geuzaine and Jean-Franccois Remacl. Gmsh: a three-dimensional finite element mesh generator with built-in pre- and post-processing facilities. 107

[147] P. Dular and C. Geuzaine. GetDP reference manual: the documentation for GetDP, a general environment for the treatment of discrete problems. http://www.geuz.org/getdp/. 107

[148] P. Dular, C. Geuzaine, A. Genon, and W. Legros. An evolutive software environment for teaching finite element methods in electromagnetism. *IEEE Transactions on Magnetics*, 35(3):1682–1685, May 1999. 107

[149] Klayout. http://www.klayout.de/. 113